COMPUTATIONAL ANALYSIS AND OPTIMISATION OF THE INLET SYSTEM OF A HIGH-PERFORMANCE RALLY ENGINE

BY

KATLEGO WEBSTER MAKGATA

Submitted in partial fulfilment of the requirements for the degree of

Master of Engineering (Mechanical Engineering)

In the

Faculty of Engineering, Built Environment and Information Technology

University of Pretoria

May 2005

SUMMARY

Computational analysis and optimisation of the inlet system of a high-performance rally engine

Katlego Webster Makgata

Study leaders: Prof. K.J. Craig; Mr. D. J. de Kock

Department: Department of Aeronautical and Mechanical Engineering, University of Pretoria

Degree: Master of Engineering

In the car-racing world, whether it is motor cross, formula 1 or rally racing, there is a need for maximum power through the race. While this is not possible through the entire engine speed range, it is possible to manipulate the engine speed at which maximum power is obtained by changing the engine configuration. Where restrictions prevent engine reconfiguration to move the maximum power engine speed, there is the option of increasing the engine power at the set engine speed. One of the most effective ways to do this is to modify the intake system to allow for more air into the engine, thus allowing for more fuel to be burnt and more power to be obtained. While fuel economy suffers, this is sacrificed in the pursuit for maximum power. This dissertation focused on improving the inlet system of a high-performance rally car race engine by using computational fluid dynamics (CFD) and mathematical optimisation techniques, the combination of which is called a computational flow optimisation (CFO) system.

The history and background of intake systems is presented in the literature survey section followed by a discussion on variable intake manifolds. Variable intake manifolds are extensively used in modern production sports cars because of their advantage of improving smooth power delivery through the entire engine speed range. The theory of waves and their interactions is also given along with the theory of engine tuning with regards to intake systems. Tuning takes advantage of the energy of flow pulses to increase the amount of charge that is inducted into the engine. The

numerical methods used to solve for flow in intake systems are also presented as they form the basis of the engine simulation code used in the study, namely EngMod4T.

The governing equations as well as other important aspects, such as grid generation, boundary conditions and convergence, which relate to CFD are discussed. The literature survey is concluded by a discussion on the mathematical optimisation algorithm employed in this study.

The literature survey is followed by the presentation of the CFD work done in determining the amount of air inducted by the intakes. The simulations are transient in nature in order to capture the pulse interactions and their influence on the mass of air inducted by the intakes. The first case considered is that of a single intake exposed to atmosphere. To relate the results of the single intake simulation to a full-intake simulation, the mass of inducted air is assumed to be equal for all four intakes. This assumption was found to be flawed as shown by the simulation that followed that took into consideration all four intakes also open to atmosphere. The simulation showed that the intakes actually induct differing amounts of air and the total amount is less than for four single trumpets. A more comprehensive simulation was conducted where the airbox was included and the resulting total mass inducted showed that even less air is inducted by this setup. The results of the latter were used as the basis of the optimisation study that followed. Various airbox designs, obtained from the optimisation software LS-OPT, were simulated and resulted in an improved airbox design that inducts 6.2% more air than the original airbox. And since there is direct relationship between mass of air inducted and engine power produced, it is expected that the engine power would also increase by 6.2%.

The study demonstrates the successful implementation of a CFO system to solve a complex industrial flow problem. With the increase of computing power and increasing affordability of such systems coupled with the ease-of-use of commercial CFD software, CFO should become more common in industrial application.

Keywords: airbox, computational fluid dynamics, computational flow optimisation, inlet system, simulation, transient, mathematical optimisation.

ACKNOWLEDGEMENTS

My sincere thanks go to the following that contributed in their own way:

Professor Ken Craig and Danie de Kock. My family and friends who showed me support throughout my study period. Thanks to Toyota Motorsport for donating their facilities, time and for partially sponsoring this study. I would like to extend my sincere thanks to the CSIR for also sponsoring the study and for their *unbelievable* patience. And a special thank you to my mother for all her prayers.

In memory of my father, Philemon Bolayang Makgata, and my aunt, Dr. Princess Tlou Mmolawa.

TABLE OF CONTENTS

Abbreviations and Acronyms

This list contains abbreviations and acronyms as used in this report.

Abbreviation or Acronym	**Definition**
ABDC	After bottom dead centre
ANOVA	Analysis of variance
ATDC	After top dead centre
BBDC	Before bottom dead centre
BTDC	Before top dead centre
CAD	Computer-aided design
CFD	Computational fluid dynamics
CFO	Computational flow optimisation
DNS	Direct numerical simulation
DOHC	Double overhead cam
FV	Finite volume
ICE	Internal combustion engine
LES	Large eddy simulation
LFOPC	Leap Frog Optimisation for Constrained Optimisation
PDE	Partial differential equation
PISO	Pressure-implicit with splitting of operators
RANS	Reynolds-averaged Navier-Stokes
RPM	Revolutions per minute
RSM	Reynolds stress methods
SIMPLE	Semi-implicit Method of Pressure-Linked Equations
SRSM	Successive response surface method
VVT	Variable valve timing
WOT	Wide open throttle

List of Figures

List of Tables

CHAPTER 1 : Introduction

1.1 MOTIVATION

The recent increase in computing power coupled with the declining cost of computers has led to a rapid development in the science of computational fluid dynamics (CFD) simulation. Simulation can be defined as the prediction and reconstruction of behaviour of a product or physical situation under assumed or known conditions. It is widely used in various engineering disciplines as a means of quickly determining or improving the behaviour of a design, thus saving on experimental work that can be expensive.

However, the emergence of simulation has not made experimental tests obsolete, as these are important for verification during the design process. CFD as a simulation tool has proved itself to be extremely useful over the years, especially since some phenomena cannot be determined experimentally, for example molten steel flow patterns. It has also been successfully used in the aerospace industry to predict aerodynamic behaviour of aircraft components such as wings, canards, etc. These simulations also yield derived flow information such as vorticity and residence time, which are difficult to measure. CFD has also been extended for use in industrial applications such as continuous steel casting, heat sink design (for cooling), building ventilation and automotive engine cooling.

The use of CFD in prediction and improvement of system behaviour has, over the years, gained acceptance in industrial application. This approach has worked well in the improvement of a Formula 1 [1] and race car intake system, [2], [3], where the results were also validated by road tests. Achieving race car intake performance improvement without going the trial-and-error route is essential for economy and time reasons, which is the reason that CFD and mathematical optimisation were employed in this endeavour. Also, previous experimental attempts to improve the intake system that is the subject of this study have yielded little success, hence the decision to use numerical techniques.

The sole objective of this study is to determine and improve the flow in the engine intake system of the concerned rally race engine through the use of the combination of CFD and mathematical optimisation techniques. Understandably, the accuracy of numerical methods is of great concern especially in CFD with the wide choice of modelling options, all which give converged but different solutions. In this study, this issue is addressed by comparing the results to flowbench experimental results.

1.2 OVERVIEW

A literature survey on the subject of intake flow, its history and existing intakes, is presented in CHAPTER 2. Also included in this chapter is the theory of tuning, wave interaction and numerical methods, concepts that are essential in order to understand intake flow. The governing equations of flow are given in the section that discusses CFD, together with a discussion of turbulence modelling as implemented in the software used. Grid generation and the grid types employed in the study are also presented. Mathematical optimisation and its formulation are also discussed in this chapter. Only the optimisation technique that is relevant to the study is discussed in detail.

An application of the CFD methods discussed above is given in CHAPTER 3 where the intake is progressively modelled from the simplest geometry to the most complex. The results are given and discussed in this section. Also included is the comparison between numerical and experimental results as part of the validation effort.

CHAPTER 4 extends on the findings of CHAPTER 3. In this chapter, the optimisation technique presented in the literature survey is applied to the problem, and the optimisation loop, in conjunction with CFD, is performed to come to an improved airbox design.

A summary of the work conducted in this study is given in CHAPTER 5. Conclusions and recommendations for future work are also included based on the results obtained in the study. Recommendations are based largely on the computational limitations and numerical difficulties experienced in the study.

CHAPTER 2 : Literature Study

2.1 ENGINE INTAKE SYSTEMS

2-1.1 Introduction

The basic function of engine intake systems is to provide the engine with a fresh air-fuel mixture every cycle for combustion to take place. Different engine operation requirements demand individualised intake systems. In other words, a vehicle that is used for everyday purposes cannot have the same intake system as a racing vehicle, though they may share the same engine platform. Racing engines require maximum volumetric efficiency for increased power and torque, but this is not desirable as far as economy is concerned. Everyday-use vehicles seldom require top-end power, thus economy and driveability at lower speeds are more important in this instance. It is therefore important that intake systems are designed to suit the purpose for which the engine is intended.

This chapter begins by giving a basic overview of the intake system and its history, followed by the system requirements for improved flow. The flow behaviour in the intake is discussed next and thereafter, the exhaust gas effects are discussed. The last section will describe engine intake performance prediction as applied to numerical methods.

2-1.2 Overview and history of engine intakes

Engine intakes serve as flow passageways for the combustion of the air-fuel mixture in the engine. Much attention has been focused in this area of development in an attempt to maximise airflow into the engine, which would translate into better performance. There is direct correlation between mass flow and power as shown by Heywood [4]. The design of such systems has until recently been on a trial-and-error basis, which is costly and time consuming. Early intake systems were based on any commercially available pipes without regard for scientific reasoning pertaining to interior flow. Many theories, largely by experience, were put forward regarding the

behaviour of the flow in the intake. These theories proved useful through the years even when verification was necessary. Smith and Morrison [5] conducted extensive research in this area and their work is still regarded as the basis for many scientific designs. They proved most theories were actually justified and shed light onto other factors to be considered when designing intake-exhaust systems. An example of an early intake ram-induction attempt can be seen in Figure 2-1 as used on a 1937 Riley 1100cc and a 1500cc four-cylinder engine.

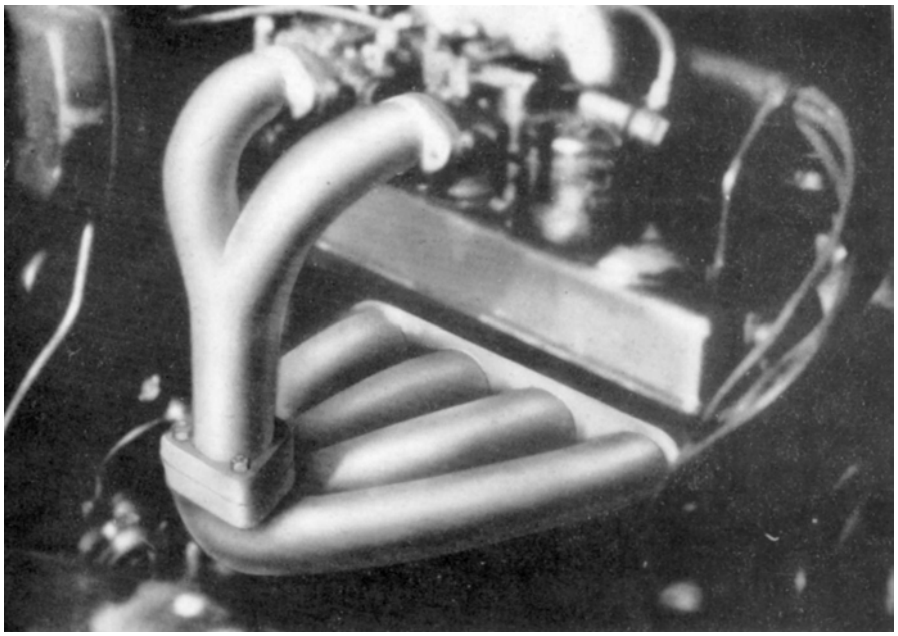

Figure 2-1: 1937 Riley hi-charge induction system [5]

The long induction ducts were used to try and take advantage of the ram effect. Although the system was not a success due to erratic mixture formation arising from wide temperature effects, more attempts on different engines did yield some success. Chrysler Corporation had notable success with increased inlet length ducting as seen in Figure 2-2. The long ducts make efficient use of the pressure pulsations to achieve a torque increase of around ten percent (10%). The ducts, equal in length, were selected to give an increase in torque over a 1500 rpm range with the maximum occurring at 2800 rpm.

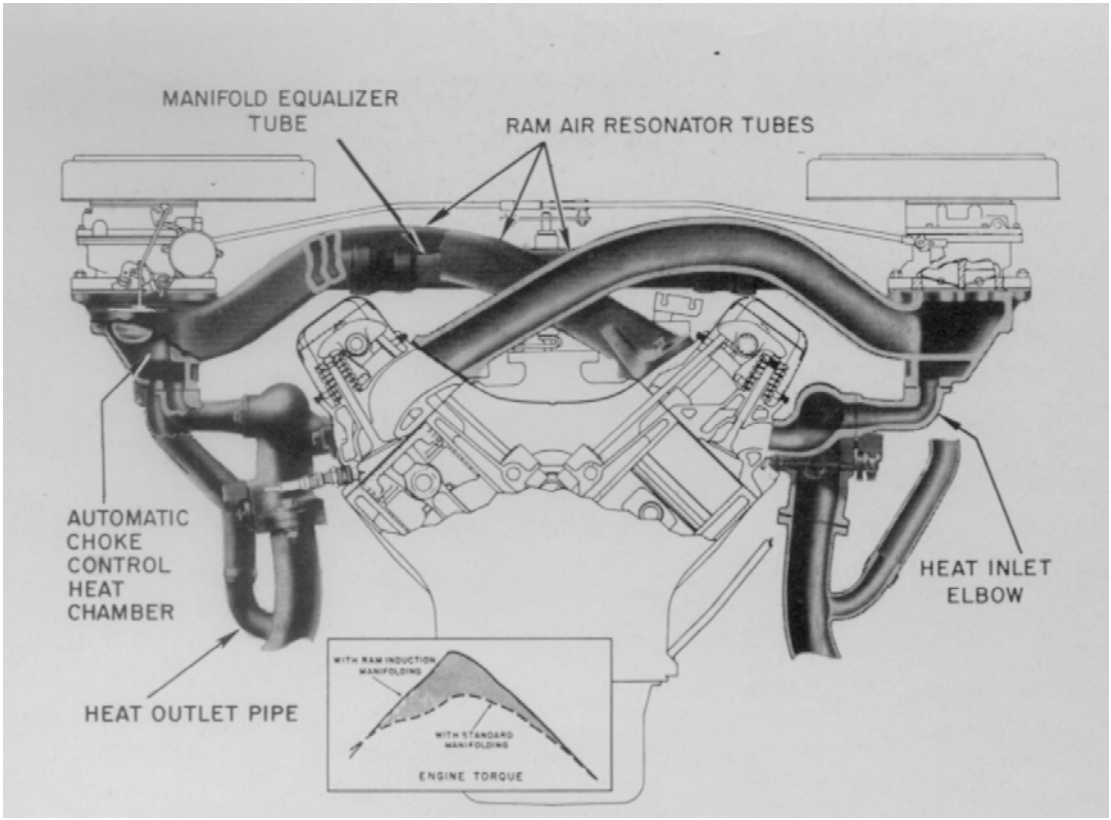

Figure 2-2: Induction tract of a Chrysler Valiant 5.2 litre V-8 [5]

The layout of induction systems has not changed much since the early days. Basically the system comprises an air inlet, load control device, carburettor/injector and inlet tract (duct or manifold) leading into an inlet port. In some arrangements, like in a carburettor engine, the inlet port serves the same purpose as the manifold. On the other hand, the arrangement mentioned is normally different for racing engines where the air inlet is usually replaced by a combination of a bellmouth-end type pipe and an airbox-filter combination. The bellmouth-end pipe is normally referred to as a "trumpet". This arrangement is shown in Figure 2-3.

The airbox acts as a plenum chamber where the incoming air is diffused, thereby increasing the pressure and reducing the velocity. Thus increased amounts of air can be inducted with the use of the airbox. On Boxer (flat cylinder arrangement) and V-type (V-arranged cylinders) engines, resonance intake manifolds may be used to boost mid to high revving efficiency. A common plenum chamber feeds each bank of cylinders through separate pipes [6].

Two pipes of different diameters connect the plenum chambers on the cylinder banks and a valve controlled by an engine management system can close one of the pipes to vary the amount of air going into each bank. The firing order is arranged such that the cylinders breathe alternately from each chamber hence creating pressure waves between them. If the frequency of pressure wave matches the engine speed, cylinder filling is greatly improved and so is volumetric efficiency. By closing one of the interconnecting pipes at low engine revs, the area and the frequency are reduced thus enhancing mid-rev output.

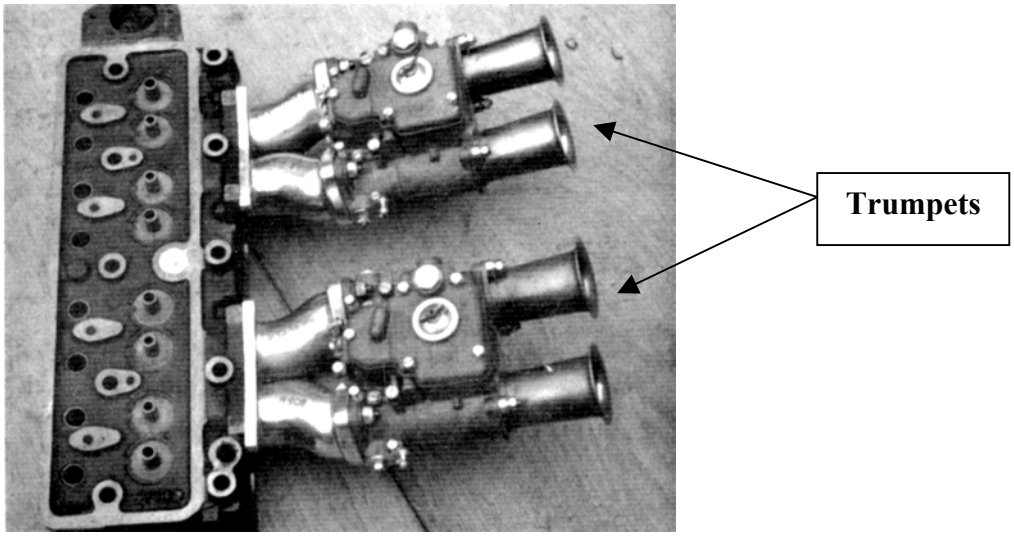

Figure 2-3: Two twin-barrel carburettors with adaptor manifolds and trumpets on a Morgan-TR four-cylinder engine [5]

Modern-day intake systems use innovative ways to achieve an even spread of torque throughout the engine speed range. One ingenious design is the variable inlet tract length manifold. This design varies the inlet tract length according to the engine speed, thus running the engine at its optimum at all speeds. This system is widely used by large car manufacturers such as Audi, BMW, Nissan, Volkswagen, Ferrari and Porsche [8]. Motor manufacturer Mazda, has also used innovative induction systems on their engines further showing the importance attached to intake systems and their effect on power and torque [9], [10].

2-1.3 Variable intake manifolds

There are two kinds of variable intake manifolds namely; variable length intake and resonance intake manifolds. Both manifolds make use of the geometry of intake manifolds to reach the same goal. These manifolds are normally used on heavy modern sedans that would benefit from increased torque. In addition, sports cars such as the Ferrari 360 M and the 550 M make use of this technology for better driveability at low speeds. By combining these manifolds with a system such as variable valve timing (VVT), the engine can be made more flexible throughout its speed range with improved fuel consumption.

The figures in Table 2-1 illustrate the 3-stage intake Porsche VarioRam system as used on the 993 Carrera.

Table 2-1: Illustration of Porsche's VarioRam System [8]

<table>
<tr>
<td> 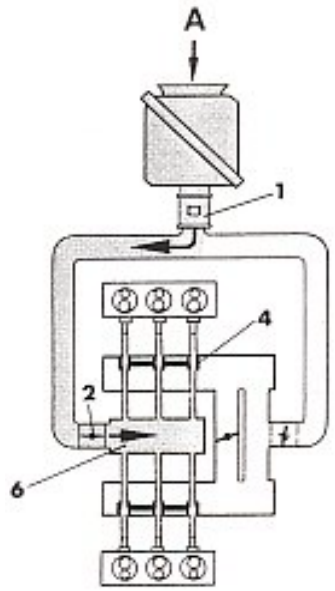

Figure 2-4: Below 5000rpm</td>
<td> 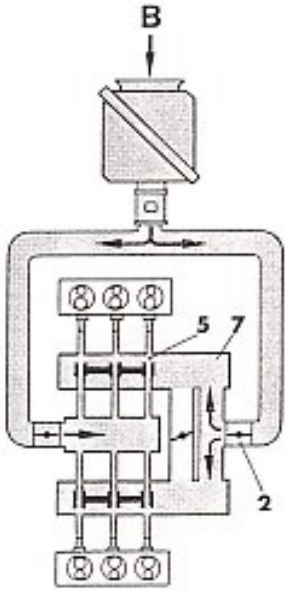

Figure 2-5: 5000-5800 rpm</td>
<td> 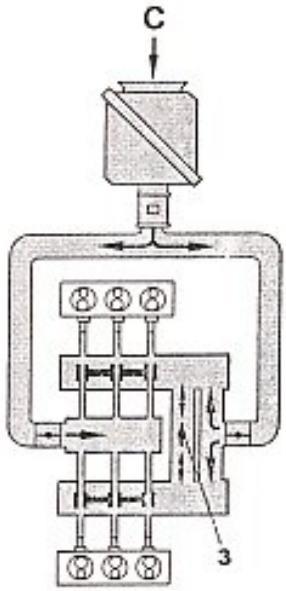

Figure 2-6: Above 5800 rpm</td>
</tr>
<tr>
<td> 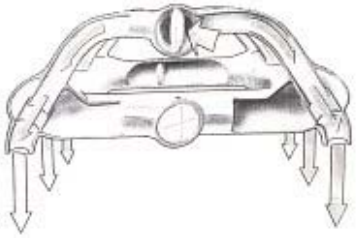
Figure 2-7: Below 5000rpm</td>
<td> 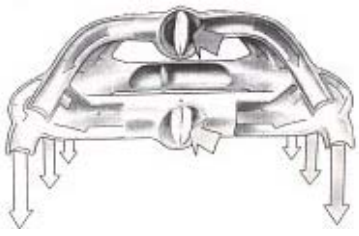
Figure 2-8: 5000-5800 rpm</td>
<td> 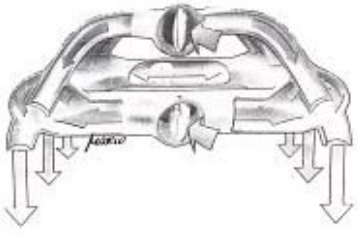
Figure 2-9: Above 5800 rpm</td>
</tr>
</table>

Below 5000 rpm, the long pipes and the resonance intake (item number 7) are disabled and in the mid-range speed (5000-5800 rpm), the long pipes plus short-pipe resonance intake are opened (valve 2) with one of the interconnected pipes of the resonance intake pipes closed. At the top-end speed range, all the pipes are opened to achieve maximum charging from the resonance intake.

Even with modern-day intake-exhaust system scientific design principles, many arrangements are still a compromise between cost and engine efficiency. Unavoidable engine design requisites are mostly responsible for a loss of efficiency, especially in the intake stages. Valve-timing requirements, such as overlapping between inlet and exhaust valve openings, are to blame for some loss of intake charge. The effect of blow down is mostly evident in forced-induction engines where the momentum of the incoming charge carries it through the open exhaust valve during overlapping.

As the cost of development is of concern to many designers, most intake system designs are not optimised for reduced flow resistance and/or increased mass flow rate. Modifications to intake systems can yield increased mass flow with only a slight increase in power and torque. However, the cost and time required to arrive at the optimised intake system can be enormous. It is because of this fact that many designers cannot justify spending much time, effort and funds to optimise such systems for mass production vehicles.

However, any slight increase in power and torque in the motor racing world could mean the difference between winning and losing races. It is for this reason that research and development has been most active in this segment of motoring. Intake system designers harness exhaust gas energy to enhance mass flow into the cylinder head by making use of the pressure wave motion of the exhaust process. However, this effect can only be obtained if the exhaust pipe is tuned for that particular speed to avoid exhaust gas motion from having a negative effect on performance. It is thus imperative that one has a good understanding of the unsteady gas process before commencing with the tuning of intake-exhaust systems. Smith and Morrison [5], Blair [6] and Smith *et al* [7] provide an in-depth analysis and explanation of the mechanisms that govern these gas processes.

Found in Blair [6], are also some useful sections dealing with tuning as well as engine computer (numerical) modelling. Because of modern-day computing capability, large engine simulations can be performed and it is thus helpful to have some guidance in this area to ensure credible and cost-effective results in the shortest time possible.

2-1.4 System Requirements

Intake manifolds usually comprise a load-control device (throttle body), a plenum and runners that feed the charge to individual cylinders. Requirements in the design of such systems include low resistance to the flow, good distribution of air-fuel charge to the individual cylinders, tract lengths that can take advantage of the ram and tuning effects as well as manifold heating for adequate fuel vaporisation.

One popular method to increase flow in the inlet port is through a gas-flowing process, where the surface roughness of the inlet port is reduced substantially hence reducing resistance to the flow. However, the effect this has on power output of an engine is minimal when compared to other methods such as manifold tuning.

Manifold tuning takes advantage of the pressure pulses in the manifold to increase mass flow. By making the manifold a certain length, it is possible for the highest negative pressure wave to occur at the manifold exit (cylinder inlet) at chosen engine speeds. When the valve is opened at this point, this pressure energy forces the air mixture into the cylinder. Extensive research has gone into engine manifold and airbox tuning as indicated by the amount of available literature in this regard.

The airflow quality in an airbox can be improved by reducing sharp corners as well as ensuring that choking does not occur anywhere in the throat (i.e., negative entry effects are minimised). Choking occurs when the local mach number reaches unity, thus limiting the amount of intake charge inducted. De Vita *et al* [2],[3], have done some research in this field and have successfully reduced the losses in the airbox by using CFD as an aid. Although optimisation was performed, it was based on trial-and-error thus not necessarily ensuring an optimum design. This study however, gives an understanding of sources of flow losses and thus provides a starting point for the mathematical optimisation process. By eliminating obvious design parameters that

give rise to losses, an optimum design can be reached in fewer iterations. This not only saves time and effort, but also reduces expenses.

2-1.5 Numerical methods

Numerical methods for determining the pressure in the system have been developed and used extensively over the years. These methods provide solutions to the complex governing equations of fluid behaviour such as mass and heat transfer. Rapid advances in computing power have made it possible for these equations to be solved in an economic manner for complex flow problems where the equations may be non-linear and the computational expense enormous. Numerous authors such as Winterbone and Yoshitomi [11], Winterbone and Pearson [12], and Blair [6] have done extensive research on this subject, with much success in accurately predicting the transient pressure in intake systems. Their contributions are covered in this section. Basically, the authors describe the intake flow in terms of wave theory.

Wave behaviour theory is largely based on sound theory and its propagation through a medium after Newton, Laplace and other scientists discovered the correlation between sound and wave actions. These wave action methods are applied to determine the behaviour of waves within the engine intake system to predict the performance for different configurations.

Intake charge within an intake pipe propagates in waveform because of the unsteady pressure at the inlet valve due to piston movement as well as combustion in the cylinder. Multiple waves are set up in the process and these waves move back and forth in the intake, setting up pressure pulses. However, these waves do not normally move in the same direction resulting in particle collisions. This phenomenon is known as *super-positioning*. It is fundamental to understand this phenomenon as it occurs continuously in the intake pipes and can be the cause of some inaccurate pressure transducer readings in experimental work.

Basically two types of waves are continuously set up in engine manifolds namely, linear and non-linear waves. These types of waves are discussed in detail.

2.1.5.1 Linear waves

Linear waves are waves that propagate in a pipe system with disturbances whose amplitude is small when compared to the undisturbed flow. This assumption leads to the classical wave equation

$$\frac{\partial^2(\Delta p)}{\partial t^2} = a_0^2 \frac{\partial^2(\Delta p)}{\partial x^2} \tag{2.1}$$

This equation describes propagation through a homogenous medium at a single wave speed, a_0. This wave speed, independent of either waveform or direction of propagation, can refer to the speed of light in electromagnetic waves in free space or the speed of sound in acoustic waves. Analytical solutions to equation (2.1) can be obtained in both the time and frequency domain as will be shown.

Time domain solution

To obtain the solution in the time domain Equation (2.1) is re-written as follows

$$\frac{\partial^2 p_e}{\partial t^2} = a_0^2 \frac{\partial^2 p_e}{\partial x^2}, \tag{2.2}$$

where p_e is the excess pressure above the undisturbed level, i.e., $p_e = p - p_0$, with proposed general solutions of the form

$$p_e = f(t - x/a_0) + g(t + x/a_0) \tag{2.3}$$

or

$$p_e = f(x - a_0 t) + g(x + a_0 t), \tag{2.4}$$

where the functions f and g represent longitudinal pressure waves, travelling in opposite directions, in which the wave induces a velocity field parallel to the direction of propagation. The sum of the individual waves gives the resultant pressure wave. By considering movement only in the positive x-direction ($g = 0$), equation (2.4) reduces to

$$p_e = f(x - a_0 t) \tag{2.5}$$

which remains constant for no wave amplitude dissipation hence the quantity $(x - a_0 t)$ must be constant thus

$$x = a_0 t + \text{const}. \tag{2.6}$$

At time t = 0 and still considering the positive x-direction, equation (2.4) gives an arbitrary wave of the form *f(x)*. At a later time *t*, the wave has an identical shape but shifted by distance $a_0 t$ as shown by Figure 2-10 and hence, waves can be tracked from one end of a pipe to the other by simply taking note of the time delay. This method is sometimes referred to as transmission line analysis because of the direct analogy to transmission of power in an electrical transmission line without any losses.

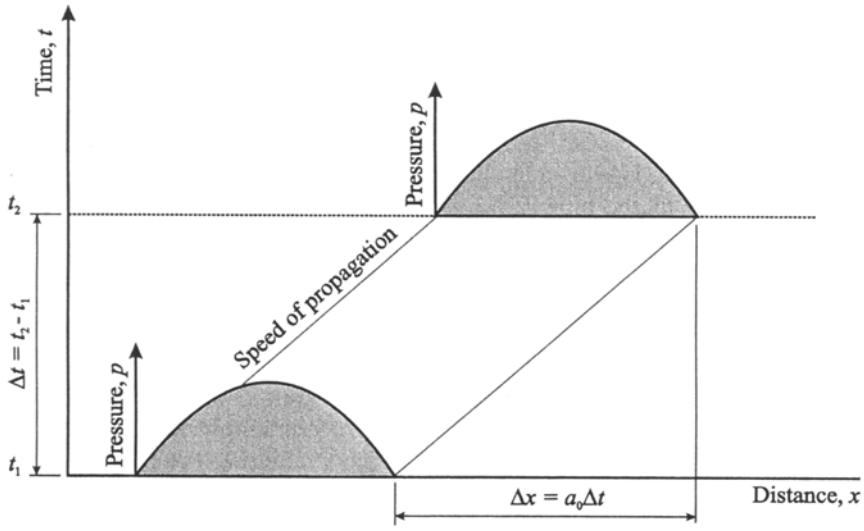

Figure 2-10: Propagation of a linear wave [12]

The relationship between the excess pressure, p_e, and the fluid velocity, *u*, in the direction of propagation of linear waves is given by

$$p_e \mp \rho_0 a_0 u = 0 \tag{2.7}$$

The net velocity of induced by waves moving in the positive and negative *x*-directions respectively, is of the following form

$$u = \frac{1}{\rho_0 a_0}\left[f\left(x - a_0 t\right) - g\left(x + a_0 t\right)\right] \tag{2.8}$$

The mass flow rate is given by

$$\dot{m} = \rho_0 u F \tag{2.9}$$

where F is the pipe cross-sectional area. By substituting equation (2.8) into (2.9) the mass flow rate is redefined as

$$\dot{m} = \frac{1}{Z_c}\left[f\left(x - a_0 t\right) - g\left(x + a_0 t\right)\right] \tag{2.10}$$

where $Z_c = a_0/F$ is known as the pipe impedance, the inverse of which (Y_c) is called the pipe admittance.

Pearson, Winterbone and others have applied linear wave theory in the time domain to solve pipe network systems and also wave propagation in engine intake manifolds because of the fast solution times of such models. The assumptions of linear wave theory are more appropriate for engine intake manifold flow because of the smaller pressure wave amplitudes and velocities. Also, the flow in intake manifolds has entropy levels that are nearly constant when compared to exhaust gas flow. These methods are also very good in predicting volumetric efficiencies.

Frequency domain solution

Further understanding of the characteristics of wave propagation can be obtained by describing the linear wave equations in the frequency domain. Expressions can then be derived for the natural frequency of complex manifold systems. Since the system considered in this study is one of a simple nature not requiring wave equation solutions in the frequency domain, the reader is referred to Winterbone and Pearson [12] for the full mathematical treatment and derivations.

2.1.5.2 Non-linear waves

The system considered in this study includes an airbox, whose flow behaviour cannot be easily determined by the use of linear wave theory, hence requiring the use of non-linear wave theory. A summary of non-linear wave theory is presented below.

Contrary to linear waves, as non-linear waves propagate, their amplitude is affected and shocks can occur as shown by Figure 2-11.

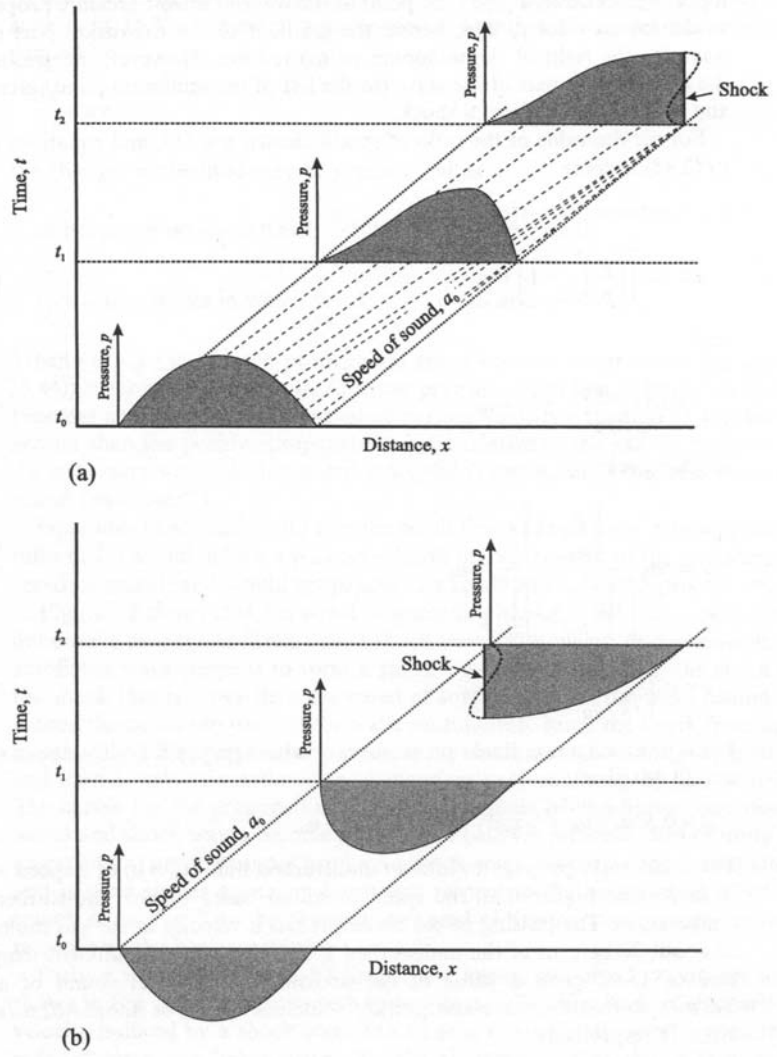

Figure 2-11: Propagation of non-linear (a) pressure and (b) rarefaction waves along a pipe [12]

The equations that describe the waves will be presented in their summarised form for both simple and compound waves. The full derivation of the equations is dealt with in detail by Winterbone and Pearson [12]. Simple waves are waves that propagate as a result of a single disturbance, while compound waves are a result of wave super-positioning.

Simple waves

The particle or gas velocity as a function of pressure is of the form

$$u = \frac{2a_0}{\kappa - 1}\left[\left(\frac{p}{p_0}\right)^{(\kappa-1)/2\kappa} - 1\right] + u_0 \qquad (2.11)$$

while the speed of propagation, c, of a point on the wave is the sum of the local gas velocity and the local speed of sound to give the following

$$c = \frac{2a_0}{\kappa - 1}\left[\frac{\kappa + 1}{2}\left(\frac{p}{p_0}\right)^{(\kappa-1)/2\kappa} - 1\right] + u_0, \tag{2.12}$$

where κ is the ratio of specific heats of the medium through which the wave is travelling. The above equations are known as the Earnshaw's equations. From equation (2.12), the propagation speed of points in a wave increases as the pressure increases, and eventually the pressure wave steepens and a shock is formed as seen in Figure 2-11. After the shock has formed, it is maintained and equations (2.11) and (2.12) are no longer valid. The shock wave characteristics are described by the following equations

$$u = a_0 \frac{\left[\frac{p}{p_0} - 1\right]}{\left[\frac{\kappa(\kappa-1)}{2}\left\{\left(\frac{\kappa+1}{\kappa-1}\right)\frac{p}{p_0} + 1\right\}\right]^{1/2}} + u_0 \tag{2.13}$$

and

$$c = a_0\left[\left(\frac{\kappa-1}{2\kappa}\right)\left\{\left(\frac{\kappa+1}{\kappa-1}\right)\frac{p}{p_0} + 1\right\}\right]^{1/2} + u_0 \tag{2.14}$$

For air, with a ratio of specific heats, $\kappa = 7/5$, equations (2.11) to (2.14) become for no shock:

$$u = 5a_0\left[\left(\frac{p}{p_0}\right)^{1/7} - 1\right] + u_0 \tag{2.15}$$

and

$$c = a_0\left[6\left(\frac{p}{p_0}\right)^{1/7} - 5\right] + u_0. \tag{2.16}$$

while for shock waves:

$$u = 5a_0 \frac{\left[\frac{p}{p_0} - 1\right]}{\left[7\left\{6\frac{p}{p_0} + 1\right\}\right]^{1/2}} + u_0 \tag{2.17}$$

and

$$c = a_0 \left[\left(\frac{1}{7}\right)\left\{6\frac{p}{p_0} + 1\right\}\right]^{1/2} + u_0 \,. \tag{2.18}$$

Compound waves

Expressions for the resultant pressure and velocity of compound wave systems can also be derived. Consider two non-linear waves travelling towards one another in stationary air (At pressure p_0 and speed of sound a_0) with absolute crest pressures of p_1 and p_2. As they overlap, the absolute pressure and particle velocity of the resultant wave at the overlap region become p_t and u_t respectively. The resultant particle velocity in that region is given by

$$u_t = 5a_0\left[\left(\frac{p_1}{p_0}\right)^{1/7} - 1\right] - 5a_0\left[\left(\frac{p_2}{p_0}\right)^{1/7} - 1\right] \tag{2.19}$$

which is essentially the summation of the two wave particle velocities thus

$$u_t = u_1 + u_2 \,. \tag{2.20}$$

Equation (2.20) is also valid for linear waves with the negative sign in equation (2.19) just an indication of the direction in which the wave is travelling, the convention being left to right is positive while right to left is negative.

Method of Characteristics

Non-linear waves can be analysed through the use of the *Method of Characteristics* since the partial differential equations do not yield closed analytical solutions. This method aided in the simulation of engine performance while highlighting major features of unsteady flow in engine manifolds. Besides having difficulty in dealing with different fluids, two other major drawbacks of the method are [12]:

1. Conservation of properties, i.e., continuity, energy and momentum, is not always achievable between two pipe ends, especially where there are large pipe cross-section changes or entropy variations.
2. The method has difficulty in handling large pressure waves, which can be a problem especially when dealing with exhaust systems that have diffusers.

To overcome these defects, finite difference (volume) methods, as found in most computational fluid dynamics codes (CFD), are used while also making it possible to find solutions in more than one dimension. The solution algorithms for these methods can be written in conservative form and they can handle large pressure waves and shocks with little numerical difficulties.

2-1.6 Tuning

Engine tuning can be loosely defined as a process of getting a system to respond in a desired manner at specified engine speeds while taking into account the interactions between the intake and exhaust systems. The many factors involved in engine tuning have led to tuning developing into a science with methods for calculating wave actions explored in more detail for increased accuracy. There are two distinct types of inlet tuning namely, inertia and resonance tuning [11].

First-Order Helmholtz resonator

Inertia charging occurs due to the individual runners and throttle bodies per cylinder and their geometry, while resonance tuning is largely influenced by plenums.

Cylinder charging at the tuning speed is dependent on the system resonance frequency, which in turn depends on whether the inlet valve is closed or open. This resonance is the vibration of air column in the intake manifold and different vibration behaviours have been identified. When the valve is closed, the pipes resonate as a quarter wave organ pipe with the frequency given by [11]:

$$f = \frac{a}{4L} \tag{2.21}$$

where a = speed of sound of air in the manifold [m/s]

L = length of the primary pipe [m]

f = frequency [Hz]

However, when the valve is open, the system resonates as a *Helmholtz resonator*. This mode of vibration occurs when the column of air in the pipe moves in-phase against the air in the cylinder. An analogy can be made to the spring-mass system in which the spring is the compressibility of the air in the cylinder and the mass is the mass of the column of air. The natural frequency of a first-order Helmholtz resonator is given by equation (2.22):

$$f = \frac{a}{2\pi}\left[\frac{S}{LV}\right]^{\frac{1}{2}} \tag{2.22}$$

where S = cross-sectional area of primary pipe [m^2] and

V = volume of resonator chamber [m^3].

Alternatively, the volume V in the equation above can be taken as the mean cylinder volume during the induction stroke, thus equation (2.22) becomes:

$$f = \frac{a}{2\pi}\left[\frac{2S}{LV}\right]^{\frac{1}{2}}\left[\frac{r-1}{r+1}\right]^{\frac{1}{2}} \tag{2.23}$$

where r = nominal compression ratio.

Figure 2-12 is an illustration of the first-order Helmholtz resonator (I-C resonator). Here the gas dynamics are modelled as a spring-mass system with the air in the cylinder modelled as an air spring (Spring) and the air in the manifold as an air piston (Mass).

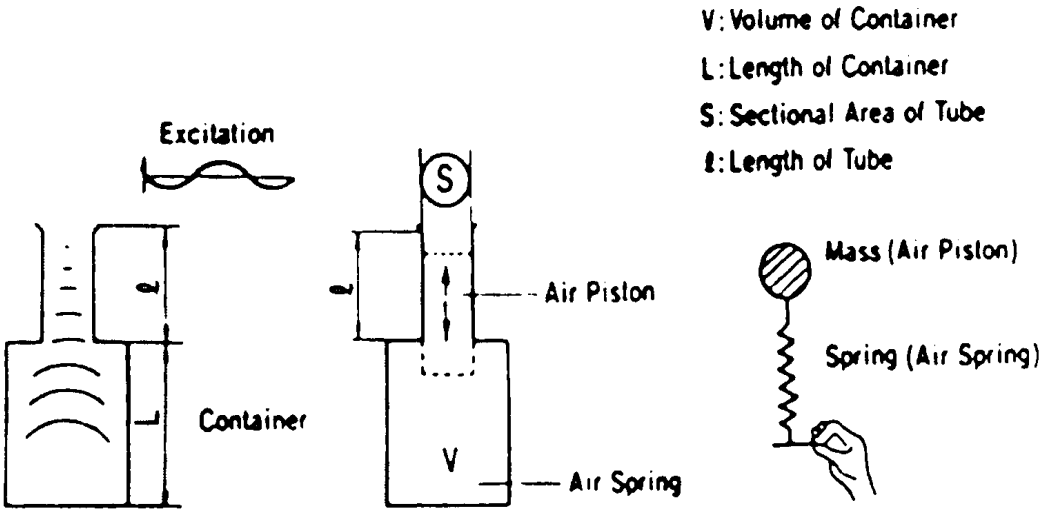

Figure 2-12: The 1st Order Helmholtz Resonator (I-C Resonator) [11]

Such a resonance system results in tuning at certain engine speeds with the peak pressure occurring at the inlet valve before it closes. Although not explicitly stated, it can be assumed that most of the publications that appear on frequency tuning are based on equations (2.21) and (2.23).

Through immense experimental work on a four-cylinder engine, Winterbone and Pearson [12] have shown that the primary pipe length has a major influence on the volumetric efficiency of an engine as shown in Figure 2-13. The standard manifold pipe length of the engine was 0.4 m, which was increased and decreased at intervals of 0.05 m.

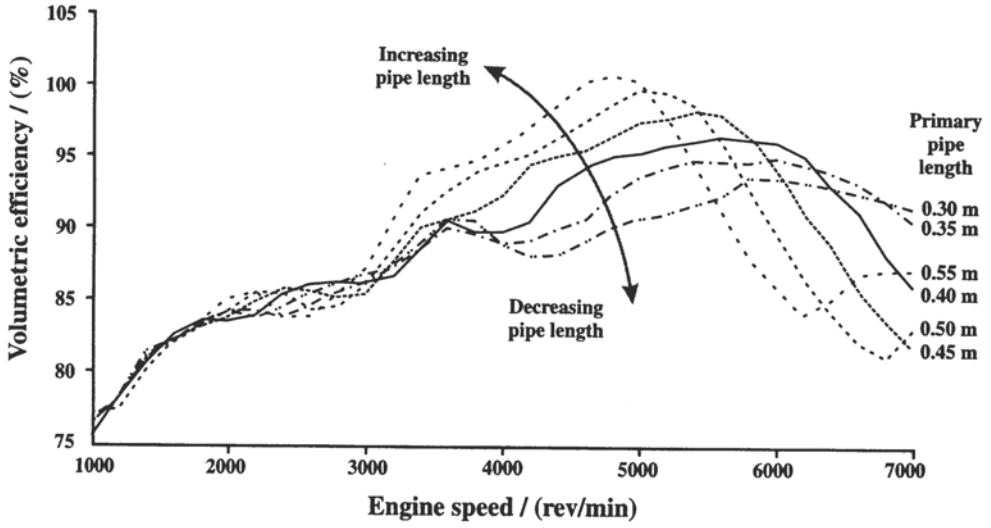

Figure 2-13: Effect of primary pipe length on volumetric efficiency for a four-cylinder engine [12]

The volumetric efficiency plots exhibit two peaks at different engine speeds and it can be seen that the engine speed at which the first peak occurs, for all plots, changes very little when compared to the second peak. As the pipe is lengthened, the second peak increases due to the increased amount of air in the manifold. At the same time, the resonant frequency is reduced (see equation (2.21)) making the engine lose power at higher speeds. On the other hand, shortening the manifold pipe results in the second peak moving to the higher engine speed range with reduced volumetric efficiency. Inertia tuning, brought about by manifold resonance effects, accounts for the shifting of the second peak through the engine range. It is evident from the figure that by combining the two tuning modes; one can achieve a steady increase of volumetric efficiency and torque over a wide engine speed range, hence the emergence of variable intake manifolds in modern vehicles.

Second-Order Helmholtz Resonator

The Second-Order Helmholtz resonator (R-P resonator), applicable only to boxer and V-type engines, comprises a resonance tube and a plenum. Referring to Figure 2-14, the air in the plenum is modelled as a spring (Spring A) and the air in the resonance tubes as an air piston (Mass A).

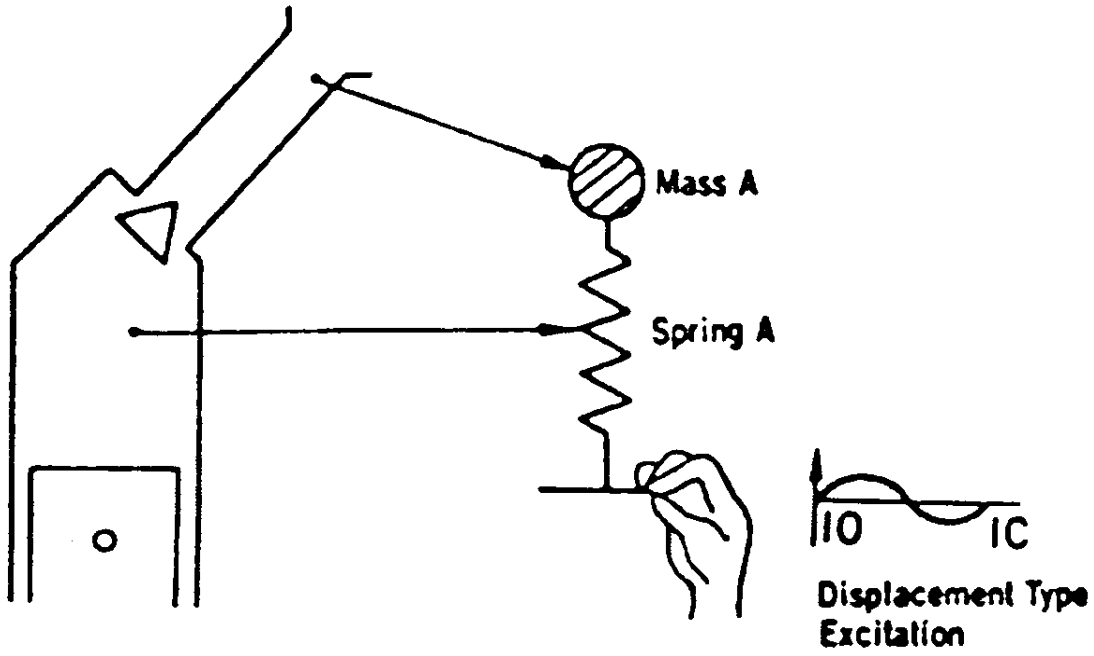

Figure 2-14: The 2nd Order Helmholtz Resonator (R-P Resonator) [11]

In the boxer and V-type configurations, charging is achieved by a combination of inertia and resonance charging when using a resonance-charging manifold. Thus combining both the I-C and R-P resonators, modelling of these engine types is possible. The configuration in both types of engines is symmetrical in nature and thus the system can be simplified by only considering one bank of cylinders and plenums. The modelling process from the engine configuration to the final simplified symmetrical two-degree-of-freedom model can be seen in Figure 2-15.

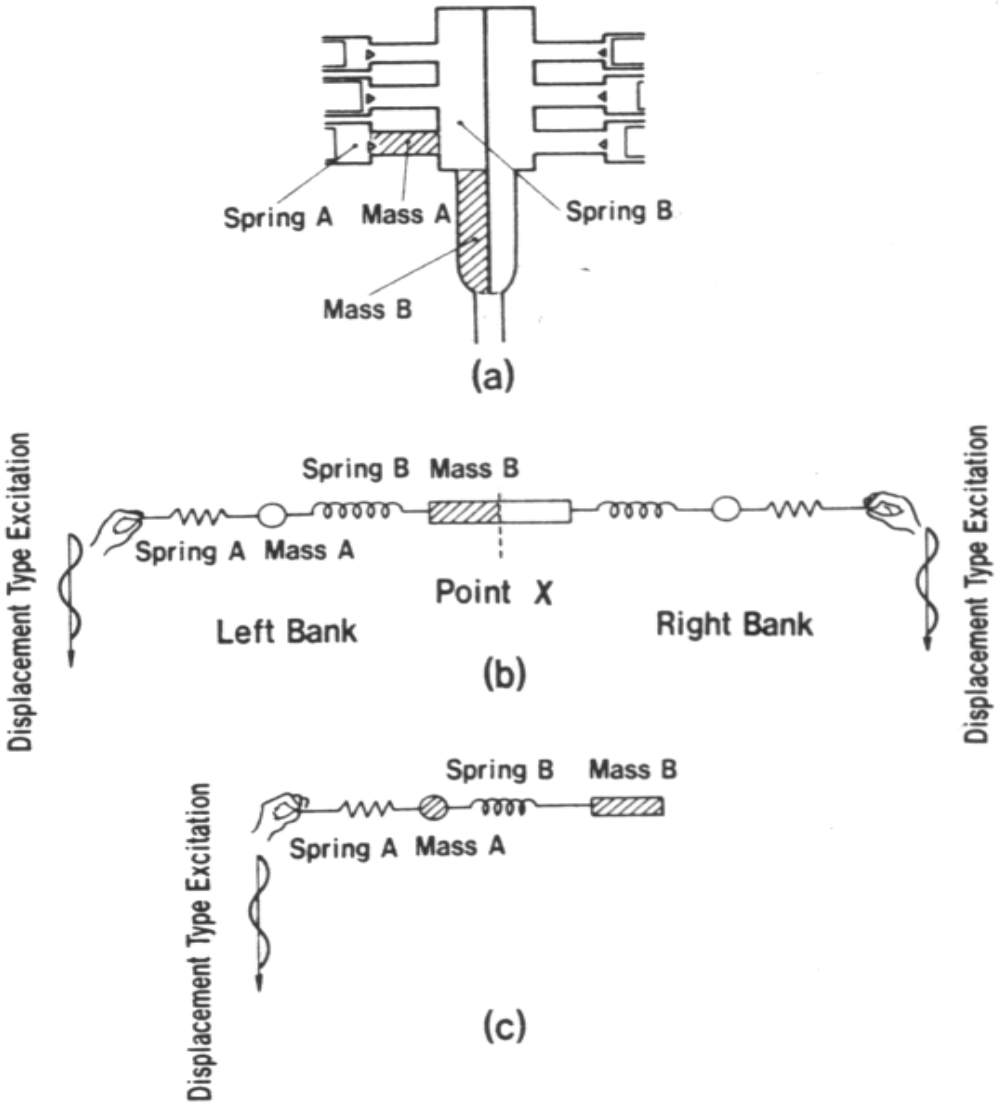

Figure 2-15: Modelling of a resonance charging manifold two-degree-of-freedom system [9]

2-1.7 Excitation

The piston movement during the induction stroke as well as the inlet valve changing area, provide the necessary excitation required for inertia and resonance charging. In first-order systems, there is an increase in phase shift between the excitation and the spring, with an increase in excitation frequency. At the resonance speed, this results in a quarter period phase shift when the pressure is observed in the manifold (see Figure 2-16).

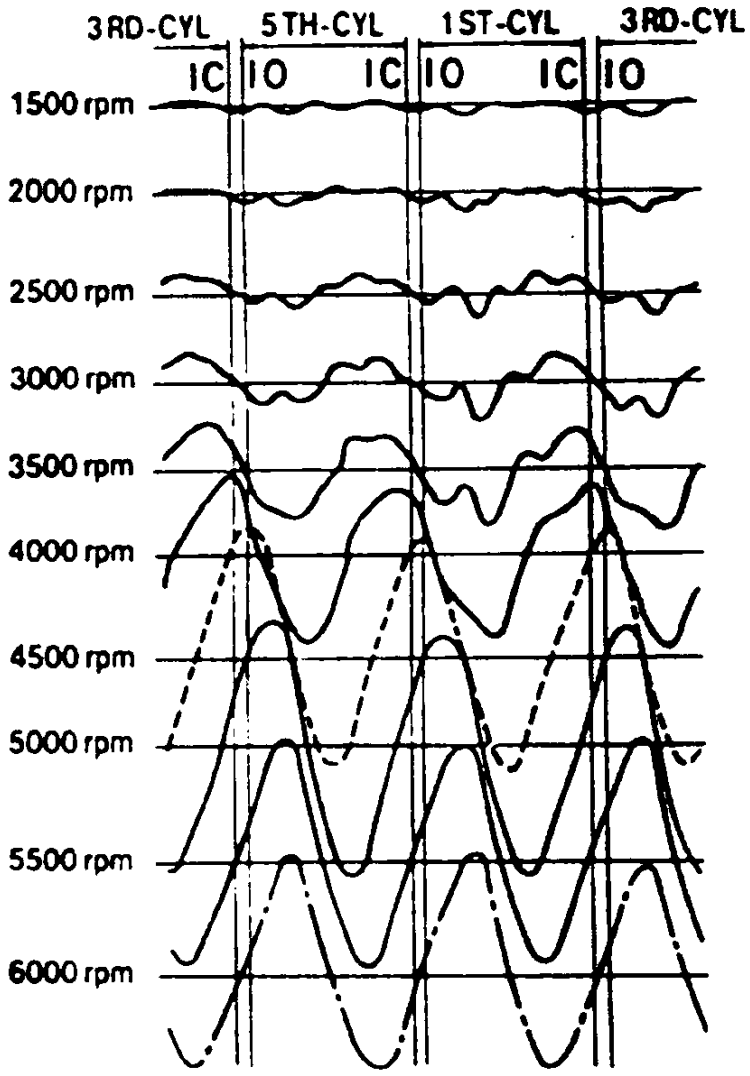

Figure 2-16: Pressure at inlet valve vs. crank angle at different speeds. [Dotted line depicts resonance speed (4500 rpm)] [9]

In a resonance charging manifold, two resonance engine speeds exist as shown in Figure 2-17. At low engine revolutions per minute (rpm) and primary resonant rpm, both mass A and B are in phase and with the result that when both springs are compressed, a higher mass flow rate is expected at the inlet valve.

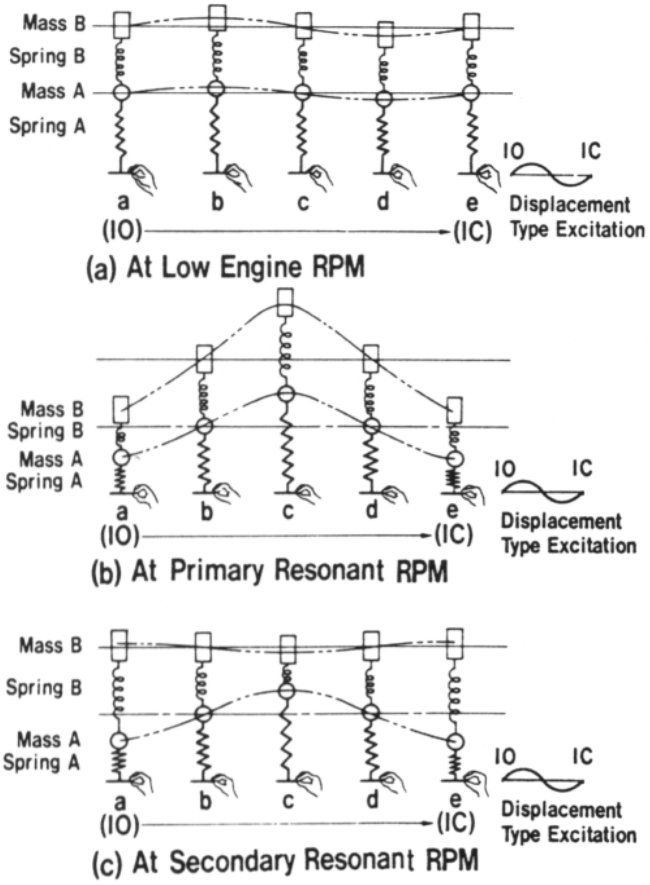

Figure 2-17: Modes of oscillation of 2nd Order system [9]

At the secondary resonant rpm, masses A and B are almost 90 degree out of phase. At this resonance rpm, less variance in the mass flow rate than at the primary resonant rpm is expected. This is because the direction of flow in the intake manifold and plenum chamber, as indicated by springs A and B, is always opposite though not necessarily equal. Reverse flow can be expected at the inlet valve due to these wave interactions.

2-1.8 Exhaust tuning effects

Although outside the scope of this study, an understanding of exhaust gas dynamics is important. It is inevitable that exhaust gases and the fresh inducted mixture will have some sort of interaction since some valve overlap occurs. It is thus important that this interaction does not have an undesirable effect on engine performance. In fact, exhaust gases can actually aid in the induction process. Smith and Morrison [5] and Blair [6] also cover this aspect of tuning in detail.

During the exhaust process in a four-stroke engine, the inlet valve usually opens before top dead centre (BTDC). During this valve overlap, the exhaust gas motion causes pressure waves that, depending on the exhaust pipe configuration and engine speed, can aid or restrict intake flow. Normal exhaust pipes for sports cars collect exhaust pulses from individual cylinders and combine them into a larger pulse, with a corresponding lower pressure behind the pulse. This low pressure actually helps in drawing more air/fuel mixture into the cylinder from intake manifolds. This is called scavenging. This wave phenomenon enables late inlet valve closing times, i.e., after bottom dead centre (ABDC), during the compression stroke because of the momentum of the incoming air. This momentum ensures better cylinder filling.

Exhaust tuning takes into account these effects to increase mass flow and requires an understanding of the mentioned processes. It is because of these interactions that tuned exhaust manifolds have a different configuration to original exhaust systems. Certain restrictions such as engine bay space influence the geometry of the exhaust system such that the final tuned system may not necessarily be the best system.

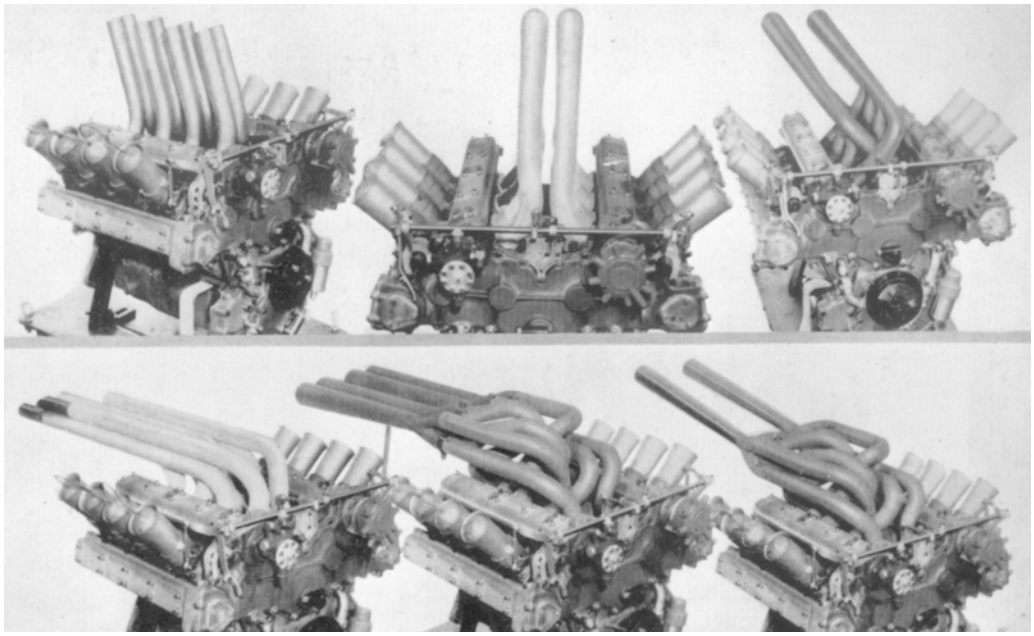

Figure 2-18: Experimental exhausts on Ford V-8 racing engine [5]

Figure 2-18 is an excellent example of good exhaust designs that cannot be practically implemented into a race car due to space limitations. However, such experimental

designs are still necessary in order to gain a better understanding of an engine's performance. These designs eventually lead to a final design that attempts to incorporate the most positive aspects of the experimental designs with some compromises due to limitations.

2-1.9 Variable back-pressure exhaust

Scavenging works best at certain engine speeds and this speed is fixed for different pipe lengths. That is; at low engine speeds, shorter pipes give the best scavenging performance and vice-versa at high engine speeds. It is because of this reason that an increasing number of modern super cars (e.g., Aston Martin Vanquish, Ferrari 550 Maranello, 360 Modena, Mitsubishi Lancer Evolution VII and Lamborghini Diablo 6.0) now employ the use of a variable back-pressure exhaust. This works in a similar manner to the variable intake manifold, the only difference being that it works to expel spent gases while the intake serves to provide fresh air mixture.

The system usually comprises two different lengths of exhaust pipes with a valve that can switch between them. The system can therefore satisfy both low and high-speed output requirements with reduced noise levels and harmful gas emissions.

2-1.10 Miscellaneous effects

Exhaust silencers and end-pieces have also been subject to design with the aim of reducing flow losses and hence ensuring lower pressures in the flow path. Reduction of these losses also ensures smoother passage of exhaust gases therefore requiring less piston work during the exhaust stroke.

Increased engine power output leads to increased stress on engine components and this aspect should not be overlooked when power increase is required as it could lead to severe engine damage. On the other hand, factory stock engines have a safety factor designed into them for power to be increased by a certain amount without much engine wear. However, because this engine threshold is difficult to determine except by test-to-failure methods, engine components expected to experience increased stress such as pistons, connecting rods, big-end bearings and cylinder head gaskets must be

replaced with stronger components. In the case of turbocharged engines with nitrous oxide, ceramic coating for various components such as pistons, valves, cylinder head and cylinder walls reduces wear and friction and also reduces heat build-up in the combustion chamber.

2-1.11 Prediction of engine intake pressure using numerical methods

Accurate numerical methods are required in order to correctly simulate the flow behaviour in a system. These methods aid in predicting some of the complex flow phenomena or processes that occur in an engine. Although 0-D and 1-D engine simulation techniques offer quick turnaround times when simulating pressure in the combustion chamber, these techniques do not give qualitative information about the flow such as squish, swirl or tumble flow. It is only recently that complex 3-dimensional processes such as combustion have been modelled, and simulated successfully in CFD [13], [14], [15].

However, where cost is a concern, these techniques do offer a viable option with an acceptable compromise between accuracy and cost. This can be achieved by coupling the 0-D or 1-D engine (such as EngMod4T® [16]) package to a CFD code with the pressure solution being updated at every time-step [17]. A cheaper alternative is to use pressure data extracted from these engine simulation codes and enforce it as a boundary condition in the CFD code. This has proved to be successful as demonstrated by results from PowerFLOW® 3.0 for an intake port with inlet valve lifts of 7 mm, 9 mm and 11 mm as seen in Table 2-2 [18]. The table shows that there is an excellent agreement between the PowerFLOW and experimental results.

Table 2-2: Comparison of PowerFLOW results with Experiment results [18]

	Volume Flow Rate (l/s)		Swirl Moment Ratio	
	Experiment	**PowerFLOW**	**Experiment**	**PowerFLOW**
7 mm	43.5	42.1	0.7	0.66
9 mm	46.5	47.6	1.00	1.00
11 mm	47.8	50.9	1.18	1.25

PowerFLOW® does not solve the Navier-stokes equations directly, but instead models the microscopic physics of the particles that compose the macroscopic fluid. This method contrasts with traditional CFD methods in that it works on the principle of simplifying microscopic behaviour while still achieving desired macroscopic behaviour. The particle distributions are represented with integers that allow the fluid dynamics to be processed exactly on digital computers. Although this fluid dynamics code does not take the traditional CFD approach, it is nevertheless worth mentioning.

It is also possible to realise engine performance improvement by the sole use of 1-D engine simulation codes as demonstrated by Wirtz and Mazzoni [19] and Papaconstantis [20]. These authors managed to achieve an improvement in power and torque of approximately 5 % to 7 %. The time taken for these simulations is only a fraction of the time that a CFD simulation would take, and thus 1-D simulations are desirable for quick and inexpensive results. The major drawback of 1-D simulation results is that they give the user no insight into the flow behaviour such as swirl and separation, which is the advantage that CFD has over these methods.

2-1.12 Combustion

Spark ignition internal combustion engine operation is illustrated by the Otto cycle [4]. This cycle describes the thermodynamic events that occur in a closed cycle but is however based on constant volume combustion, which is not the case in real engine operation. Combustion is thus modelled as a time-dependent process while taking into account the ignition-timing advance and the finite time required for combustion [6].

When a combustion mixture is ignited at 25° BTDC, there is an ignition delay of about 10° (i.e., from 335° to 345° crank angle). The actual period of heat release takes place over a burn duration, b, of approximately 50° (from 345° to 395° crank angle), over which the mass fraction of fuel burned has the profile as seen in Figure 2-19. This can be referred to as the phased burn cycle. In Figure 2-20, the ideal Otto cycle is compared to the phased burn cycle and the deviation is evident, with the phased burn cycle more suited for real engine operation. This process is implemented into 1-D engine simulation codes by taking into consideration the ignition advance, ignition delay period and duration of burn.

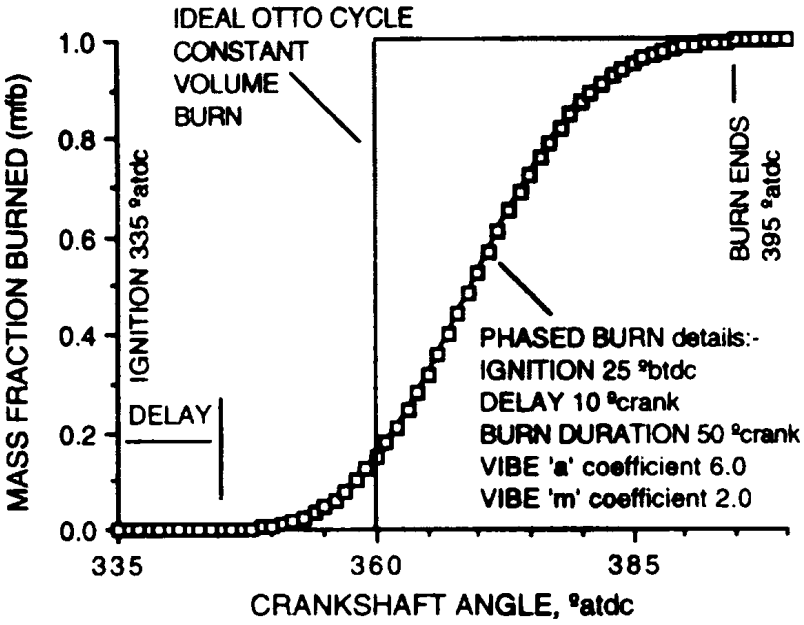

Figure 2-19: Phased burn combustion model [6]

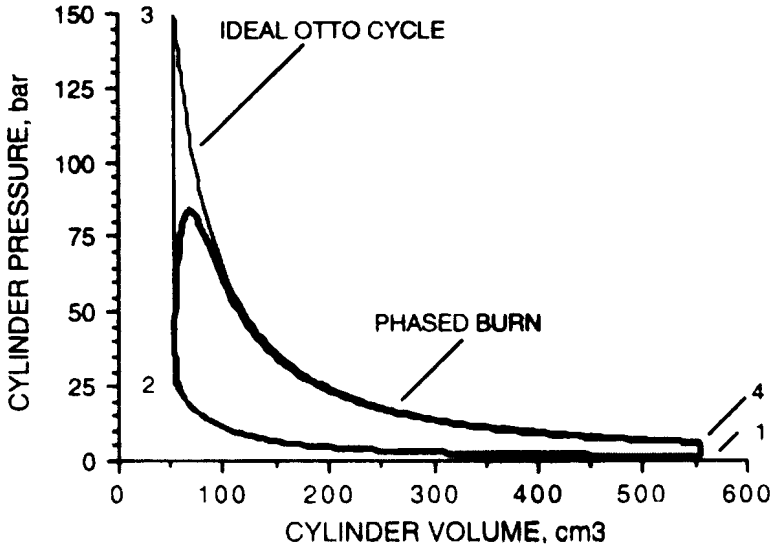

Figure 2-20: Ideal Otto cycle compared to the phased burn model [6]

2-1.13 Conclusion

In this section, the history and development of intakes as well as their function were presented. The equations describing wave behaviour in intakes were discussed as well as the theory behind tuning. These governing equations are important as they serve as the basis of the 1-D simulations that provide data for the CFD (discussed in the section that follows) simulations.

2.2 COMPUTATIONAL FLUID DYNAMICS

2-2.1 Introduction

Fluid flow is governed by the conservation of three fundamental quantities namely; mass, momentum and energy. The description of these conservation laws in mathematical form yields non-linear partial differential equations, which are famously known as the Navier-Stokes equations. Although these Navier-Stokes equations have been known since the 1800s, they have been too difficult to solve for arbitrary flows until the development of the modern computer. The science involved in solving these equations numerically on the computer is known as computational fluid dynamics (CFD).

In order to solve the Navier-Stokes equations, the flow domain for the specific problem is first discretised. Domain discretisation, using mesh or grid generating techniques, involves breaking up the selected control volume into smaller volumes and solving the Navier-Stokes equations over each volume. For simple geometries such as rectangular shapes, discretisation is simple but gets more difficult as the geometry becomes more complex. Also, to accurately capture flow phenomena such as turbulence, fine grids are required at the region of interest leading to an increased number of mesh elements. This results in a large system of non-linear equations requiring large computing memory. However, with the ever-increased computing capability available today, a lot of complex flow problems can now be solved.

Commercial CFD codes such as FLUENT, PHOENIX, CFX, CFD++ and Star-CD have also developed to a point that the user need not be an expert on CFD in order to successfully put it to use. The end-user must however have a good knowledge of fluid dynamics for a successful simulation with credible results to be obtained. Therefore, used correctly, CFD codes can reduce time and cost of experiments in product development or process improvement.

The rest of the chapter discusses the various areas of CFD in the following order:

- Governing equations
- Grid generation techniques

- Boundary conditions that define a CFD problem
- Solution algorithms and convergence criteria
- Basic background on the CFD solver used (FLUENT)

2-2.2 Governing equations

The governing equations of fluid behaviour are given in equations (2.24) and (2.25) [21], [22]. These equations are given for compressible flow, but can be easily simplified for incompressible flow. In the Eulerian system, the particle derivative is described as follows:

$$\frac{D}{Dt} = \frac{\partial}{\partial t} + \left(\vec{V} \cdot \nabla\right) \tag{2.24}$$

where:

$$\left(\vec{V} \cdot \nabla\right) = div\vec{V} = \frac{\partial u}{\partial x} + \frac{\partial v}{\partial y} + \frac{\partial w}{\partial z}. \tag{2.25}$$

This particle derivative will be used in the sections to follow to present the Navier-Stokes equations in conservative form.

2-2.3 Conservation of Mass

The equation for conservation of mass in conservative form is given as:

$$\frac{\partial \rho}{\partial t} + \nabla \cdot \left(\rho \vec{V}\right) = 0. \tag{2.26}$$

where ρ is the density and $\vec{V}$ is the vector velocity of the fluid.

2-2.4 Conservation of Momentum

The equations for conservation of momentum in the three Cartesian directions are presented.

$$\frac{\partial(\rho u)}{\partial t}+\frac{\partial\left(\rho u^2\right)}{\partial x}+\frac{\partial(\rho uv)}{\partial y}+\frac{\partial(\rho uw)}{\partial z}$$
$$=-\frac{\partial p}{\partial x}+\frac{\partial}{\partial x}\left(\lambda\nabla\cdot\vec{V}+2\mu\frac{\partial u}{\partial x}\right)+\frac{\partial}{\partial y}\left[\mu\left(\frac{\partial v}{\partial x}+\frac{\partial u}{\partial y}\right)\right]+ \tag{2.27}$$
$$\frac{\partial}{\partial z}\left[\mu\left(\frac{\partial u}{\partial z}+\frac{\partial w}{\partial x}\right)\right]+\rho g_x$$

$$\frac{\partial(\rho v)}{\partial t}+\frac{\partial(\rho uv)}{\partial x}+\frac{\partial\left(\rho v^2\right)}{\partial y}+\frac{\partial(\rho vw)}{\partial z}$$
$$=-\frac{\partial p}{\partial y}+\frac{\partial}{\partial x}\left[\mu\left(\frac{\partial v}{\partial x}+\frac{\partial u}{\partial y}\right)\right]+\frac{\partial}{\partial y}\left(\lambda\nabla\cdot\vec{V}+2\mu\frac{\partial v}{\partial y}\right)+ \tag{2.28}$$
$$\frac{\partial}{\partial z}\left[\mu\left(\frac{\partial w}{\partial y}+\frac{\partial v}{\partial z}\right)\right]+\rho g_y$$

$$\frac{\partial(\rho w)}{\partial t}+\frac{\partial(\rho uw)}{\partial x}+\frac{\partial(\rho vw)}{\partial y}+\frac{\partial\left(\rho w^2\right)}{\partial z}$$
$$=-\frac{\partial p}{\partial z}+\frac{\partial}{\partial x}\left[\mu\left(\frac{\partial u}{\partial z}+\frac{\partial w}{\partial x}\right)\right]+\frac{\partial}{\partial y}\left[\mu\left(\frac{\partial w}{\partial x}+\frac{\partial v}{\partial z}\right)\right]+ \tag{2.29}$$
$$\frac{\partial}{\partial z}\left(\lambda\nabla\cdot\vec{V}+2\mu\frac{\partial w}{\partial z}\right)+\rho g_z$$

These equations can be rewritten as a single vector equation using indicial notation:

$$\frac{D\rho\vec{V}}{Dt}=\rho\vec{g}-\Delta p+\frac{\partial}{\partial x_j}\left[\mu\left(\frac{\partial v_i}{\partial x_j}+\frac{\partial v_j}{\partial x_i}\right)+\delta_{ij}\lambda div\vec{V}\right] \tag{2.30}$$

2-2.5 The Energy Equation

The energy equation, which in essence is the first law of thermodynamics, is given in its most economic form as follows:

$$\rho \frac{D}{Dt}\left(e+\frac{p}{\rho}\right)=\frac{Dp}{Dt}+div\left(k\nabla T\right)+\tau_{ij}^{'}\frac{\partial u_i}{\partial x_j} \tag{2.31}$$

where the viscous stresses are given by the stress tensor:

$$\tau_{ij}^{'}=\mu\left(\frac{\partial u_i}{\partial x_j}+\frac{\partial u_j}{\partial x_i}\right). \tag{2.32}$$

2-2.6 Two-Equation Model: *k-ε Model*

Engineering flow problems encountered in CFD are often turbulent, thus requiring more effort to solve. Turbulent flows are described by disorderly (or 'chaotic') motion of fluid particles in space and time. The degree of unsteadiness of the flow is often subject to the complexity of the geometry. Flow fluctuations bring into contact particles of differing momentum resulting in velocity reductions due to viscous effects; subsequently the kinetic energy is reduced [23]. This process is said to be dissipative.

Turbulence also increases mixing of particles; thereby differing concentrations of conserved quantities are mixed. This process is called turbulent diffusion. Turbulence, depending on the application, can have desirable effects, for example; chemical mixing and increased wall heat transfer coefficients for better heat transfer rates than in laminar flow. In other applications, turbulence is required though it may lead to losses. Such an application is flow into the combustion chamber where mixing of fuel and air is desired, but because of turbulence, flow velocity is reduced.

Most compressible viscous flow is turbulent, thereby increasing the complexity of the governing equations. Direct numerical simulation (DNS) of turbulence is also computationally expensive; therefore the alternative is to model the phenomenon. Turbulence modelling is based on the principle that unsteady and irregular high-Reynolds-number flow averaged over time is steady and predictable. This principle

leads to a set of non-linear differential equations known as the Reynolds-Averaged Navier-Stokes (RANS) equations. For high-Reynolds number compressible flow; viscous and turbulent effects are only significant near the walls, as a result the turbulent models need only be applied to a small section of the computational domain.

Turbulent models comprise, in order of complexity, among others the zero-equation model, one-equation model (turbulent kinetic energy), two-equation model (e.g., k-ε model), Reynolds stress model (RSM) and large eddy simulation (LES). Direct numerical simulation is the highest level of turbulence simulation, as it requires the exact solution of the full Navier-Stokes equations without averaging or approximation. Since the cost of simulation is directly proportional to Re^3 [24] and also due to computer capability limitations, DNS is currently only possible for flows of low Reynolds (Re) numbers and simple geometrical domains.

As there are many suggested turbulence models today, only the best-suited model for each application need be used and for this study the k-ε model proved sufficient for the simulations. The k-ε model is a two-equation model coupling the turbulent kinetic energy equation with the equation for modelling the rate of change of dissipation (ε). The resulting two models are given below for fully elliptic high-Reynolds-number flow [21].

$$\frac{D\varepsilon}{Dt} \approx \frac{\partial}{\partial x_j}\left[\frac{v_t}{\sigma_\varepsilon}\frac{\partial \varepsilon}{\partial x_j}\right] + C_1 v_t \frac{\varepsilon}{k}\frac{\partial \bar{u}_i}{\partial x_j}\left(\frac{\partial \bar{u}_i}{\partial x_j} + \frac{\partial \bar{u}_j}{\partial x_i}\right) - \frac{C_2 \varepsilon^2}{k} \tag{2.33}$$

$$\frac{Dk}{Dt} = \frac{\partial}{\partial x_j}\left[\frac{v_t}{\sigma_k}\frac{\partial k}{\partial x_j}\right] + v_t \frac{\partial \bar{u}_i}{\partial x_j}\left(\frac{\partial \bar{u}_i}{\partial x_j} + \frac{\partial \bar{u}_j}{\partial x_i}\right) - \varepsilon \tag{2.34}$$

where $\sigma_k = v_t/v_K$ and $\sigma_\varepsilon = v_t/v_\varepsilon$ are effective "Prandtl numbers" relating eddy diffusion of k and ε to the momentum eddy viscosity. The eddy viscosity is modelled as follows:

$$v_t \approx \frac{C_\mu k^2}{\varepsilon} \tag{2.35}$$

where $v_t = \dfrac{\mu_t}{\rho}$

Recommended values for attached boundary layer calculations of the five empirical constants are given in Table 2-3.

Table 2-3: Recommended values for empirical constants [21][24]

C_μ	C_1	C_2	σ_k	σ_ε
0.09	1.44	1.92	1.0	1.3

The values in Table 2-3 are however, not universal and need to be modified for different problems such as jet, wakes, and recirculating flows. The combination of the equations (2.33) to (2.35), empirical constants in Table 2-3, continuity (2.26) and the momentum relations (equations (2.27) to (2.29)) yields a system of equations that are simultaneously solved with turbulent closure to as the *k*-*ε* model. Near the wall, the *k*-*ε* model is not valid and thus a curve-fit incorporating the laminar sublayer (law of the wall) and the logarithmic layer (log law), known as a wall function, is used. The *k*-*ε* computations begin at a certain distance y_p away from the wall. The log-law belongs to a class of models known as wall functions.

2-2.7 Near-Wall Treatment

Due to the viscous and sub-layer damping effects in the turbulent boundary layer, the Reynolds number is significantly lower in this region. At high Reynolds number flows, the *k*-*ε* model requires a very fine grid at the turbulent boundary layer to solve for the flow properties in this region. This is due to the fact that the boundary layer is very thin at high Reynolds numbers. Due to the computational effort a fine grid requires, wall functions are used near the wall.

The relations given in (2.36) are for the velocity profile in the turbulent boundary layer [24].

$$u^+ = \frac{\overline{v_t}}{u_\tau} = \begin{cases} n^+ & n^+ \le 5 \\ \frac{1}{\kappa}\ln\left(n^+\right) + B & n^+ > 30 \end{cases} \tag{2.36}$$

where $\overline{v_t}$ is the mean velocity parallel to the wall and u_τ is the shear velocity given by:

$$u_\tau = \sqrt{\frac{|\tau_w|}{\rho}} \tag{2.37}$$

where τ_w is the shear stress at the wall, κ is the von Karman constant ($\kappa = 0.41$) and B is an empirical constant related to the viscous sublayer ($B = 5$).

In equation (2.36), n^+ is the dimensionless distance from the wall given by

$$n^+ = \frac{\rho u_\tau n}{\mu} \tag{2.38}$$

In most literature n^+ is also referred to as y^+. The log-law is valid for: $30 < y^+ < 60$.

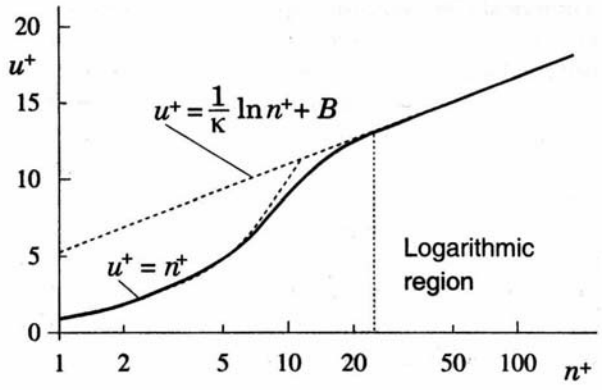

Figure 2-21: Velocity profile as function of distance normal to the wall in the turbulent boundary layer [24]

Figure 2-21 illustrates the velocity profile as a function of distance normal to the wall. Dashed lines are from corresponding equations whereas the solid line constitutes averaged experimental data.

2-2.8 Grid generation and GAMBIT

The grid generation process or meshing involves dividing the flow domain into smaller control volumes over which the discretised Navier-Stokes equations are solved. Grid (mesh) types can be classified into two categories namely; structured and

unstructured grids. The mentioned types of grids find use in different applications and are used in the meshing process in this study.

Structured grids consist of grid lines with a characteristic of not crossing or overlapping. The position of any grid point is uniquely identified by a set of two (2-D) or three (3-D) dimensional indices, e.g., (*i, j, k*). Unstructured grids make no assumption about any structure in the grid definition and usually consist of triangular (tetrahedral (tet) in 3D) elements.

A numerically generated structured grid or mesh, is understood here to be the organised set of points formed by the intersections of the lines of a boundary conforming to a curvilinear coordinate system. The prime feature of such a system is that some coordinate line (surface in 3D) is coincident with each segment of the boundary of the physical region.

The use of coordinate line intersections to define the grid points provides an organisational structure that allows all computations to be done on a fixed square grid when partial differential equations of interest have been transformed so that the curvilinear coordinates replace the Cartesian coordinates as the independent variables. This grid frees the computational simulation from restriction to certain boundary shapes and allows general flow solvers to be written in which the boundary shape is specified simply by input.

Grid generation for the purposes of this research takes place in FLUENT's [25] pre-processor, GAMBIT [26]. GAMBIT is a versatile pre-processor that can support a large variety of commercially available computer-aided design (CAD) platforms. Raw geometry can be imported from these CAD packages into GAMBIT where it is operated on (i.e., the necessary simplification for CFD purposes are made), in preparation for meshing.

Various meshing schemes are available in GAMBIT and are used where suitable in the grid generation process. Most of these schemes are unique to GAMBIT and are not necessarily documented, as they may be modifications of existing meshing schemes. GAMBIT allows the user to specify any volume to be meshed, although the

shape and topological characteristics of the volume determine which mesh schemes can be used.

Different meshing schemes such as Hex, Hex/wedge and Tet Hybrid, can be specified on volumes to be meshed. The Hex mesh is composed of hexahedral elements only constituting a fully structured mesh. The Hex/wedge mesh comprises mainly of hexahedral elements with wedge elements where necessary. However, Hex and Hex/wedge elements do not apply to any shape volume, as opposed to Tet Hybrid meshes. The versatility of the Tet Hybrid element makes it appreciable for use where the volume is complex and none of the other meshes can be applied. Solution inaccuracies associated with the Tet Hybrid element type are, however, more significant than for any of the other element types. Each element type is associated with a volume-meshing scheme and only those schemes used in this study will be discussed.

Cooper meshing scheme

When this scheme is enforced on a volume, GAMBIT treats the volume like a cylinder with end-caps. In the actual volume, the faces at these locations are representative of the end-caps and are called source faces as in Figure 2-22. They are so-called because their face meshes are projected through the volume after certain mesh operations have been performed by GAMBIT as is illustrated by Figure 2-24 (a) to (b).

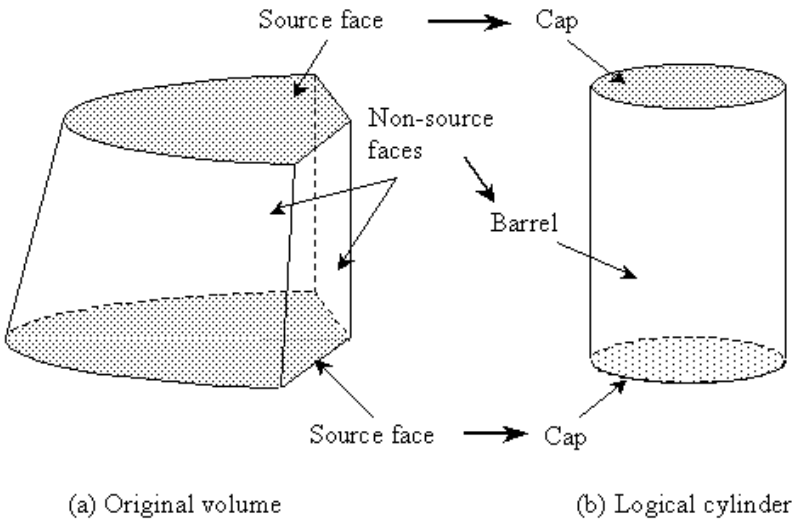

Figure 2-22: Cooper meshing scheme volume treatment [26]

The Cooper scheme involves, in order of occurrence, the following steps:

1. Meshing the non-source faces
2. Imprinting the source faces on one another
3. Meshing the source faces
4. Projecting the source faces' node patterns through the volume to produce a volume mesh

The steps described can be illustrated by the example in Figure 2-23, which shows the union of a prism, cylinder and a rectangle.

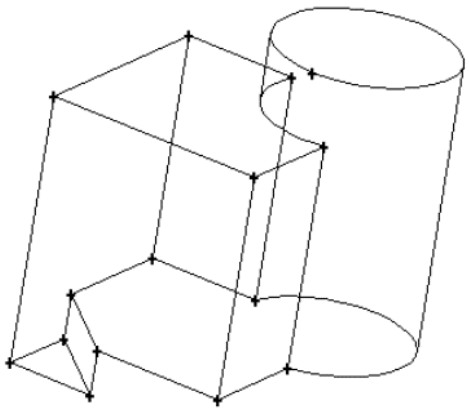

Figure 2-23: Union of cube, a cylinder, and a triangular prism [26]

The various Cooper mesh scheme steps are clearly illustrated in Figure 2-24.

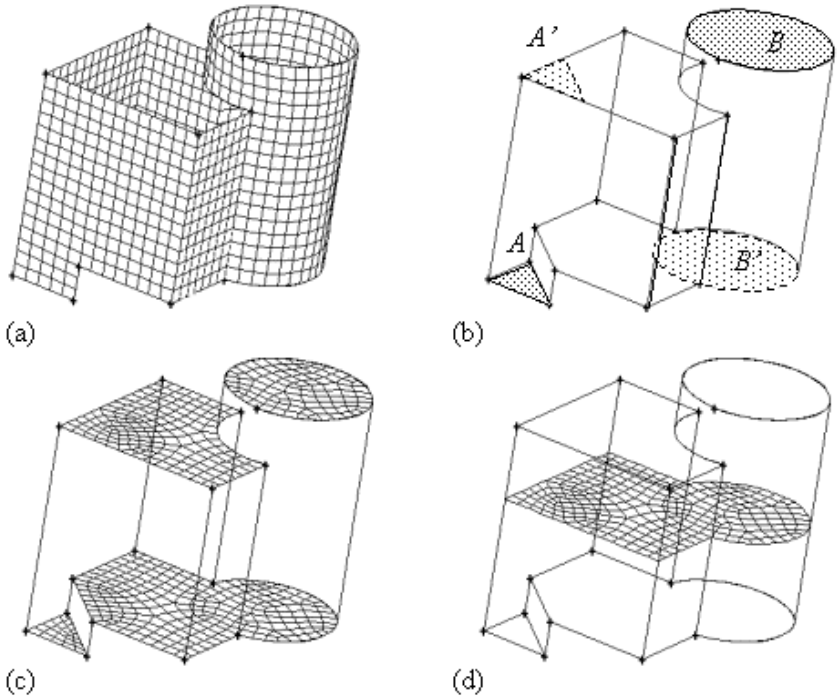

Figure 2-24: Cooper meshing scheme [26]

Figure 2-25 is a typical grid used in this research illustrating the different meshing schemes used.

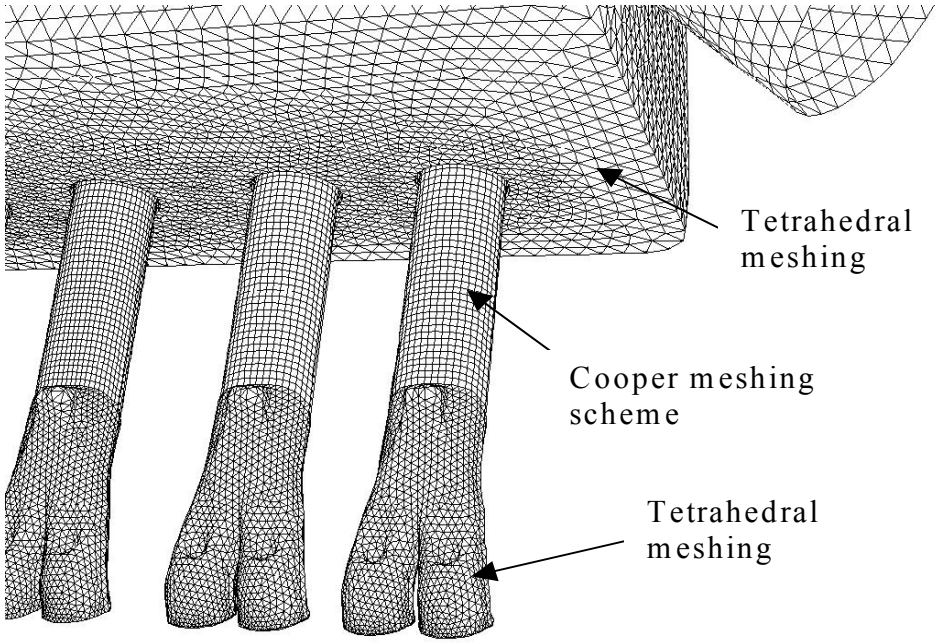

Figure 2-25: Illustration of meshing types used in the study

2-2.9 Boundary Conditions

Equations (2.26) to (2.31) presented in the preceding section remain the same regardless of the flow field, i.e., external flow, internal flow, two-phase flow (with some modifications), etc. In mathematics, any solution to a set of partial differential equations (PDE's) requires a set of boundary conditions for closure and the solution of the governing equations is no exception.

CFD simulations largely depend on the boundary conditions specified, hence correct boundary specification improves convergence to a correct solution. Incorrect boundary and initial conditions, however, can give convergence although not to a correct solution. There is a wide variety of boundary types available in FLUENT [25], but only those used in this study will be given.

1) **Flow inlet and exit boundaries**

   Pressure inlet: Used to define the total pressure and other scalar quantities at flow inlets.

   Pressure outlet: Used to define the static pressure at flow outlets (and also other scalar variables, in case of backflow). The use of a pressure outlet boundary condition instead of an outflow condition often results in a better rate of convergence when backflow occurs during iteration. Note that when backflow occurs, this boundary acts like a pressure inlet boundary.

2) **Wall and symmetry:**

   Wall: Used to define a solid-fluid interface where viscous flow is considered, thus applying a no-slip condition. The boundary condition on a surface assumes no relative velocity between the surface and the gas immediately at the surface.

   Symmetry: Used to define surfaces at which normal velocity and normal gradients of all other variables are zero. This boundary type is essential where the geometry is symmetrical in nature, and only half the domain is modelled.

2-2.10 Solution Algorithms

The governing equations of fluid flow are particularly difficult to solve because of their non-linear nature. Much work has been done in numerical methods to solve for these types of equations. Some proven and popular methods worthy of note are SIMPLE, SIMPLE-C, SIMPLER, QUICK and PISO [27]. These methods are appreciated because of their robustness when applied to a variety of problems. In this study, steady-state and transient flows are solved using the SIMPLE and PISO algorithms respectively.

The acronym, SIMPLE, stands for Semi-Implicit Method of Pressure-Linked Equations, and describes the iterative procedure by which a solution to discretised equations is obtained. This method is well suited to steady-state solution computation. The iterative procedure is the pseudo-transient treatment of the unsteady governing equations in a discrete form to obtain a steady-state solution. SIMPLE was introduced by Patankar and Spalding (1972) [27] and was described in 1980 by Patankar [27]. The SIMPLE algorithm has a limitation in that new velocities and corresponding fluxes do not satisfy the momentum balance after the pressure-correction equation is solved. As a result, the calculation must be repeated until the balance is satisfied. The PISO algorithm improves the efficiency of this calculation by performing two additional corrections namely, neighbour and skewness correction.

PISO, which stands for Pressure-Implicit with Splitting of Operators, is a pressure-velocity coupling scheme that is part of the SIMPLE family of algorithms. This scheme is based on the higher degree of the approximate relation between the corrections for pressure and velocity. In highly distorted meshes, the approximate relationship between the correction of mass flux at the cell face and the difference of the pressure corrections at the adjacent cells is very rough. An iterative process is required to solve for the pressure-correction gradient components along cell faces since they are not known beforehand leading to the introduction of a process named skewness correction [24]. Here, the pressure-correction gradient is recalculated and used to update the mass flux corrections after the initial solution of the pressure-correction equation is obtained. This process significantly reduces convergence difficulties associated with highly distorted meshes and allows FLUENT to obtain a

solution on a highly skewed mesh in approximately the same number of iterations as required for a more orthogonal mesh. The PISO algorithm is used in this study for calculation of the unsteady gas behaviour due to its efficient nature and suitability for transient computations as recommended in FLUENT [25].

2-2.11 Convergence

Convergence of a flow or heat problem can be judged by observing the normalised residuals. Residuals are numerical imbalances from the solved governing equations resulting from an incomplete solution during the iterative process. The solution process can be terminated when the normalised residuals fall below a specified value, which is generally 10^{-3}. However, in some cases even with the convergence criteria (as far as normalised residuals are concerned) satisfied, the solution may not necessarily be a correct one. To avoid such instances, quantities such as mass flow rate, static pressure and heat flux can be monitored at a location in the flow domain that is deemed to be important. The monitored quantity is observed until the change from iteration to iteration is negligible thus ensuring good convergence.

2-2.12 Background on the CFD solver used (FLUENT)

FLUENT is a finite volume (FV) solver that can handle a wide variety of flow problems such as external flow, internal flow, and two-phase flow. All modes of heat transfer can also be solved by the CFD code. This code is used for all CFD analyses throughout this study.

Modern CFD packages are user-friendly with improved user and code interfacing. Thus understanding the underlying principles of flow is important in order to put the code to good use. FLUENT has a facility for coding to make repetitive simulations, as in an optimisation loop, more efficient and hence save time. This facility makes use of a journal file, which is a file containing a list of text commands that set-up a CFD model and runs the simulation. Post processing can also be performed with the use of these journal files.

The code developers validate and verify chosen simulated flow cases (mostly from industrial users) against experimental data, consequently ensuring a validated code for users. Thus, the code is very suitable for a wide-variety of industrial problems including the one that is the subject of this study, as will be seen in the chapters that follow.

2-2.13 Conclusion

As discussed in this section, the solution to the Navier-Stokes equations cannot be determined analytically, hence it is solved at discrete points in the flow domain by an iterative process. The various important aspects of grid generation process were also discussed as well as boundary condition specification. Solution algorithms used in solving the governing equations were briefly discussed as well as the solution convergence. The code, FLUENT, used in the study was also discussed where its journal file function's efficiency was highlighted in being the main point making FLUENT suitable for optimisation problems. Mathematical optimisation and its application to CFD is discussed in the next section.

2.3 MATHEMATICAL OPTIMISATION

2-3.1 Introduction

Optimisation is a process that involves changing parameters of a design in order to arrive at a desired objective. One approach in design that is commonplace is changing the design until an improvement is achieved. However, this "optimisation" process based on intuition and experience does not always yield desired results. This is mainly due to the fact that some design objectives may cross-influence one another and intuitively manipulating these objectives may prove to be an impossible task. This has led to the development of mathematical optimisation techniques to complement the design process. In this study, these techniques are applied to the airbox design in order to achieve a design that would give the maximum airflow through the intakes.

Complex non-linear multidisciplinary optimisation problems are often encountered and with ever-improving computer performance, it has become feasible to solve these problems. These problems are, however, often sensitive to design changes and inherent computer round-off errors, due to memory limitations. These may make it difficult to obtain the function gradients necessary for finding the optimum.

Response surface methodology *(RSM)* [28] is one optimisation methodology that is statistical in nature. RSM constructs smooth approximations to functions in a multi-dimensional space. By selecting optimally placed designs throughout the design space, RSM constructs approximate surfaces thereby reducing local noise effects. This method allows the designer to fully exploit the global information, giving freedom to try alternative design formulations. For example, the design response can be fixed while minimising or maximising other design criteria. The latter process can be reversed, whereby constraints are varied and the response to the changes is monitored.

Successive response surface methodology (SRSM) [29] is used in this study in an attempt to maximise the airflow through the four engine intakes, by shrinking the design space and formulating successive sub-problems thereby "zooming-in" on the optimal design. Use is made of a software package LS-OPT [30] that has the response

surface methodology (RSM) as its base optimisation method. A formal introduction to optimisation and problem formulation is given in the sections that follow.

2-3.2 Theory of optimisation

Mathematical optimisation is used to find the optimal values of selected design variables to obtain the minimum or maximum of an objective function. In more complex problems, more than one objective function is necessary, thus making the process computationally expensive. Design variables, $\boldsymbol{x}=(x_1, x_2, \ldots, x_n)^T$, are parameters that can vary within a specified design range and are mostly subject to constraints or bounds.

The general standard mathematical form of the above paragraph is presented as follows:

$$\text{minimise } f(\boldsymbol{x}),\ x \in R^n$$

subject to

$$g_j(\boldsymbol{x}) \le 0,\ j = 1, 2, \ldots, m$$

and

$$h_k(\boldsymbol{x}) = 0,\ k = 1, 2, \ldots, p$$

where f, g and h are functions of design variables $\boldsymbol{x}=(x_1, x_2, \ldots, x_n)^T$. $f(\boldsymbol{x})$ is the objective function which is the quantity to be maximised or minimised. The functions $g(\boldsymbol{x})$ and $h(\boldsymbol{x})$ are the inequality and equality constraints respectively.

2-3.3 Response surface methodology

The single-most important requirement of the response surface method is the analysis of design points to determine their response. Since simulation-based problems can be expensive and time-consuming to evaluate, it is desirable that the design set be chosen appropriately in order to be as efficient as possible. Use of made of the theory of experimental design (Design of experiments or DOE), of which LS-OPT uses the *D*-optimality criterion [30]. The following formulation of a least-squares problem will

provide understanding of the working of the successive response surface methodology (SRSM) that is used throughout the study.

Assume a single response variable y having independent variables $\boldsymbol{x}$. The *exact* relationship between these quantities is given by

$$y = \eta(\boldsymbol{x}) \tag{2.39}$$

If the functional relationship is now approximated (e.g., polynomial approximation), it follows that

$$\eta(\boldsymbol{x}) \approx f(\boldsymbol{x}) \tag{2.40}$$

The approximating function f is assumed to be a summation of basis functions:

$$f(\boldsymbol{x}) = \sum_{j=1}^{L} b_j \phi_j(\boldsymbol{x}) \tag{2.41}$$

where L is the number of basis functions ϕ_j used to approximate the model of interest.

The sum of the square error to be minimised is given by the following

$$\sum_{p=1}^{P} \left\{ [y(\boldsymbol{x}_p) - f(\boldsymbol{x}_p)]^2 \right\} = \sum_{p=1}^{P} \left\{ [y(\boldsymbol{x}_p) - \sum_{j=1}^{L} b_j \phi_j(\boldsymbol{x}_p)]^2 \right\} \tag{2.42}$$

where P is the number of sampling points, y is the exact functional response at the sampling points $\boldsymbol{x}_j$ as given in equation (2.42) and $\boldsymbol{b} = [b_1, b_2, \ldots, b_L]^T$ are unknown constants to be determined whose solution is

$$\boldsymbol{b} = (\boldsymbol{X}^T \boldsymbol{X})^{-1} \boldsymbol{X}^T \boldsymbol{y} = \boldsymbol{C}\boldsymbol{X}^T \boldsymbol{y} \tag{2.43}$$

$$\text{where } \boldsymbol{X} = [X_{uj}] = [\phi_j(\boldsymbol{x}_u)]. \tag{2.44}$$

In a linear approximation, used in the study, the relative value of each coefficient b_i represents the relative importance of the corresponding variable x_i. Therefore, a variable with a small value of b_j and/or a large confidence interval becomes a

candidate for screening; hence only significant variables are retained for the optimisation cycle.

The number of simulation points, $\boldsymbol{P}$, is selected using the formula $\boldsymbol{P} = \text{int}[1.5(n+1)]+1$ where n is the number of selected design variables. To obtain a best estimate of the coefficients b_i in the vector $\boldsymbol{b}$, the D-Optimality criterion is employed to determine the location of the P simulation points.

The successive response surface method (SRSM) constructs linear response surfaces on a subdomain from the subset of sampling points selected using the D-optimal criterion. The resulting successive sub-problems are solved with a multi-start variant of the leapfrog dynamic trajectory method, LFOPC [31].

The subdomain (or subregion) size is adjusted every iteration as the optimum is approached by shrinking and panning as seen in Figure 2-26. Design points falling outside of the subdomain space are handled by constructing an auxiliary problem to minimise infeasibility and bring the design within the feasible design region.

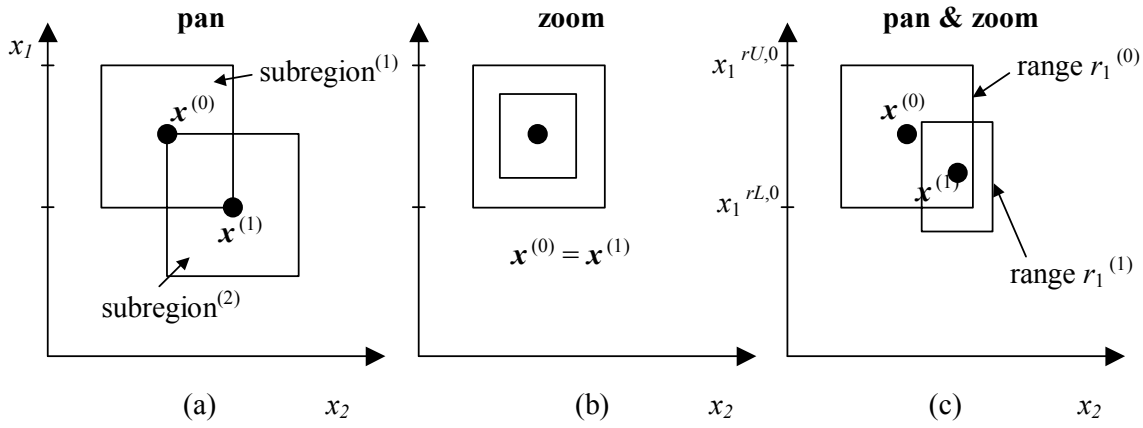

Figure 2-26: Progression of subregion in SRSM: (a) Only panning, (b) Only zooming and (c) a combination of panning and zooming [30]

In Figure 2-26, $\boldsymbol{x}^{(0)}$ is the starting design point that is at the centre of the design region. The user specifies the initial design range value $r_i^{(0)}$ that is used to determine the lower and upper bounds of the design subregion, ($x_i^{rL,0)}$, $x_i^{rR,0)}$). The size of each

successive subdomain is established through the use of a contraction and a zoom parameter.

2-3.4 Computational flow optimisation

The emergence of affordable and powerful computers has encouraged the growth of what is called computational flow optimisation (CFO). This is a field of computational science where computational fluid dynamics (CFD) and mathematical optimisation are used in tandem to find solutions to complex flow problems. These are largely simulation-based problems that tend to be cumbersome and computational intensive to find solutions to.

Numerous CFO problems have been successfully tackled through the use of different optimisation techniques such as gradient-based methods, neural networks and successive response surface methods. Craig *et al,* [29], [32]-[36], and Kingsley [37] have also successfully used CFO to find solutions to problems ranging from reduction of head injury during a car crash [29], to the reduction of automotive pollution in an urban environment [35].

When describing an engineering flow problem as an optimisation problem, care must be exercised in the selection of the objective function as well as the design variables. Insight is required in this regard so as to avoid over-defining a problem by, for instance, selecting too many design variables or constraints. The more design variables involved, the more computationally expensive it becomes to complete the optimisation, thus variables with little effect on the objective function should be ignored in the optimisation. The following steps are general steps of a simulation-based CFO problem using SRSM as the optimisation technique.

- Specify the design variables and constraints.
- Specify optimiser settings, e.g., order of approximation, affordable number of points.
- Simulate the base (initial) case objective function value in CFD. The optimiser gives suggested designs by perturbing the initial the design parameters within

the design space and the function values of the suggested designs are evaluated.

- Build a surface function through the obtained objective function values and then find the minimum point on the surface by using the LFOPC optimisation algorithm. The optimiser also gives predicted responses at the optimal design.

As the design space is shrunk, the above process is repeated until the objective function satisfies specified convergence criteria. The objective function can be subject to numerical noise that can be caused by grid resolution, data extraction from the completed solution or computer round-off errors. Therefore the SRSM is ideal for use in simulation-based problems (e.g., CFD) because of its robustness.

2-3.5 Conclusion

This section provided background on mathematical optimisation and one of the methods, the successive response surface method (SRSM) implemented in LS-OPT, was presented. The SRSM combined with CFD, together making up a CFO system, forms the basis of the optimisation study in the chapters that follow.

CHAPTER 3 : Intake Modelling

3.1 PROBLEM DEFINITION AND APPROACH

3-1.1 Problem definition

The intake system considered in this study is that of a Toyota Celica 2000cc Double Overhead Cam (DOHC) engine. The individual intake system components are shown in Appendix A. The standard production intake (not shown) has been modified for improved induction by making use of a series of "ram" pipes starting from the lower part of the front bumper extending all the way to the airbox. Modifications have also been made to other components of the engine, but are outside of the scope of this study.

The objective of the exercise is to solve the fluid flow at wide-open throttle (WOT) through the trumpet, front cover and body manifold (comprising two intake valves; and a single injector); collectively called the *intake* (shown in Figure 3-1). Similar work has been performed before by Craig and de Kock [38], [39], but in this study the boundary conditions are more detailed (as discussed further in this section) and therefore are expected to provide more accurate results.

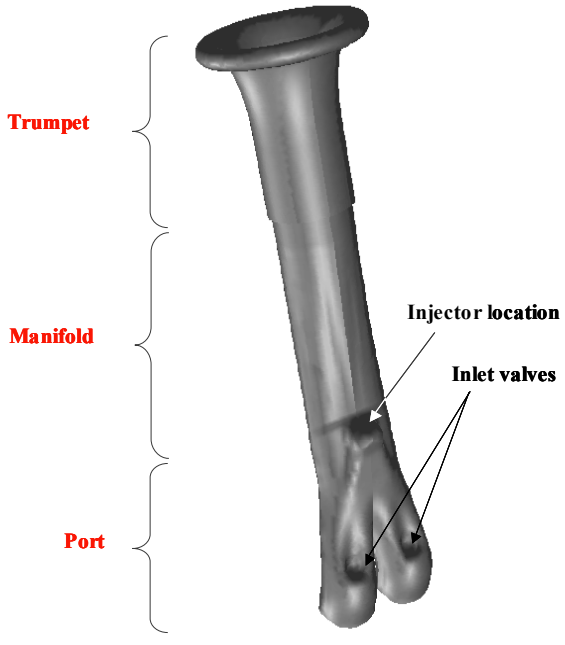

Figure 3-1: Rendered 3-D Single intake showing components

It is required that from the CFD solution the following be determined:

- The mass flow rate into the head.
- The flow behaviour in the intake due to transient effects.

The engine speed considered for the simulation is 6500rpm and is the speed at which the input pressure and temperature data are obtained. These input data used at the manifold outlet are obtained from a simulation for the considered geometry in the four-stroke engine simulation package EngMod4T [16]. EngMod4T is based on the 1-D gas dynamics equations with simplifications, as described in section 2-1.5, and correlations for complex 3-D flow phenomena.

3-1.2 Modelling Approach

The modelling approach taken in this study was of a bottom-up nature, whereby the system is modelled from the simplest set-up to the most complex arrangement as limited by computational resources. This was done in three steps as follows; a single intake without airbox, four intakes also without the airbox and finally the airbox was included for a more comprehensive analysis. Due to limited computational resources, only the section from the cylinder head up to the airbox inlet was considered for the CFD modelling. By excluding all the geometry (i.e., pipes, air-filter, etc.) downstream of the airbox, and then assuming the flow conditions at the airbox inlet, a lot of time was saved through modelling. The modelling of air mixed with the fuel at the injection point is difficult, and thus an assumption was made that the flow medium is homogenous air. In sections that follow, the same approach to the simulations was employed with the only difference being the model as discussed next.

Firstly, a converged second-order steady-state CFD solution was obtained by assuming a pressure drop across the intake. The purpose of the steady-state solution was to initialise the flow in the intake before the unsteady solution was computed, and also to obtain the outflow temperature boundary condition.

For the unsteady flow computation, the pressure outlet boundary was changed to a varying pressure boundary, with the pressure data obtained from EngMod4T

(described in the next section) used as an input. To ensure periodic flow, five engine cycles (5x720° crank angle) were solved to ensure cyclic behaviour. Figure 3-2 below shows the history of the pressure at the inlet valve against flow time for five engine cycles.

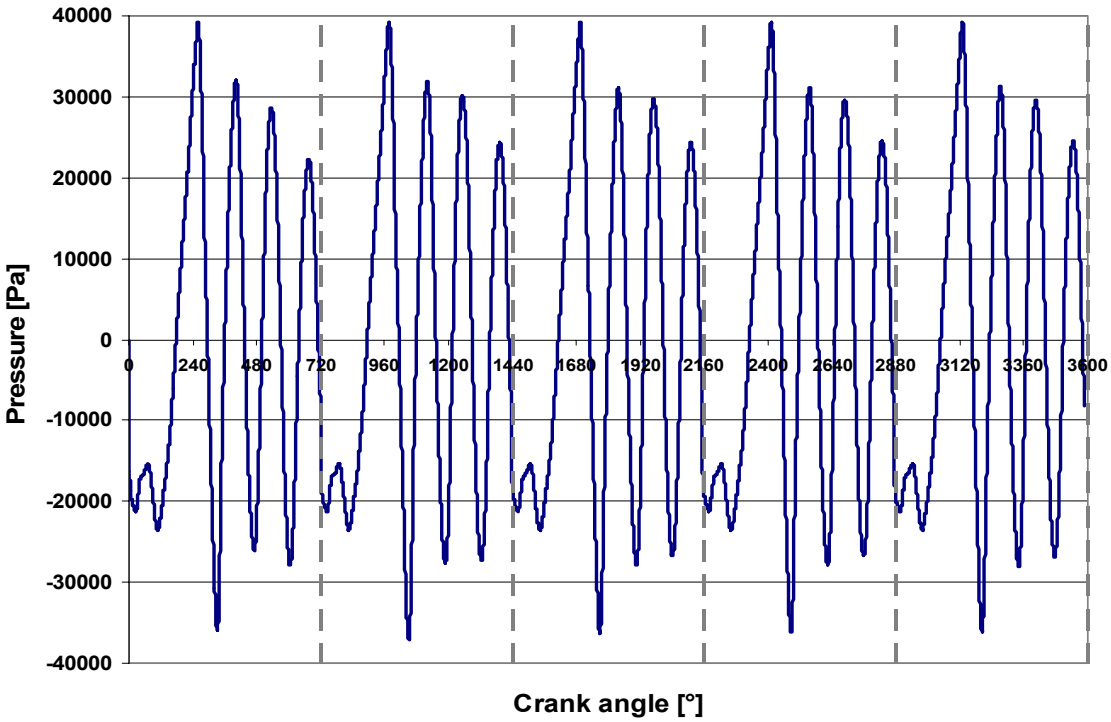

Figure 3-2: History of average pressure at inlet valve (Base design)

The broken lines on the plot depict the end of an engine cycle, and it can be seen that the pressure profiles become similar from cycle to cycle. At this point the flow was considered periodic and thus the pressure repeatable from cycle to cycle. This can be referred to as cyclic convergence. For all the CFD simulations that follow, it was ensured that cyclic convergence was achieved.

The computed unsteady mass flow rate and pressure at the exit of the inlet port are monitored and written to a file, where after the total mass inducted was computed and used as the single-most important factor of the CFD output. Where the geometry has more than one intake, each one was monitored and the combined effect was used as the final quantifying factor.

3-1.3 EngMod4T

During an engine cycle, the pressure at the inlet valve is unsteady due to pulsing and other effects. The time-variant pressure data are obtained from the four-stroke engine simulation package, EngMod4T [16], which simulates a full engine cycle for a specified number of cylinders. Input to the program includes parameters such as the exhaust system configuration, compression ratio, inlet/exhaust valve geometry, valve timing, firing order, etc., that fully define a combustion engine's configuration and operation.

Table 3-1 lists some of the input data used for EngMod4T. A more complete table (Table B-1) can be seen in Appendix B. The exhaust configuration with the dimensions required for input into EngMod4T is also shown in Figure B-1 (Appendix B).

Table 3-1: Summary of input data into EngMod4T

Bore	86.00 mm
Stroke	86.00 mm
Conrod length	148.00 mm
Compression ratio	13.5:1
Exhaust temperature	800 °C
Firing order	1-3-4-2
Valve open	0 – 0.007213 s
Valve close	0.007213 – 0.018593 s
Engine cycle time	0.018593 s

Figure 3-3 and Figure 3-4 below show the simulated pressure and temperature respectively, as given by EngMod4T, at the inlet valve during the valve open period. Although the outputs from the program are given with respect to the flow time, they are plotted against crank angle for easier interpretation.

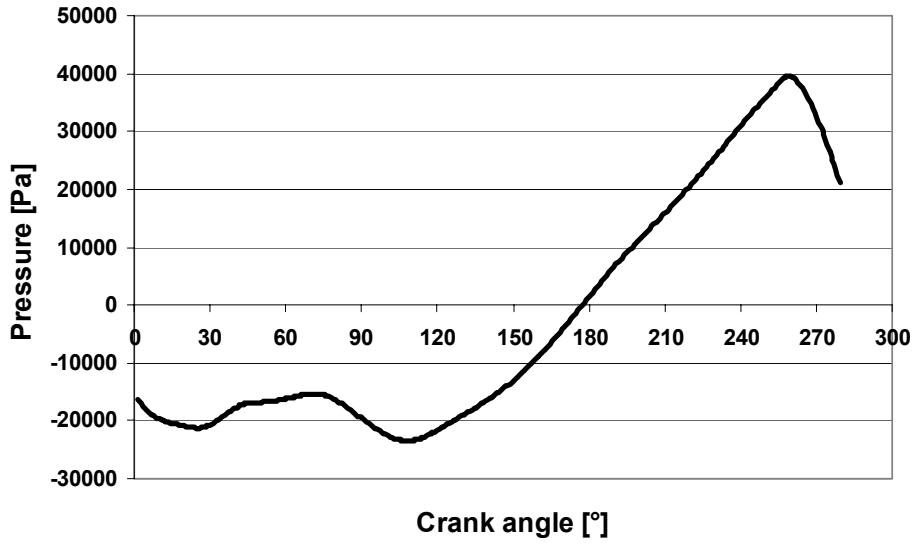

Figure 3-3: Pressure at the inlet valve as simulated by EngMod4T (valve open)

The temperature boundary condition is only used when reverse or backflow occurs at the inlet valve. Otherwise, when flow enters the inlet valve (i.e., leaves the computational domain), the temperature at this boundary is calculated from the interior of the domain. Once the valve closes, an adiabatic wall boundary condition is applied at the inlet valve boundary.

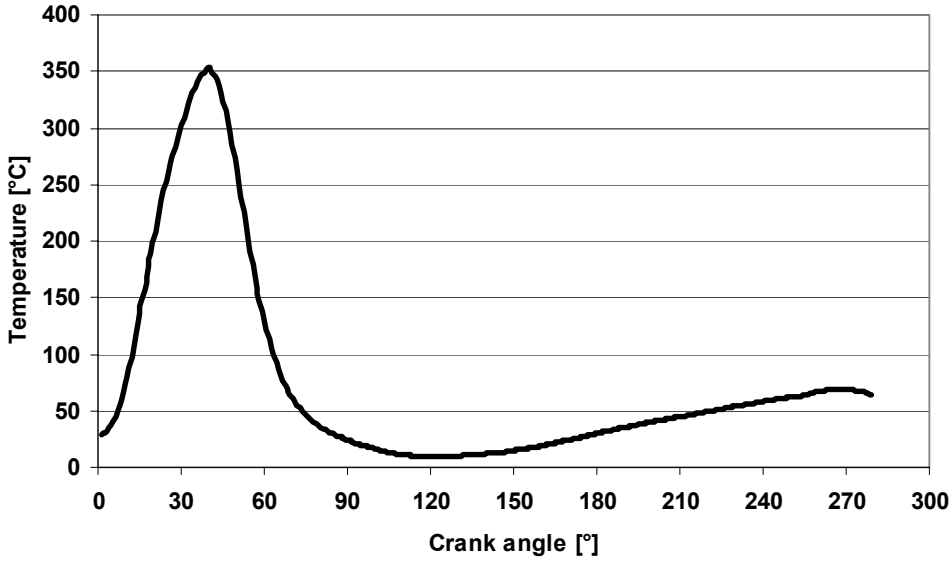

Figure 3-4: Temperature at the inlet valve as simulated by EngMod4T (valve open)

Note that the same pressure and temperature data, i.e., Figure 3-3 and Figure 3-4, are used throughout the study for all the model configurations. The motivation for using the same data was obtained though a sensitivity study conducted in EngMod4T, as shown in Figure 3-5. As shown in the figure, the pressure is only slightly sensitive to changes in operating intake geometry. The pressure was observed for large and small volume airboxes (volume determined from constraints of the optimisation study in section 4-2.2), as well as for the case where the intakes are open to the atmosphere, i.e., no airbox.

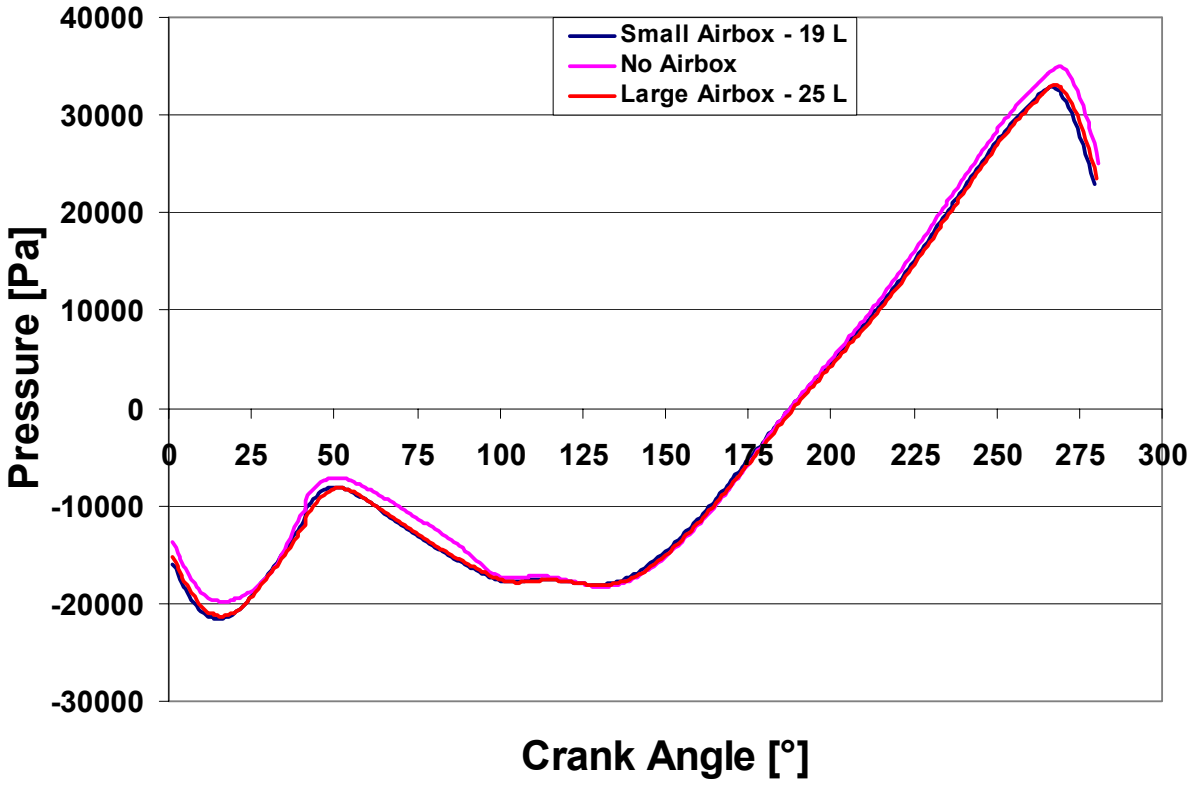

Figure 3-5: Sensitivity of inlet valve pressure to intake geometry changes

From the above results, it was decided to use the airbox pressures, as the simulations are conducted mainly on geometry containing airboxes. It is believed that the error being made by assuming the same pressure history is negligible.

3.2 SINGLE INTAKE WITHOUT AIRBOX

3-2.1 Grid Generation

The trumpet and the manifold were created in GAMBIT [26] from supplied technical drawings. The port, however, had to be scanned because of its complexity. Supplied scanned data (in DXF format, later converted to IGES) of the inlet port was used to generate the 3-D CAD drawing. *Aztech CNC Manufacturing Solutions* obtained the data by scanning an inverse of the silicon mould of the inlet port using a *Cyclone Series II* scanner from Renishaw [40]. The software used to get the scanned data to surfaces is *Paraform 2.1* [41]. The surfaces were then exported to GAMBIT, where a volume was generated by adding the trumpet and manifold. Refer to Figure 3-1 for the rendered 3-D illustration of the intake geometry.

The grid of the volume was generated in GAMBIT, where the grid was expanded at the trumpet inlet to allow for the proper boundary specification. Due to symmetry, only half of the volume was meshed. The expanded half-spherical domain was added to minimise the influence of the inlet boundary condition on the flow in the trumpet. In section 3.4, a more realistic airbox is used together with multiple intakes (cylinders). The number of grid cells was in the order of 216000. Different views of the grid can be seen in Figure 3-6, Figure 3-7 and Figure 3-8. The grid was then imported into the Computational Fluid Dynamics (CFD) package, FLUENT for case set up and solving for the flow.

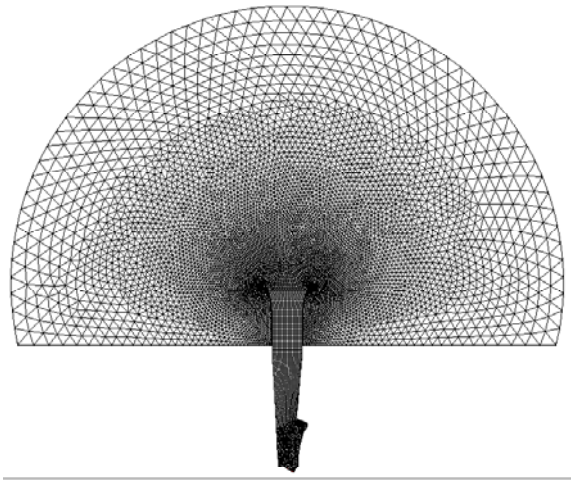

Figure 3-6: Overall grid of single intake model

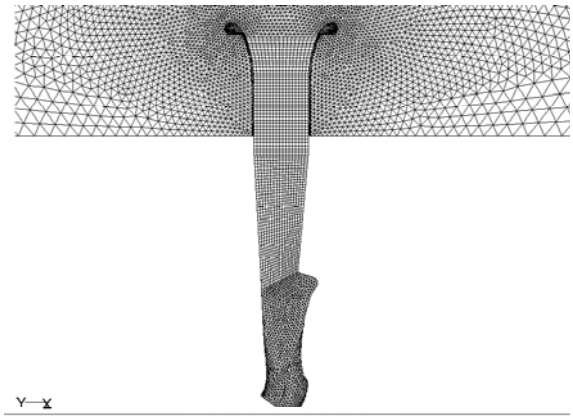

Figure 3-7: Zoomed-in view of intake

Where possible, a structured mesh was used like in the manifold section. The mesh consisted mainly of tetrahedral elements mostly in the domain representing the atmosphere. The mesh gets denser from the outside of the domain towards the trumpet vicinity so as to capture important flow features especially during unsteady simulations. Tetrahedral elements were also used in the inlet port section because of its irregular geometry as shown in Figure 3-8.

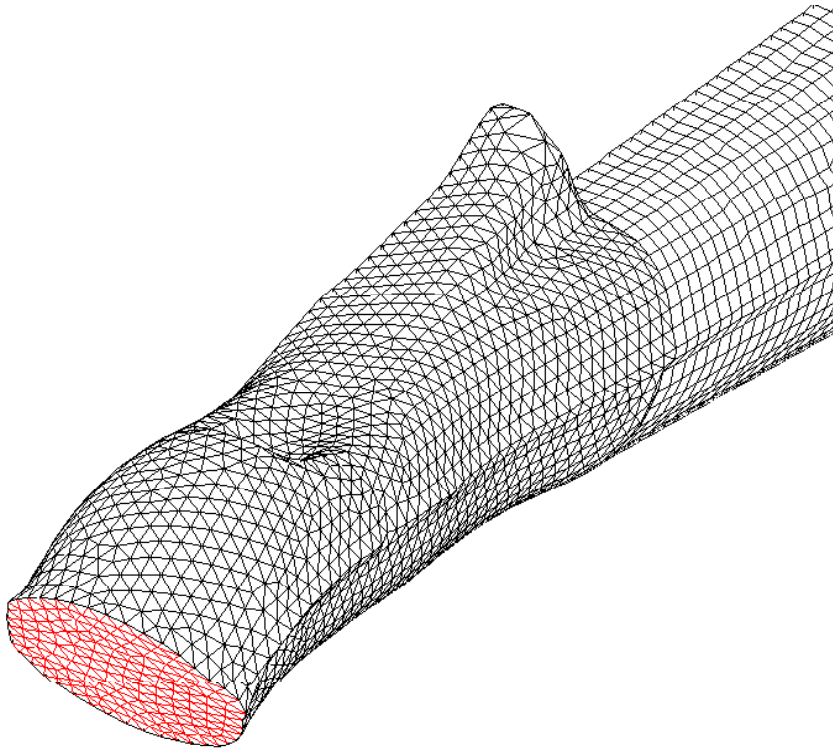

Figure 3-8: Close-up of surface grid at the inlet port

The mesh at the inlet port is dense so that the flow is this area is resolved to finer detail than in other areas of the computational domain. Since tetrahedral cells are known to give less accurate results than hexahedral cells, the use of fine cells provides increased accuracy at the expense of a high cell count. In the boundary layer area, more tetrahedral cells are required to get same accuracy as lesser number of hex cells.

3-2.2 Boundary Conditions

Two pressure boundaries were specified at the inlet and outlet of the intake with a specified pressure drop for the initial steady-state CFD simulation as seen in Figure 3-9. The pressure inlet boundary is used to represent atmospheric pressure. It is for this reason that it is placed far from the trumpet mouth to avoid boundary interference. At the pressure outlet boundary, a pressure drop is specified to initiate intake flow.

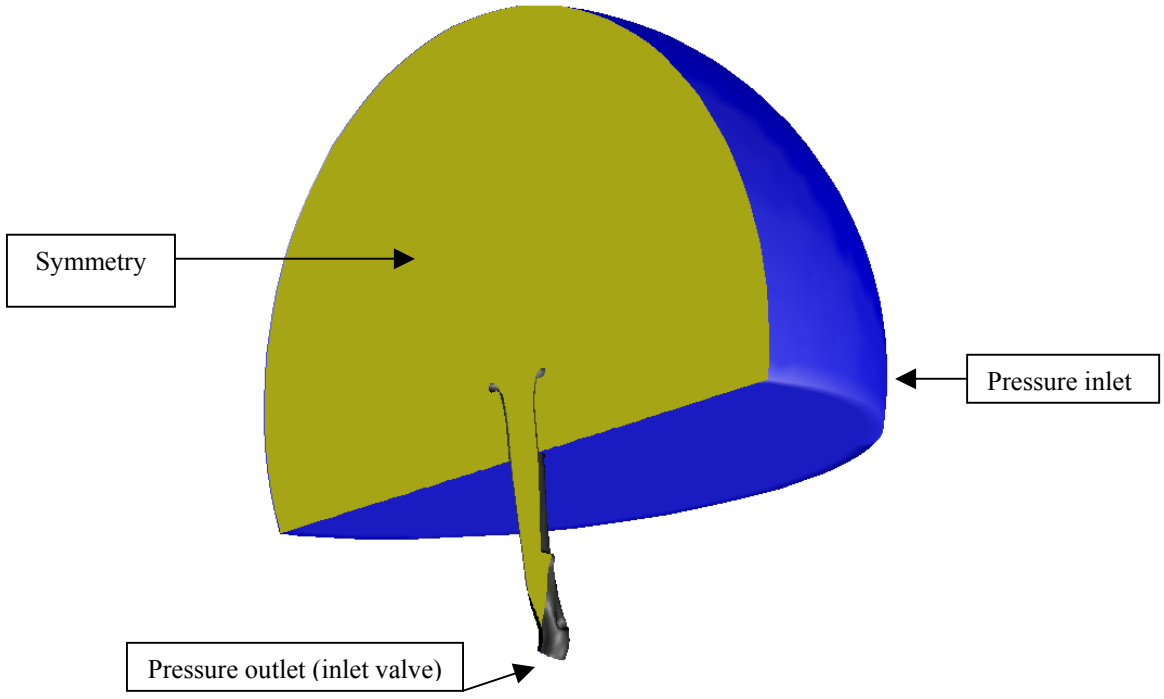

Figure 3-9: Rendered view showing boundary types by colour

3-2.3 Results and Discussion

The simulation performed in this section will be used mainly for comparison purposes as the complexity of the simulations increases. Therefore only the mass flow rate

result will be discussed, as the pressure and velocity results are more relevant in the full intake simulations in the sections that follow.

Mass flow rate

The mass flow rate at the inlet valve (outlet of CFD domain) is shown below in Figure 3-10. Negative mass flow corresponds to flow into the head. Therefore, ideally, the entire flow rate plot should be below zero, implying no backflow. From Figure 3-10, it can be noted that there is evidence of backflow as seen by the positive flow rate section of the graph towards the end of the intake cycle. The losses due to this backflow are undesirable and thus the valve opening could be timed such that it closes when the pressure is at its peak (about 250° crank angle), to retain the high-pressure pulse inside the cylinder.

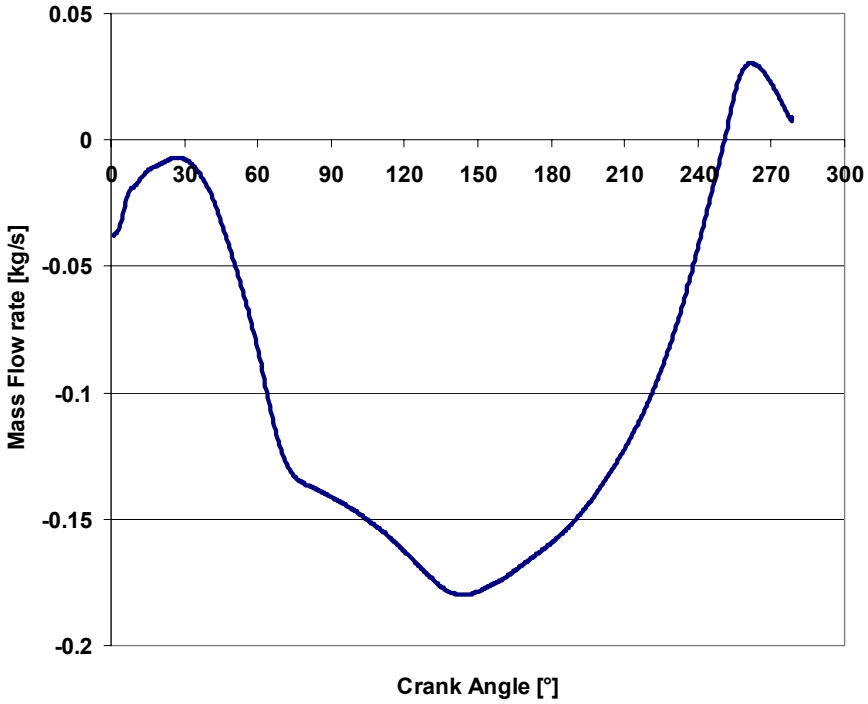

Figure 3-10: Mass flow rate at the inlet valve from the CFD simulation

The mass flow into the single intake can be extrapolated to give the total mass flow into a full engine intake system. This results in a total inducted air mass of 2.751 g. However, an assumption that the flow is equal for all intakes was necessary in order to make the extrapolation. This assumption is however flawed since there it does not account for the different flow losses that might occur from intake to intake.

3-2.4 Conclusion

This section showed results for a base case of the intake geometry of a high performance rally engine. The main result of the study is the mass flow rate, which showed that further improvements could be made by reducing the amount of backflow. The valve opening timing could serve as a good starting point in increasing the mass flow rate into the cylinder. Furthermore, ensuring a smoother transition between the injector point and the port body could reduce flow losses. To obtain more accurate results, all four intakes will be considered in the next section (four-cylinder engine) to gain insight into the effect that the intakes have on one another.

3.3 FOUR INTAKES WITHOUT AIRBOX

In order to understand the impact of an airbox on engine performance, the next configuration considered is that of an engine with the trumpets open to atmosphere. This is necessary since some engines perform better without an airbox at some speeds and also because an airbox has a characteristic of restricting wave expansion and travel. This characteristic can be positive at higher engine speeds where wave reflection against the airbox walls assists in charging because of the shorter wavelengths.

The geometry considered in section 3.2 is extended to four intakes due to the expected influence of the intakes on one another. Also, a volume is added above the intakes to allow for pulses to travel into the atmosphere. Due to the firing order being taken into account, intake charge "robbing" is expected. Charge "robbing" is the phenomenon that occurs when the inlet of an intake opens while one of the other intakes is open. This leads to a reduction in available charge mass to the latter. Three dimensional flow effects as well as intake robbing are expected to change the mass flow rate as predicted in the previous chapter.

3-3.1 Description of Problem

The gas flow at wide-open throttle (WOT) in the intake is solved. It is required to determine the following:

- The mass flow rate into the head.
- The flow profile in the intake due to pulsing.

The geometry considered is the four trumpets as in the real engine. The firing order (1-3-4-2) is also taken into account, and is used to determine the order of the valve openings.

As in the previous section, the engine speed considered for the simulation is 6500rpm and the same pressure data are also used as an input, although for each intake the pressure data is unique as given by EngMod4T.

3-3.2 Grid Generation

Due to the asymmetrical arrangement of the four intakes, the full geometry is modelled. Figure 3-11 shows a solid rendering of the four-intake arrangement. The grid was also expanded to allow for the implementation of the atmospheric boundary condition as a mock representation of the surrounding volume of air as seen in Figure 3-12.

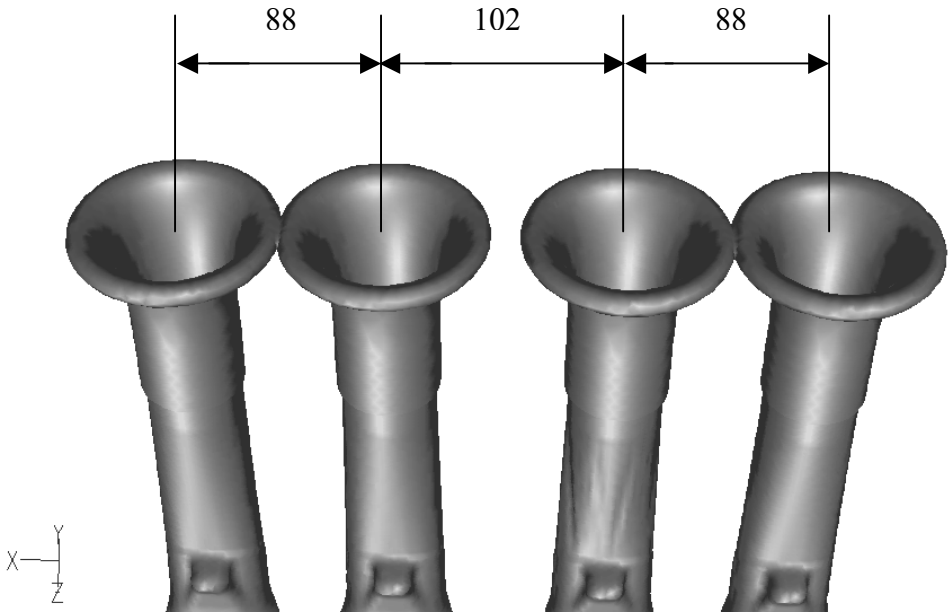

Figure 3-11: Solid rendering of four-intake arrangement [mm]

The surface grid is shown in Figure 3-12. Grid cells in the dome geometry (containing the inlet boundary) get coarser further away from the trumpet because the flow in these regions is not expected to have much of an effect on the flow in the intake. The grid contains around 460 000 cells. A close-up of the mesh is shown in Figure 3-13.

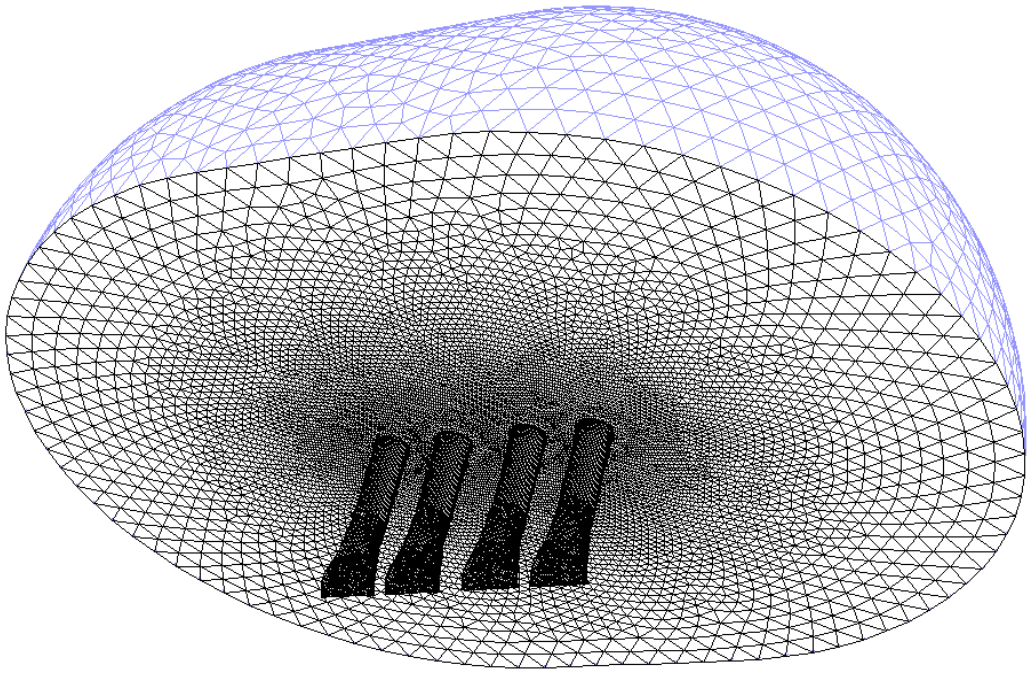

Figure 3-12: Overall grid of four intakes without airbox

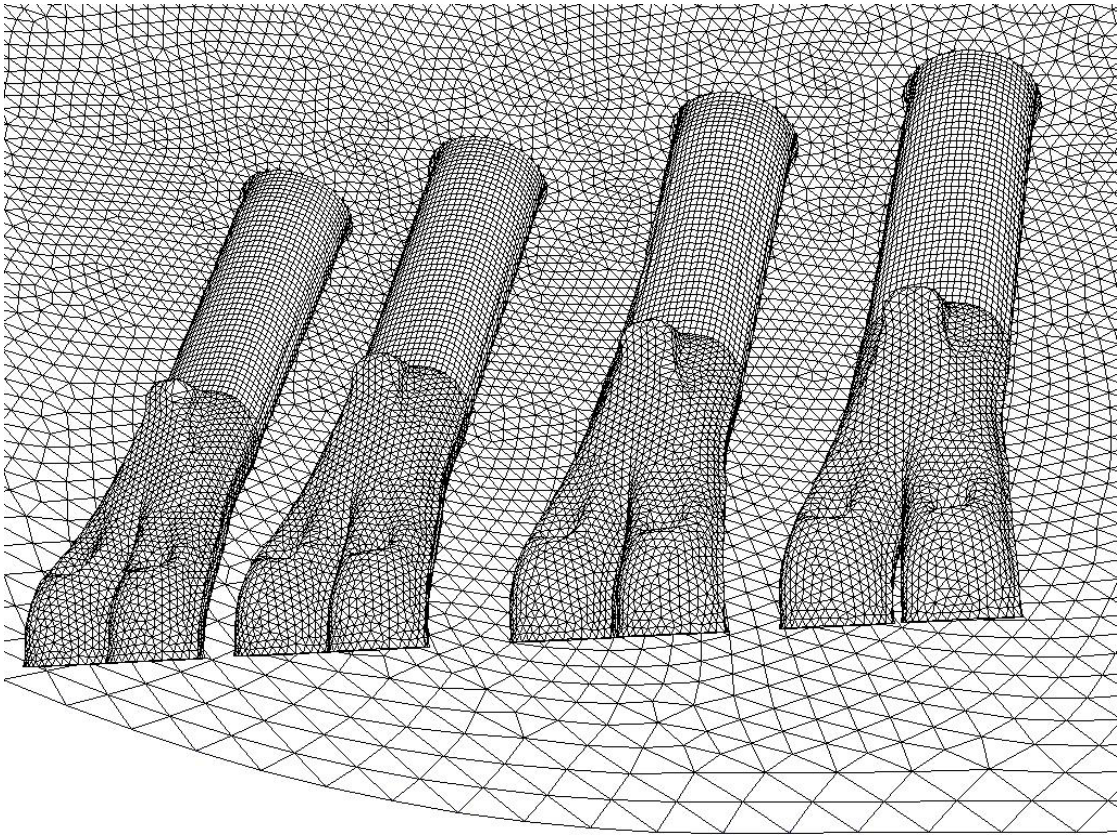

Figure 3-13: Close-up view of the mesh of the four intakes

3-3.3 Boundary Conditions

As in the single intake simulation, two pressure boundaries were specified at the inlet and outlet of the intake respectively. The steady-state solution is obtained before the unsteady flow is computed. For the full simulation, the outlet boundary at each of the ports is changed to a varying pressure boundary during the respective valve-open period. Thereafter, the boundary is switched to a wall in order to represent the valve-closed cycle. This boundary change is performed in a sequence corresponding to the firing order.

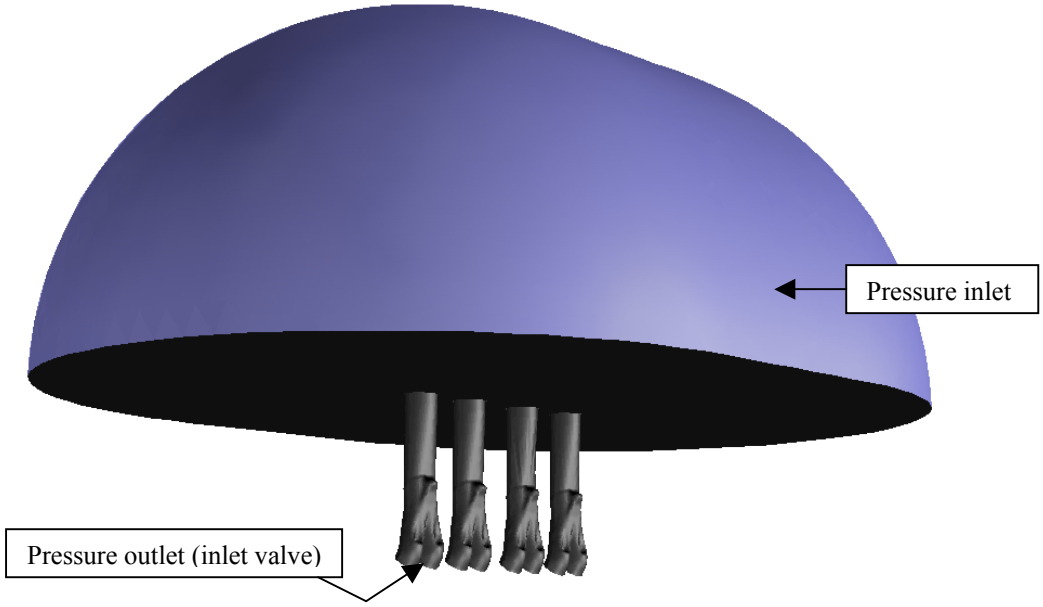

Figure 3-14: Boundary location

3-3.4 Transient Modelling

The modelling approach described in section 3-1.2 was followed for this simulation. The valve timing data of the engine are summarised in Table 3-2.

Table 3-2: Valve timing data

		Total time
Valve open	0 – 0.0071632s	0.007213 s
Valve close	0.0071632 – 0.01841327s	0.01125007 s
Engine cycle time		**0.01841327 s**

It was necessary to obtain the valve timing data of the engine because of the need to correctly simulate the full engine cycle as close to reality as possible. The implementation of the valve timing into the simulation is described in detail in the section that follows.

3.3.4.1 Engine firing sequence in FLUENT

For the full-engine simulation, the correct engine firing order must be carefully implemented in the CFD solution process. This is achieved in FLUENT by changing the pressure outlet boundary at each of the inlet ports to a varying pressure boundary during which the EngMod4T pressure data are enforced for the valve-open period. Thereafter, the boundary is switched to a wall in order to represent the valve-closed cycle. The pressure at the inlet valve during the valve-closed period is dependent on the FLUENT computations. The whole process of boundary changing and specification is automated by the use of FLUENT's scripting capability (journal file). This journal file contains text commands that are read by FLUENT for execution at user-specified intervals.

3-3.5 Results and Discussion

The mass flow rate into each intake is shown in Figure 3-15. It can clearly be seen that the ingested mass of air into each intake is not equal. The total mass of air inducted in each cycle obtained from the simulation is 2.619 g. This resultant inducted mass is 4.8% less than that obtained from four times of that of the single intake simulation in the previous section. This, along with Figure 3-15, confirms that indeed the assumption (from the previous section) made that the four intakes ingest the same amount of air is flawed.

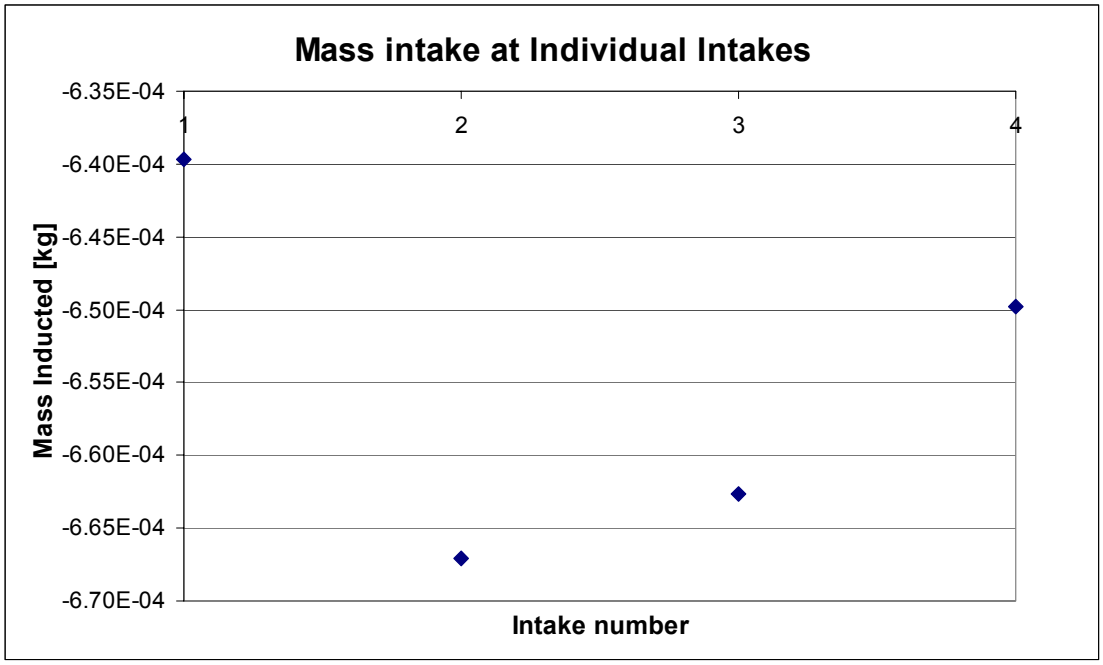

Figure 3-15: Mass of air inducted by individual intakes

The atmospheric boundary condition (pressure inlet boundary) reflects pressure waves travelling towards it (at the trumpet mouth). It is for this reason that the airbox is to be explored to determine its influence on the resultant mass inducted.

3-3.6 Conclusion

The section considered four intakes, open to atmosphere, for analysis. The results showed that more detail needs to be included in order to more accurately assess the performance of the intake system. The airbox with its one inlet and asymmetrical flow qualities was thus added as discussed in the next section.

3.4 FOUR INTAKES WITH AIRBOX (BASE CASE)

The final implementation of the study, as far as the geometry is concerned, is the addition of an airbox as part of the simulations to follow. The airbox geometry was also obtained from Toyota Motorsport and forms a major component of the parametric study. The original airbox (hereinafter referred to as the *base case/geometry*) can be seen in Figure 3-16. To reduce meshing difficulties, some detail in the geometry as seen in the figure was either removed or simplified in those areas considered to have little impact on the flow. More pictures of the complete inlet system, though not modelled, can be seen in Appendix A. The problem setup is similar to the case without the airbox (previous section).

Figure 3-16: Original airbox geometry

The results obtained from this base case form the basis for comparison in the optimisation study. It therefore is important that the predicted flow is accurate as far as the CFD simulation is concerned.

3-4.1 Grid Generation and Boundary conditions

In order to closely represent the intake port, simplified valve stems were added since they reduce the flow area at the outlet and also offer increased flow resistance, which could impact on the mass flow rate.

The mesh, containing around 400 000 elements, was generated in FLUENT's pre-processor GAMBIT [26] (see an example of the Gambit journal file in Appendix D). The overall grid of the geometry can be seen in Figure 3-17. Note how the grid cells are concentrated around the intake and the port geometry; this is mainly due to interesting flow features that are expected to occur and a refined mesh in these areas increases the chance of capturing these features.

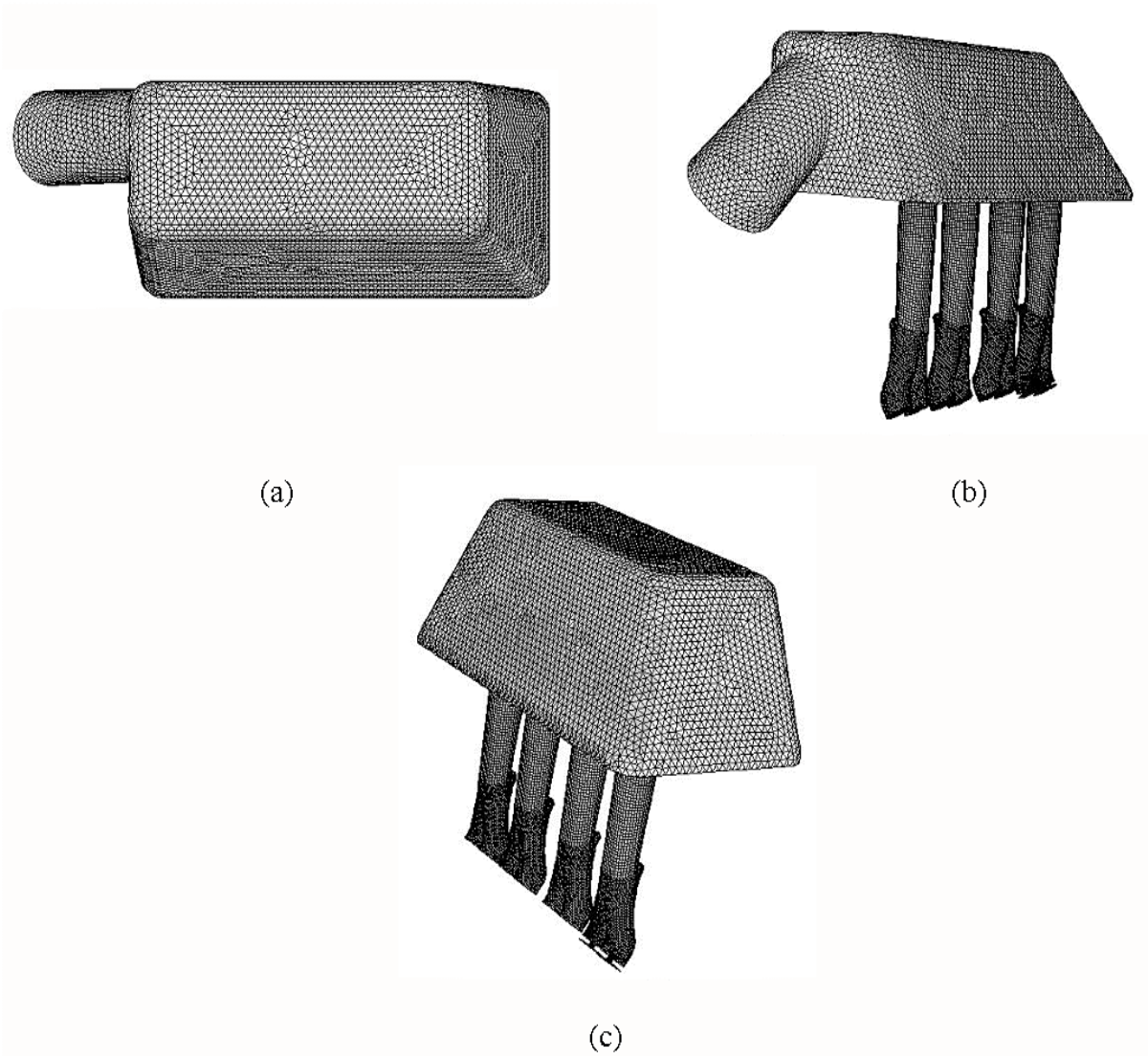

Figure 3-17: Views of overall grid

Two boundaries were specified at the inlet (pressure-inlet boundary in blue) and outlet (pressure-outlet boundary in red) of the intake as seen in Figure 3-18. The location of the inlet pressure boundary has some influence on the pressure inside the airbox and intakes. However, the pressure differences due to boundary location have a negligible effect on the power output of an engine as shown by Maynes *et al* [1]. This led to a decision to place the boundary at the airbox inlet.

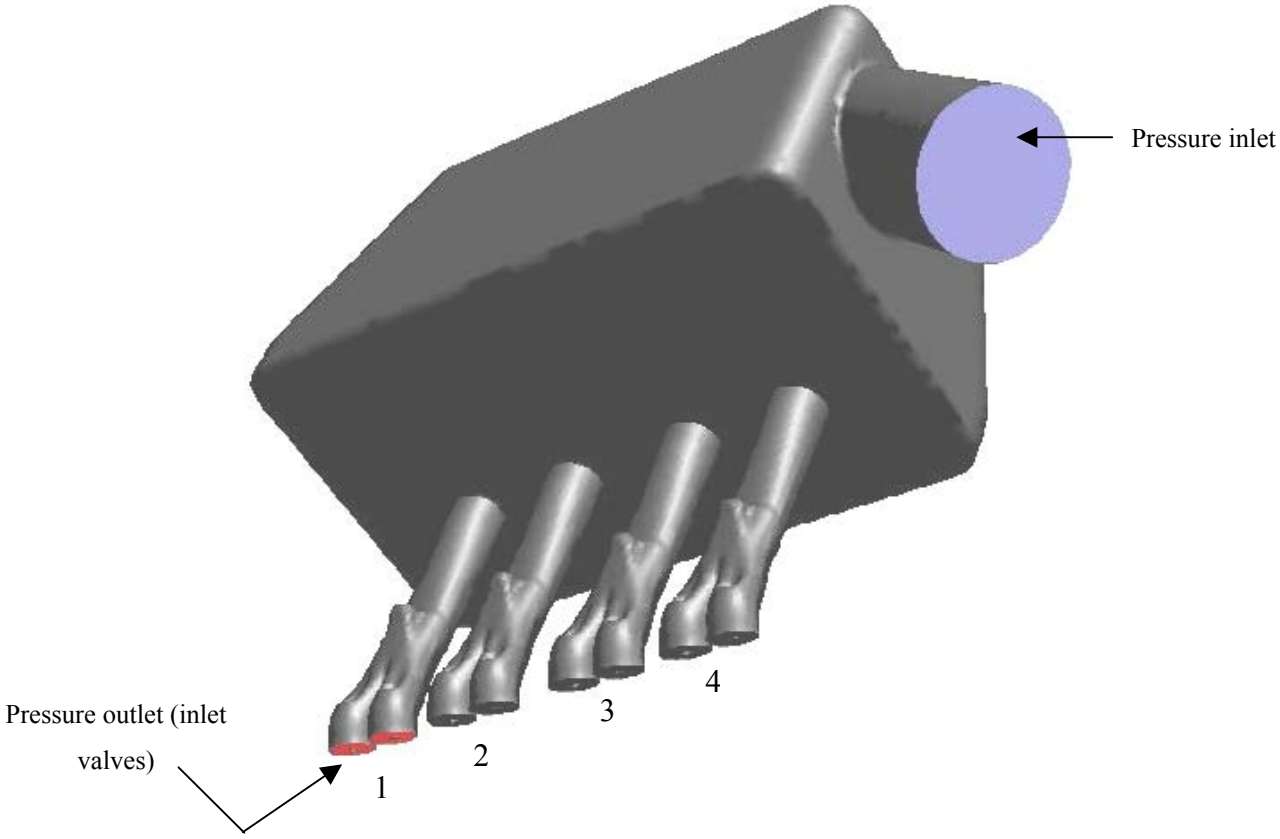

Figure 3-18: Rendered view showing boundary types by colour (intakes and airbox)

A pressure drop is specified for the initial steady-state CFD simulation. The purpose of the steady-state solution is to initialise the flow in the intake before the unsteady solution is computed, and to obtain the outflow temperature boundary condition for air density calculation. For the unsteady flow computation, the pressure outlet boundary is changed to a varying pressure boundary, with the pressure data from EngMod4T used as an input.

3-4.2 Steady-state modelling and experimental validation

3.4.2.1 Experimental validation

As per accepted engineering practice, where possible, experimental tests are performed to compare to simulation results so as to better judge the confidence level in the simulation results. This validation route was also taken in this study, although the experimental tests were limited to steady state since facilities to perform unsteady flow tests were not available. Nevertheless, the steady-state results give a very good idea of the accuracy of CFD simulations as will be shown by the results.

Experimental flow rate measurements were taken on a flowbench (SuperFlow-110 [42]), at a constant pressure drop of 1993.7 Pa (8 inch manometer reading), for various valve lifts, as well as the case where the valves were removed completely to allow for maximum flow. The experimental set-up can be seen in Figure 3-19, and more detailed illustrations are presented in Appendix C, Figure C-1 to Figure C-4. The valve lift measurements were taken at increments of 0.5 mm from 0 to 12mm valve opening. Note, however, that for the transient simulations that follow, only the no-valve case is used.

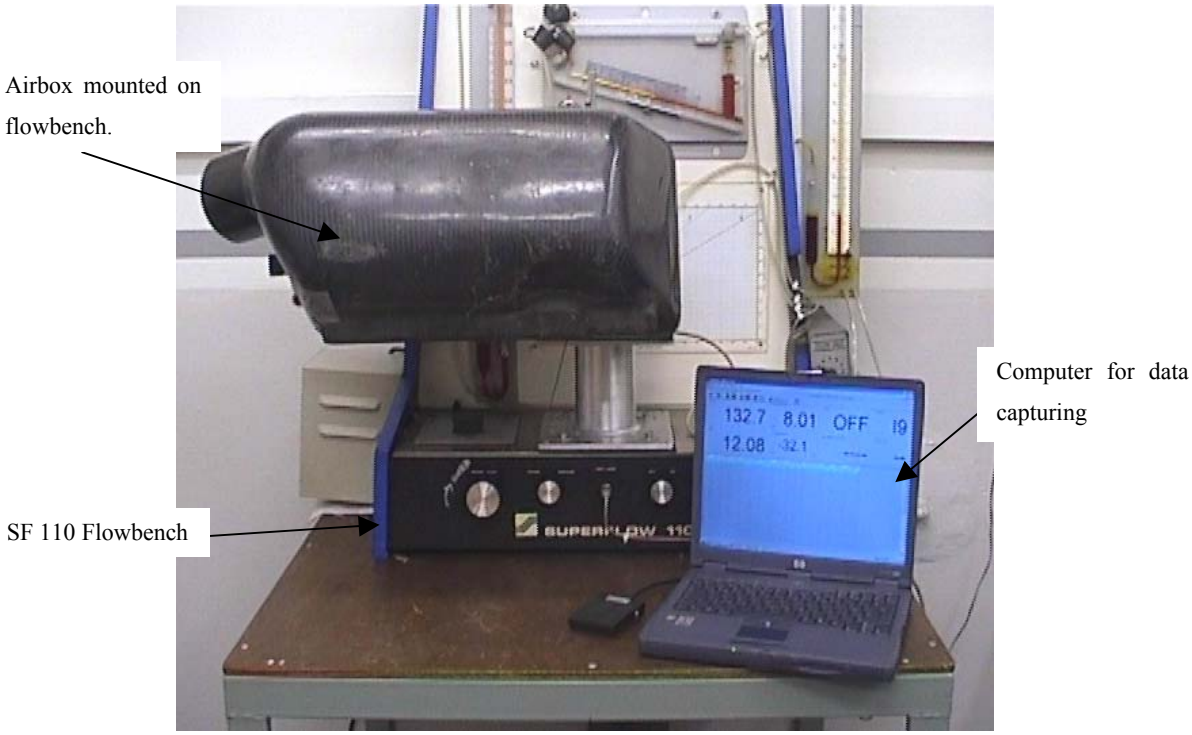

Figure 3-19: Flowbench experimental set-up

CFD simulations of the experimental set-up were performed for comparison purposes at four valve lift points (3, 6, 9 and 12 mm) were selected. The CFD model in Figure 3-18 was modified by the addition of simplified valves, at specified lifts, as shown in Figure 3-20. Also shown in the figure is the location of the pressure outlet boundary as an annular ring.

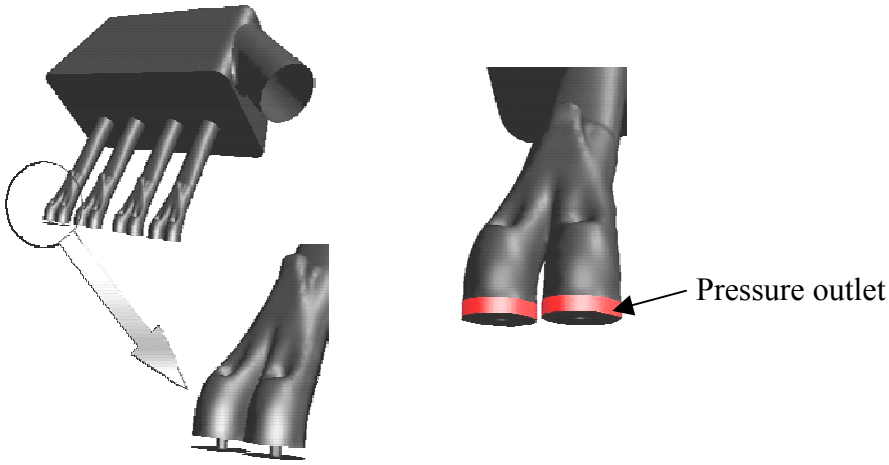

Figure 3-20: Full geometry with simplified valves added and valve-lift pressure boundary specification

Figure 3-21 shows the added mesh volume (in red) to accommodate the valve lift geometry. The added volume is one made up of structured elements thus not increasing the total cell count by much.

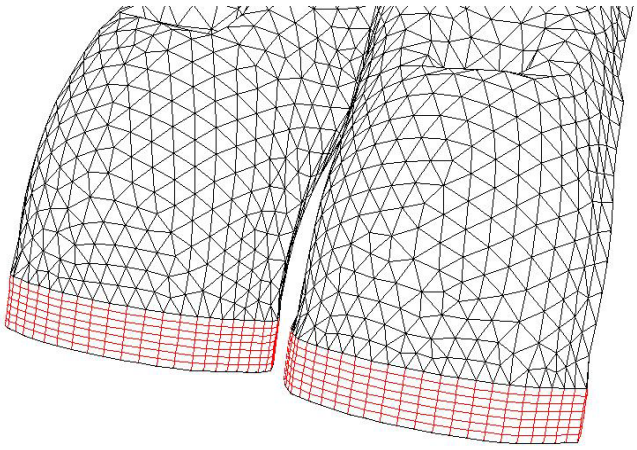

Figure 3-21: Mesh extension for valve lift simulations

3.4.2.2 Results of validation

The CFD and flow bench test results show satisfactory agreement as depicted in Figure 3-22. For comparison purposes only, the no-valve geometry results are plotted at a "valve-lift" point of 13 mm.

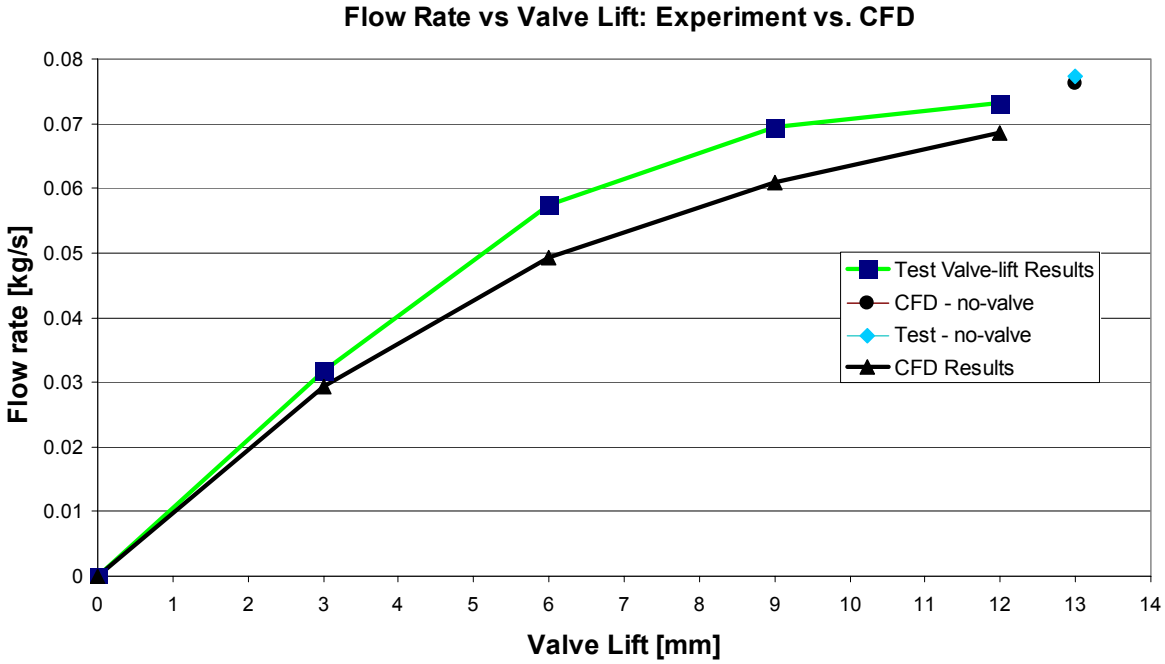

Figure 3-22: Comparison of CFD and flowbench results

The results for the valve lift cases differed by a maximum of 14.1% at a valve lift of 6mm and a minimum of 6.4% at 12mm valve lift. However, the results of the no-valve case differed by only 1.6%, which is in excellent agreement. The deviation in the valve lift cases can be attributed to the simplified valve, boundary placement as well as the "missing" cylinder volume.

3-4.3 Transient Modelling

The FLUENT journal file for setting and running the transient case is listed in Appendix D. It can be seen in Figure 3-23 that the pressure during the valve-closed period as calculated by EngMod4T differs only from the CFD by the amplitude of the waves. Even though the two simulation packages yield very similar results, there is information such as flow patterns that only FLUENT can provide because it solves the 3-D Navier-Stokes equations and also determines flow losses due to geometry that

are not predicted in EngMod4T. The principal losses in the intake are due to the friction at the walls and also the fluid interactions such as swirling, vortices, etc.

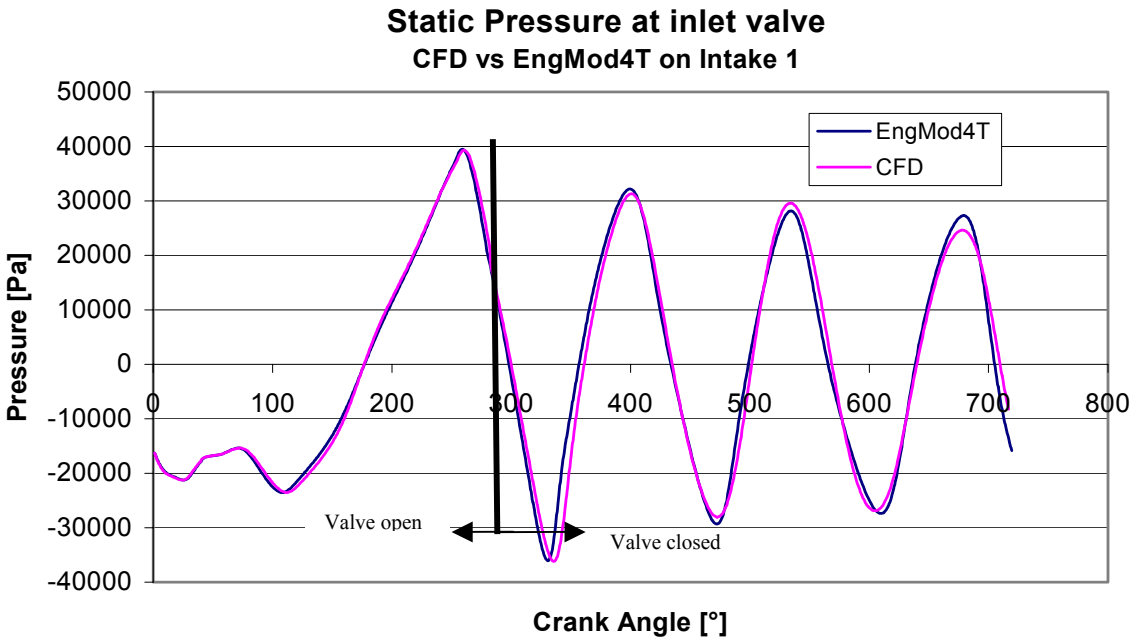

Figure 3-23: Comparison of CFD and EngMod4T average static pressure prediction at the inlet valve

The result of the deviation between the two results in Figure 3-23 is that the CFD result is not fully cyclic within the 720° crank angle range because of the enforced varying pressure boundary. The only way to remedy this would be to couple the CFD and EngMod4T simulations continuously, or to replace the EngMod4T-generated pressure boundary condition in FLUENT with a more accurate prediction of valve motion and combustion in the cylinder (which is outside the scope of this study).

Figure 3-24 depicts contours of static pressure at different flow times. The different shades on the walls indicate the strength of the pressure pulse, which determine the amount of flow inducted in the system. In Figure 3-24 (a), the inlet valves for cylinder number two are open as witnessed by the light shade at the inlet port mouth. By observing time progression of the pressure contours, much information can be extracted and used for flow quality improvement. Also, areas of pressure pulse interaction become visible thus giving insight into the flow.

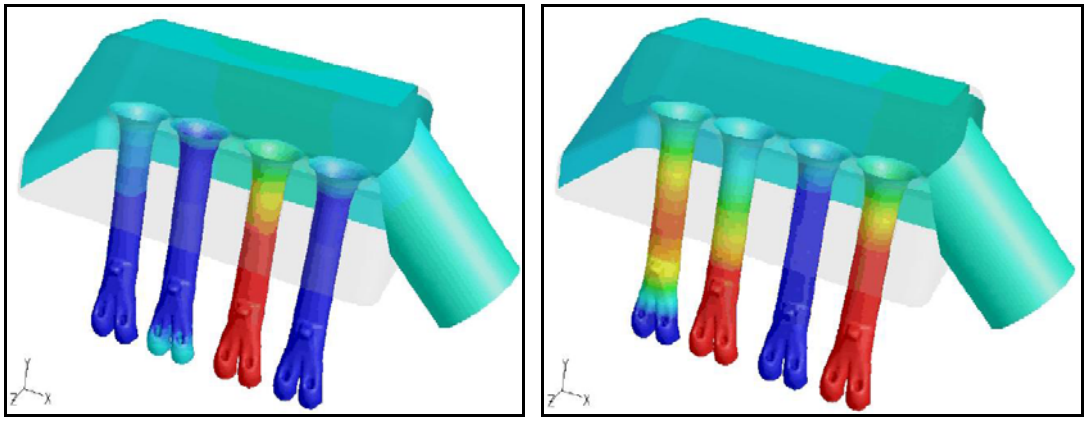

(a) (b)

Figure 3-24: Pressure contours on walls at different flow times

As the flow enters the airbox, it is directed to the top, as seen in the path lines Figure 3-25, where some loss of kinetic energy occurs because of the collision with the roof of the airbox. Although some energy has been lost, most particles stay attached to the airbox walls and eventually get drawn into the intake, maintained by the suction pressure at the inlet valves. Particles can be seen moving from the lower end of the airbox and around the trumpet indicating some loss in energy translating to lower mass flow at the intake. Also shown Figure 3-25, is a close-up view of the path lines in the inlet port.

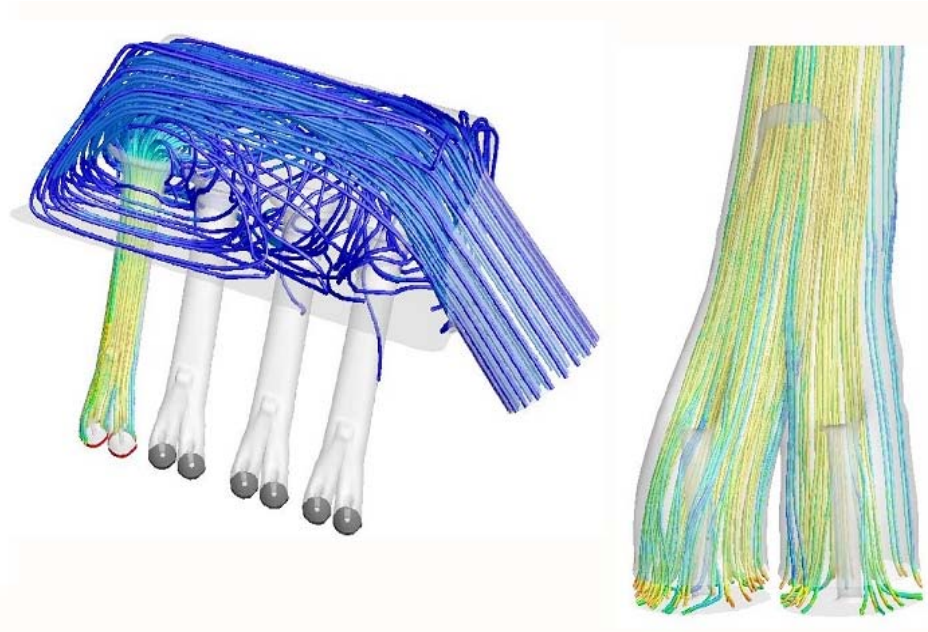

Figure 3-25: Instantaneous velocity path lines in airbox and inlet port (Intake 1)

Figure 3-26 depicts the predicted mass flow rate in intake number one. The mass flow rate profile is similar for the other three intakes. The effect of the reverse flow (around 250° crank angle) is minimal because the integrated area under the graph above the zero mass flow rate axis is relatively small compared to area below the axis. The integrated area below the axis indicates the amount of mass flow inducted over the crank angle range. Although this mass flow rate is mostly determined by the enforced transient pressure boundary at the inlet valve, factors such as frictional losses due to geometry, pressure pulses travelling through the airbox and cylinder-to-cylinder charge robbing also contribute to the total mass flow rate.

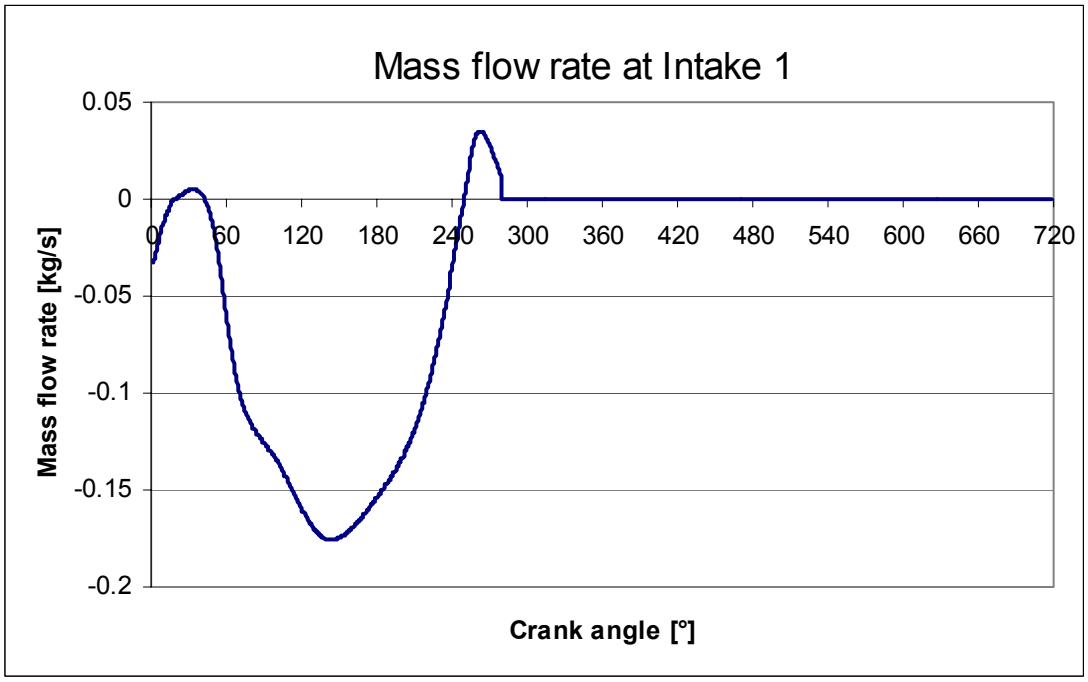

Figure 3-26: Mass flow rate at the inlet valve from the CFD simulation

Shown in Figure 3-27 is the amount of air that each intake inducts over one engine cycle. The distribution of inducted air is not equal, with more air inducted by the two middle intakes (Intakes 2 and 3). Note the negative axis used for mass inducted. The variation is mostly due to the airbox shape and design.

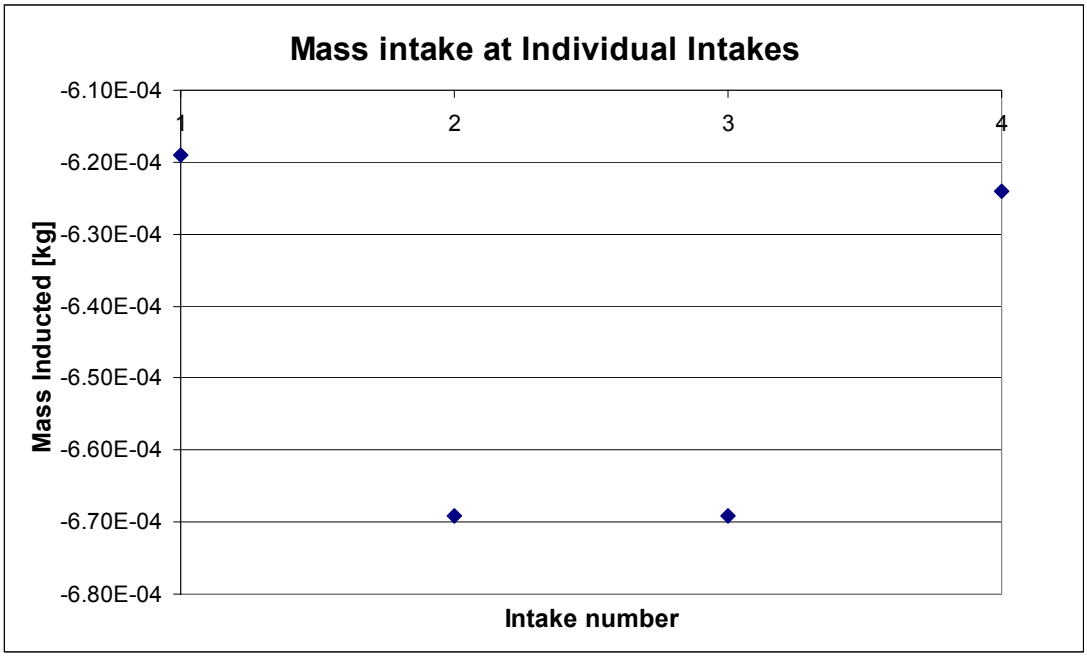

Figure 3-27: Mass of air inducted at individual intakes over one engine cycle

Figure 3-28 shows the normalised shear stresses on the trumpet and airbox surfaces over a full engine cycle (normalised to the average value over the engine cycle). Also plotted in the figure are the y+ values (refer to section 2-2.7) on all intake inner surfaces. It can immediately be seen that the contribution of wall shear stress in the airbox to losses is less than that of the trumpet walls. This is expected as the highest velocities occur in the intake. Also shown on the figure are the points where different intakes open during operation (boxed numbers). The trumpet wall shear stresses show little change when valve opening occurs. On the contrary, the y+ values are strongly influenced by the valve opening and closing sequences.

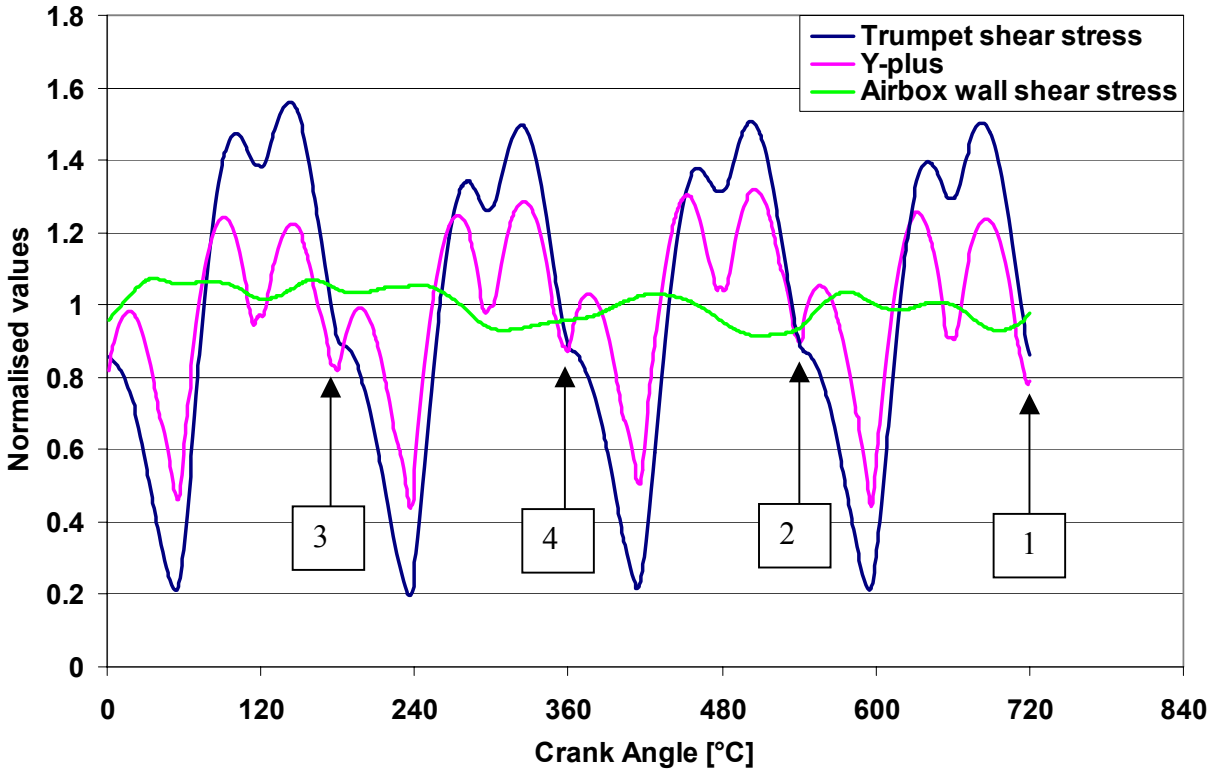

Figure 3-28: Shear stress and Y-plus plot for base case geometry

The oscillations in Figure 3-28 of y+ are similar to that of the trumpet shear stresses, except at intake opening points where the y+ values increase before again following the shear stresses' oscillatory trend. These oscillations can be attributed to the pulsating nature of the intake in a four-stroke internal combustion engine.

Adding to the solution confidence, are the actual area-weighted Y-plus values (not normalised as in Figure 3-28) obtained through the engine cycle as shown in Figure 3-29.

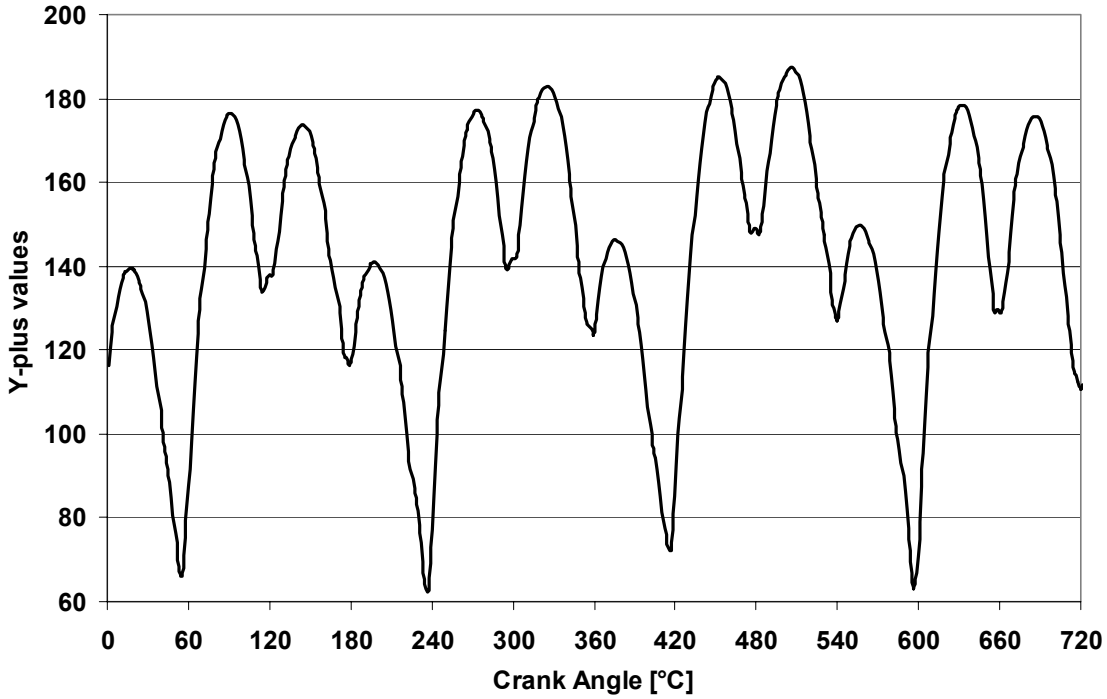

Figure 3-29:Y-plus values on intake inner walls

The values in Figure 3-29 range from just above 60 to below 200, which falls within the acceptable y+ range for flow where heat transfer is not of critical importance as is the case in this simulation.

3-4.4 Conclusion

The modelling and experimental validation of all four intakes with the airbox included were presented in this section. The CFD and experimental results showed good agreement and gave enough confidence to proceed with the optimisation study.

CHAPTER 4 : Intake Optimisation

4.1 INTRODUCTION

Since the base case results showed that an improvement could be achieved by reducing the amount of reverse flow, various airboxes were used in an attempt to maximize the mass flow rate. These airbox designs were obtained, not by trial and error, but through the use of the optimisation software LS-OPT (refer to section 2.3). The process involves selecting geometrical design variables and then varying them, mathematically, to obtain geometrical different airboxes and solving for a full engine cycle and obtaining the total mass flow. The total mass flow is then used as the objective function that needs to be maximised. The results in this section were presented at SACAM 2004 [43].

4.2 AIRBOX OPTIMISATION

4-2.1 Candidate design variables and objective functions

4.2.1.1 Candidate design variables

Candidate design variables are possible variables that could be used in the optimisation process and are initially considered before the final variables are selected. The selection criterion is primarily based on the impact a design variable might have on the objective function, but other factors such as ease of manufacturing or even aesthetics are considered. Considered design variables are shown in Figure 4-1.

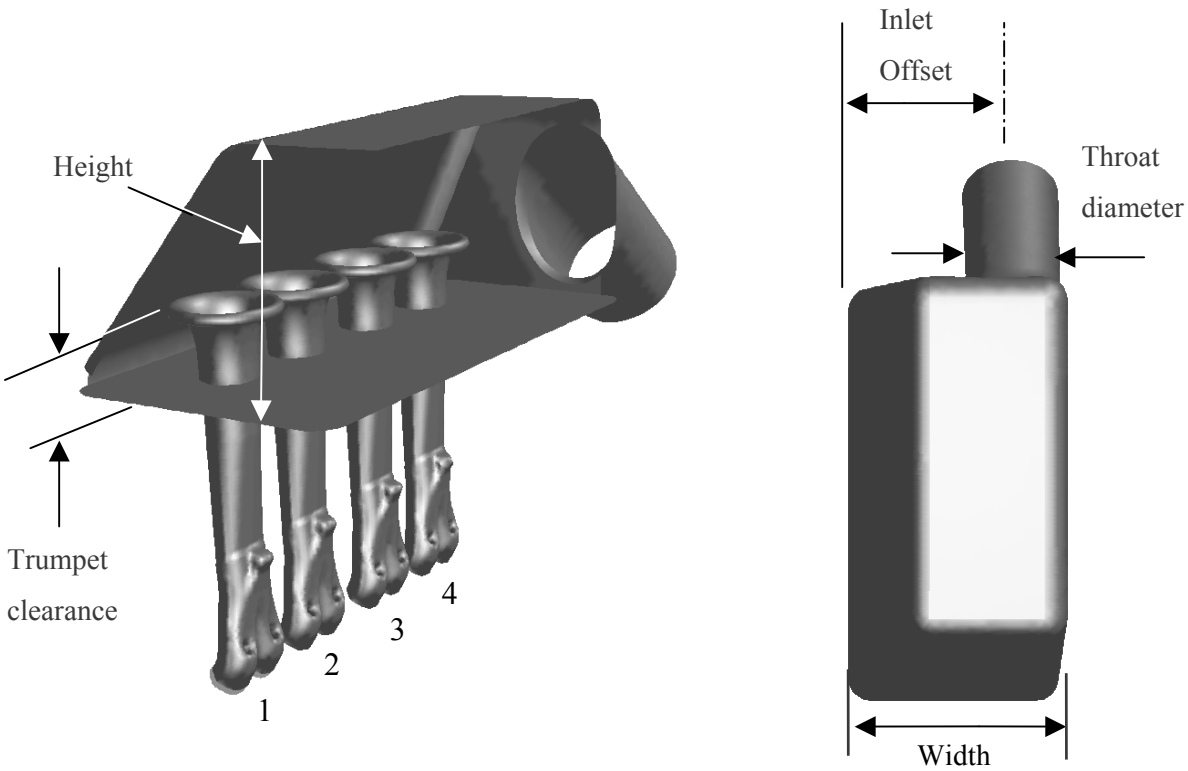

Figure 4-1: Intake-airbox arrangement with variables

Below are candidate design variables that were considered:

- Height on side of intake 1 (height at inlet pipe side remains constant to accommodate pipe)
- Width
- Trumpet clearance
- Throat diameter

- Offset
- Engine speed (RPM)
- Trumpet length/height
- Engine parameters such as valve seat angles, valve sizes, etc.

Due to the CFD computational expense, not all of the above variables could be included in the optimisation study, especially investigation of airbox performance at different engine speeds. Some variables, e.g., engine parameters and trumpet geometry, were eliminated because of the race rules prohibiting any changes on them. Nevertheless a sensitivity study on the influence of trumpet height was conducted using EngMod4T and the results are shown in Figure B-2 (Appendix B), showing that this variable is important in the performance of the engine. The throat diameter was excluded because of the manufacturing complexity. The inlet offset was excluded because of the geometrical modifications that would be required on the rest of the system to accommodate the offset inlet.

4.2.1.2 Candidate objective functions

The following objective functions were also considered in the optimisation:

- Total mass of air inducted every cycle
- Mass of air inducted by *each* intake every cycle

The latter was considered because the amount of inducted air by each intake during an engine cycle is not equal owing mainly to the airbox inlet not being positioned to evenly distribute the flow. Due to the immense computational effort required to simultaneously evaluate these objective functions in the optimisation study only the total mass inducted was considered as the primary objective, while the individual mass inductions were monitored.

4.2.1.3 Computational considerations

As discussed in section 2.3, the number of experimental points to be simulated is determined by the following relation, $\text{int}1.5[(N+1)]+1$, where N is the number of variables. In this case, assuming only one engine parameter is considered, if all design

variables (i.e., $N = 8$) are considered then 14 experimental points would be simulated for each iteration. The available computing capacity would not give satisfactory turnaround times considering a single CFD simulation would take, conservatively, around 120 hrs (5 days) to evaluate on a Pentium 4, 2.4 GHz with 512 Mb RAM. Therefore for one optimisation iteration, a total of 1680 hrs (70 days) would be required.

It must also be noted that the convergence to an optimum solution often takes more than two iterations, hence only three design variables (Airbox width, trumpet clearance and airbox height) were chosen. This translates to seven (7) experimental points requiring 840 hrs (35 days) to evaluate, which was deemed acceptable for the study.

4-2.2 Mathematical formulation

Since use is made of mathematical optimisation techniques, it is required that the problem be formulated in formal mathematical terms. The formulation is given below where the objective function $F(\boldsymbol{x}) = -f(\boldsymbol{x})$ is to be minimised. The function $f(\boldsymbol{x})$ is the amount of airflow inducted into the engine, which is negative in nature hence, the use of $F(\boldsymbol{x})$.

Minimise $F(\boldsymbol{x})$ (4.1)

Subject to the bounds in Table 4-1,

Table 4-1: Bounds for optimisation problem

Variable name	Design variable	Min [mm]	Max [mm]
Height	x_1	100	210
Trumpet clearance	x_2	60	90
Width	x_3	0	100

and the constraint to avoid physical interference of the airbox roof with the trumpet mouths (given in mm):

$$g_1 = 50 + x_2 - x_1 \leq 0 . \quad (4.2)$$

4-2.3 Results

The mass flow rate is integrated to give the total inducted mass during an engine cycle using the trapezoidal method of integration. The results are given in Figure 4-2 for the 7 experimental points of each iteration, and they clearly show that the geometry has an influence on the mass inducted into the engine. An improvement of 6.2% can be seen at experimental point 3 of the second iteration (Iter-2). Noting that engine performance is directly proportional to mass ingested, an increase of 6.2% in engine power is expected. The optimisation process was judged to have reached a satisfactory solution after Iteration 2 since the results yielded little variance for the simulated experimental points.

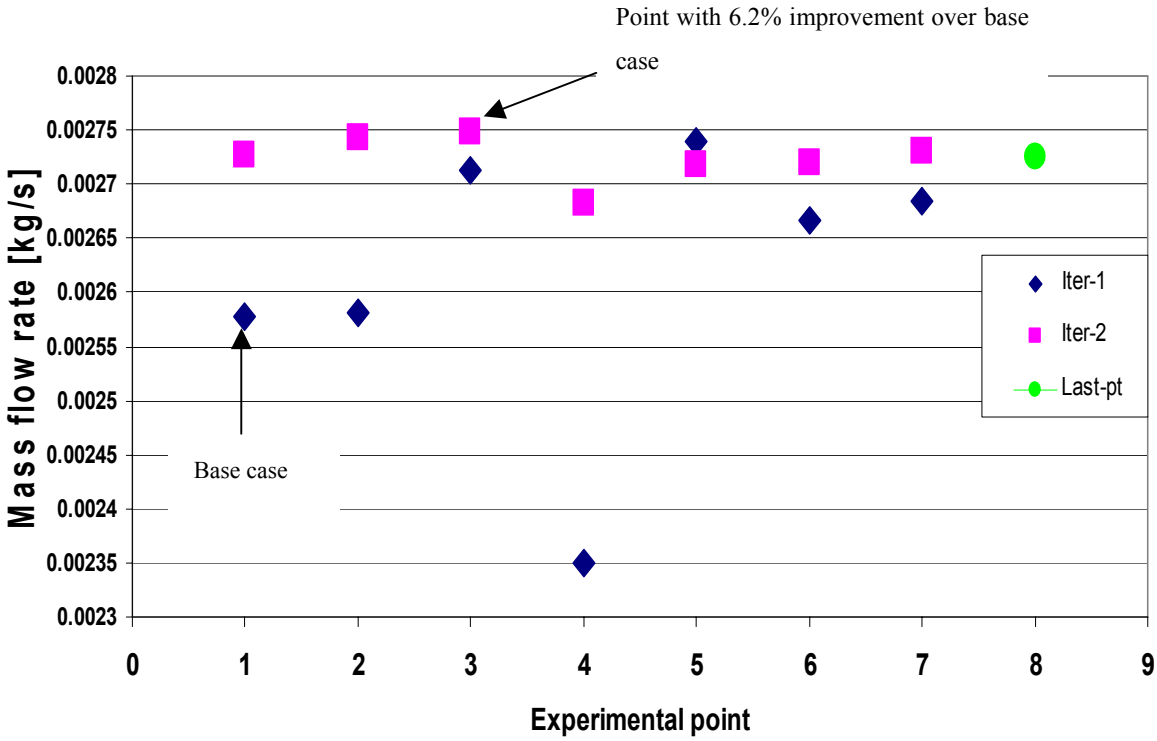

Figure 4-2: Results of airbox optimisation study

The final (improved) airbox parameter values, along with those of the base case, are listed in Table 4-2. Also listed are the results for total mass of air inducted for the two designs. (See breakdown of individual intakes in Figure E-2, Appendix E).

Table 4-2: Parameter values and mass flow rate results of airbox optimisation

	Base Case	Improved design
Height [mm]	210	155
Trumpet clearance [mm]	90	84
Width [mm]	240	340
Total mass inducted [g]	**2.578**	**2.748**

The original airbox along with the improved airbox is shown in Figure 4-3. The improved airbox is wider and also has lower end-height (at intake 1). The trumpet clearance did not change much from the original one and seems to not be as influential as the other variables.

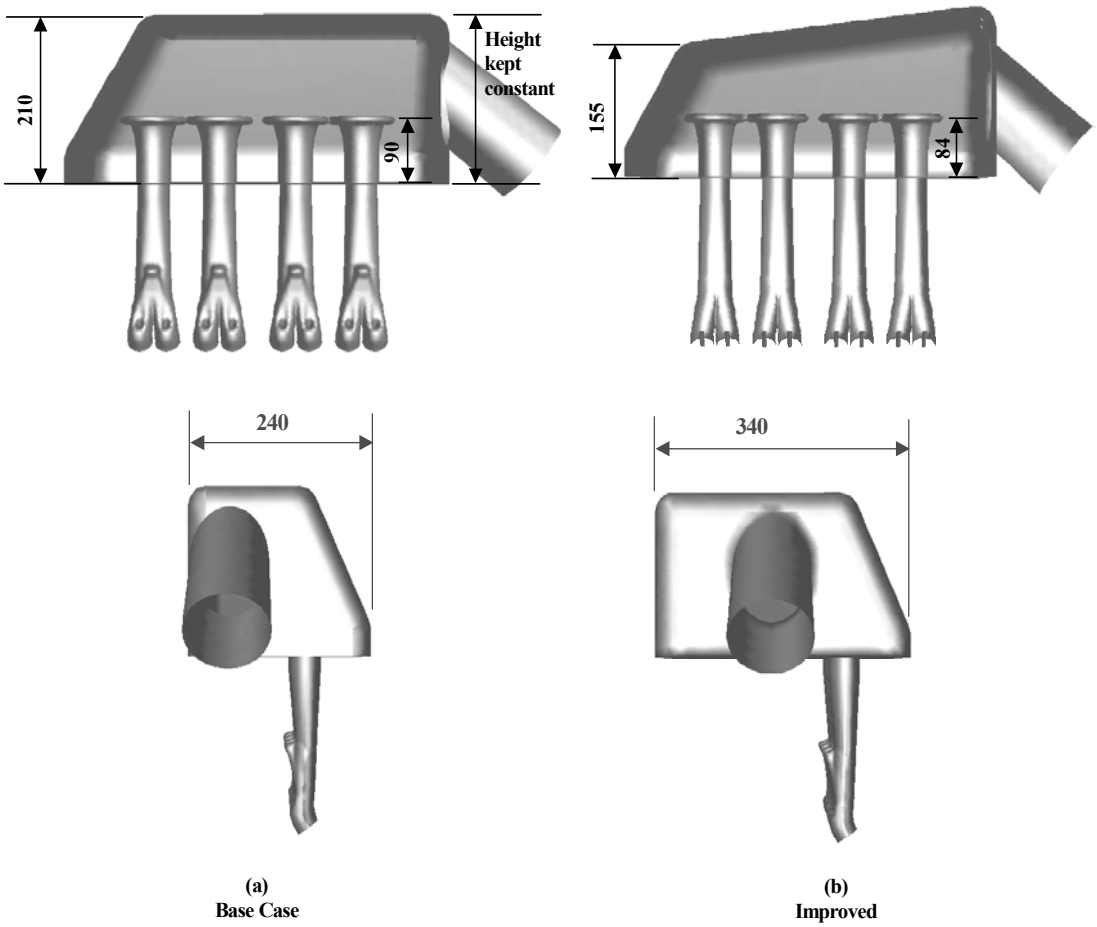

Figure 4-3: Illustration of the base and optimum airbox designs [mm]

The design variable values are plotted in Figure 4-4 and Figure 4-5 for the two optimisation iterations. These figures show all the designs that were explored before the improved design was achieved. The width values are plotted relative to the starting width (i.e. 240 mm).

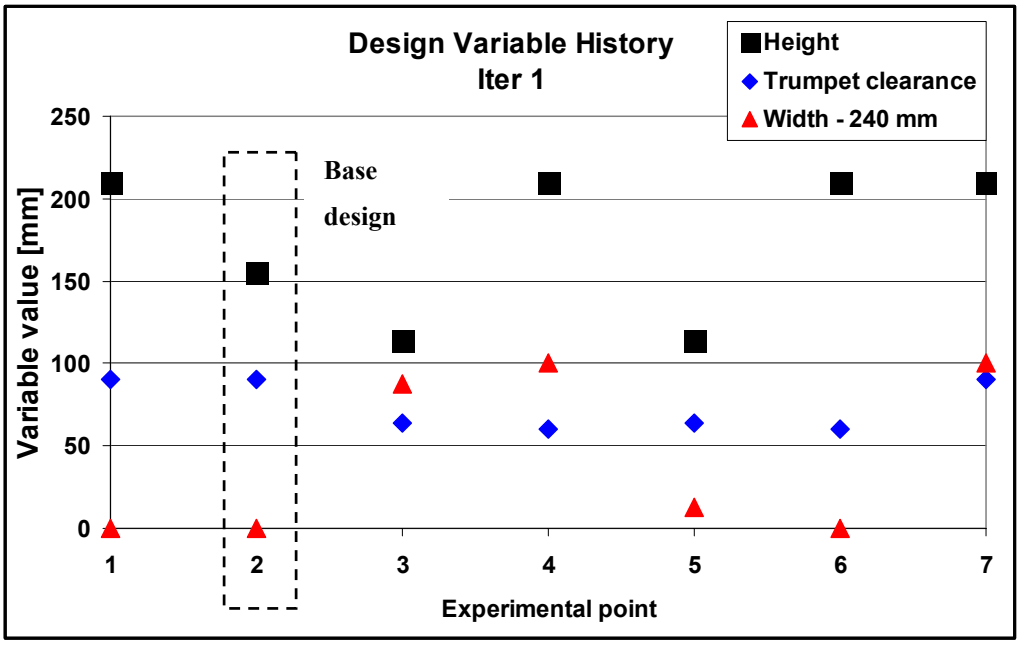

Figure 4-4: Design variables for first iteration

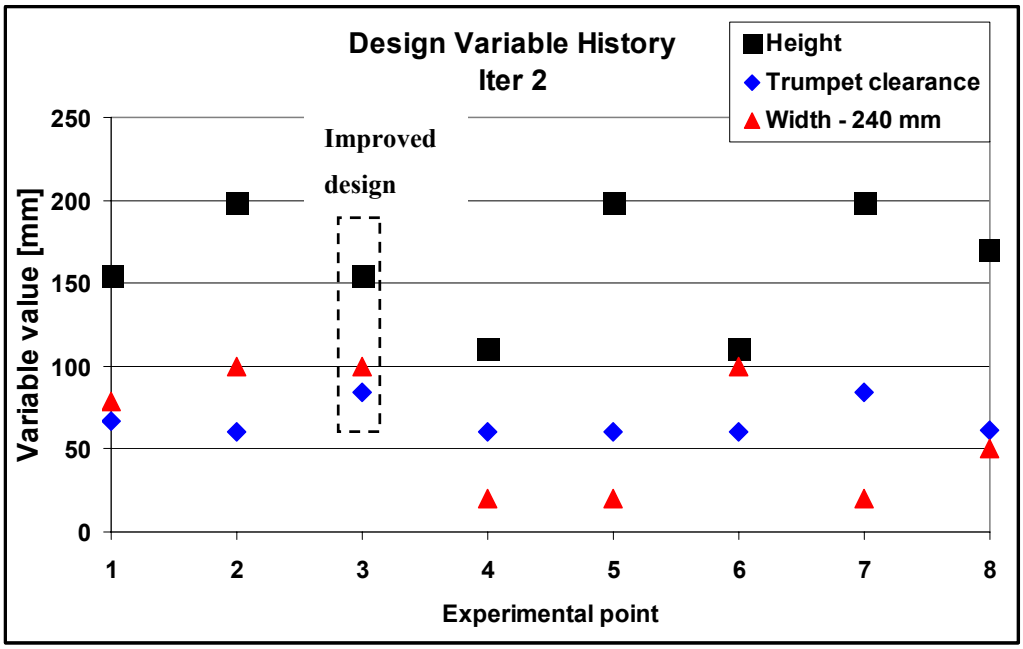

Figure 4-5: Design variables for second iteration with last point simulated included (point 8)

Note that in Figure 4-5 (and Figure 4-2), there are eight experimental points. Experimental point 8 does not form part of the second iteration but was added for comparison purposes. This point is the last point given by LS-OPT as a conclusion of the optimisation. As LS-OPT uses response surfaces, this point is the best design predicted from the surface obtained in iteration 2. The value in Figure 4-3 (green – last point) is the simulated result corresponding to the design variables of the prediction.

Although not clearly visible, the figures show that the design space has been reduced by small margin. Consider the design space in the figures. In iteration 1 (Figure 4-4), the range is from 0 to 210 mm but this range is reduced to 20 to 200 mm in iteration 2 (Figure 4-5). This indicates that the design space for this particular variable has been reduced as the optimisation converges by the SRSM algorithm in LS-OPT. The same region reduction process applies to the remaining two variables. This analysis of the design history shows the practical application of the optimisation methodology discussed in section 2-3.3.

4-2.4 Off-design performance

4.2.4.1 Problem layout

Since the airbox was optimised for a single engine speed of 6500 rpm, the performance at other speeds may be affected, hence simulations using the improved design were done at two other engine speeds to determine the mass flow rate. The base case was also simulated at these engine speeds, which were chosen to be 5500 rpm and 7500 rpm.

4.2.4.2 Results and Discussion

EngMod4T was used to simulate the inlet boundary pressure at these engine speeds for use in the CFD simulations, as shown in Figure 4-6. The 5500 rpm and 7500 rpm pressure plots have a significant area above the zero pressure axis when compared to the 6500 rpm plot. This indicates that reverse flow might have a significant influence on the mass flow results.

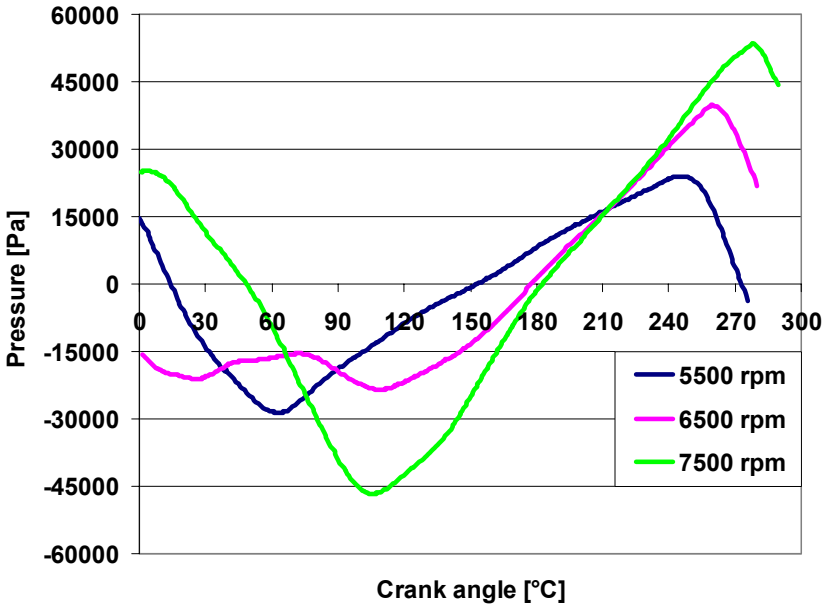

Figure 4-6: Simulated pressure for different engine speeds

The mass flow rate results for the base and improved airbox simulations are presented in Figure 4-7 (See also a breakdown of the individual intakes in Appendix E). The designs have very similar performance at the 5500 rpm point, while at the improved airbox also performs better than the base airbox at both 6500 rpm and 7500 rpm.

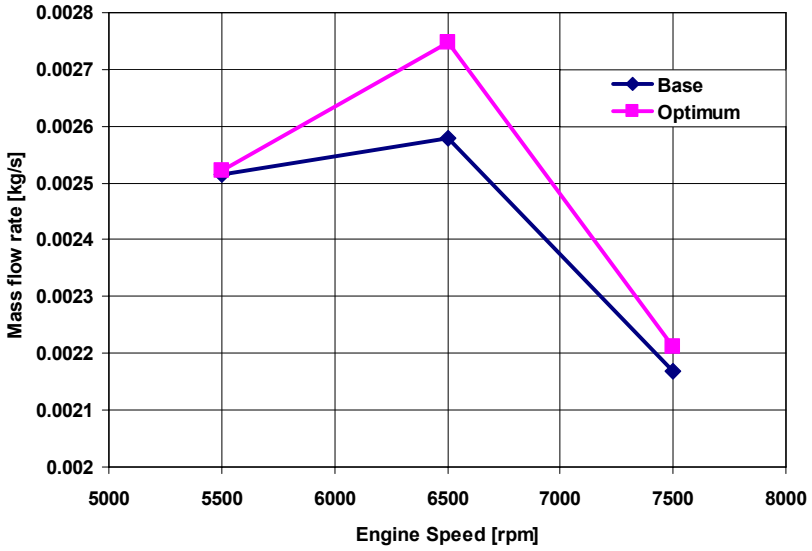

Figure 4-7: Mass flow rate response of base and improved airboxes at different engine speeds

Although the airbox was optimised only for the 6500 rpm engine speed, it is by sheer co-incidence that the improved design also outperforms the original airbox at the off-design points. Although each engine speed might have a different optimum airbox, the improvement gained shown by the improved airbox design (i.e., improved design at 6500 rpm) at the off-design points is sufficient.

4-2.5 Conclusion

In this section, results of the optimisation of the airbox were presented. By combining CFD with mathematical optimisation, an improvement on the original airbox performance was achieved by only changing the geometry of the airbox. Off-design performance of the improved design airbox was also assessed and an overall improvement over the original airbox was found.

CHAPTER 5 : Conclusions and Recommendations

5.1 CONCLUSIONS

The literature survey conducted in CHAPTER 2 highlighted the importance of proper engine intake system design in order to achieve different engine characteristics (e.g., economy and driveability for everyday driving vs. maximum volumetric efficiency with little regard for economy for racing purposes). With the amount of research already gone into various intake configurations and modelling techniques required to evaluate intake systems, the effort needed to set up the problem approach for this particular study was reduced immensely.

This study took the bottom-up approach to modelling the intake system of a high-performance rally engine as presented in CHAPTER 3. This meant firstly modelling a single intake, then all four intakes excluding the airbox and then including the airbox as a final step.

Firstly, a single intake was modelled with the assumption that the mass flow rate into all the four intakes was equal and the flow was symmetrical. The results from this simulation were mostly for insight purposes and since the model was simple to set up, it gave the opportunity to have a base starting point as the simulations and model progressively became more complex. Although important information was gathered from the simulation, the problem had been over-simplified and the model was thus extended to include all four intakes but without the airbox.

The results obtained from the four intakes simulation pointed to the importance of intake interaction and its influence on intake air mass flow. Features such as inter-intake robbing were observed, and this prompted the inclusion of the airbox, as this would affect pressure wave interactions with the inner airbox wall. The airbox as expected, did have an influence on the mass flow rate inducted into the cylinders by the intakes.

The final implementation of the study was optimisation of the existing airbox design for the chosen engine speed, as outlined in CHAPTER 4. The investigation required the selection of airbox geometrical parameters that would be varied, with the aid of optimisation methods, to change the airbox design and determining the total mass flow inducted during a full engine cycle. After two iterations, involving exploring fifteen designs, a final design giving an improvement of 6.2% was obtained.

5.2 RECOMMENDATIONS

As far as recommendations are concerned, an optimisation of the intake geometry could be performed where several objectives, such as mass flow into each intake or the intake performance at different engine speeds, are considered. With the ever-increasing computing capability, the number of design variables can be increased to allow more complex airbox and intake geometries. These variables may include the airbox inlet pipe throat diameter, radii of the edges, etc.

Also, experimental unsteady testing of the improved airbox is essential for proper completion of the study while at the same time validating the optimisation findings. This should be done at all engine speeds and finally, road-testing should be performed to evaluate the effect of the optimised design on the actually rally car engine response. This should be done under the same conditions for both airboxes in order to objectively judge the influence of the change.

A more appropriate approach to the problem is to dynamically link the gas dynamics boundary condition and the CFD solution. This requires extensive coding that would enable the two packages, namely EngMod4T and FLUENT, to exchange boundary information at each time-step during the unsteady computation. The computed CFD boundary information would be exported to the 1-D gas dynamics solver and new boundary data, i.e., pressure and temperature, would be computed and read back into the CFD solver for use in the next time-step.

This linking would provide increased accuracy as far as boundary data are concerned, and is done successfully with commercially available software such as Virtual 4-Stroke as discussed in [1]. By using CFD moving mesh capability and directly

modelling combustion, the study would do away with the need for a 1-D engine simulator. This however, is still not feasible with the current available computing capability.

The study, in spite of its shortcoming of uncoupled computation as discussed, showed that CFD and mathematical optimisation methods can be successfully married to arrive at an improved design much more efficiently than with the traditional trial-and-error method.

REFERENCES

[1] Maynes, BDJ, Kee, RJ, Kenny, RG, Fleck, R, Mackey, DO & Foley, L, (2002), 'Prediction of Formula 1 Engine and Airbox Performance using Coupled Virtual 4-Stroke and CFD Simulations', *SAE Paper 2002-01-3318. Proceedings of Motorsports Engineering Conference and Exhibition,* Indianapolis, USA.

[2] De Vita, A, Andreassi, L & Di Angelo, L (2001), 'Experimental and Computational Study for the Optimisation of Race Car Intake Air Flow', *SAE Paper 2001-01-1852*.

[3] De Vita, A, Di Angelo, L, Andreassi, L & Romagnuolo, S (2002), 'CFD-Aided Design of an Airbox for Race Cars', *SAE Paper 2002-01-2167, International Body Engineering Conference & Exhibition and Automotive & Transportation Technology Congress,* Paris, France.

[4] Heywood, JB (1992), *Internal Combustion Engine Fundamentals*. McGraw-Hill International, New York.

[5] Smith, PH & Morrison, JC (1968), *The Scientific Design of Exhaust and Intake Systems,* Second Edition, G. T. Foulis & co, LTD. London.

[6] Blair, PG (1999), *Design and Simulation of Four-stroke Engines,* Society of Automotive Engineers, Inc. Warrendale, Pa.

[7] Smith, LA, Fickenscher, T, & Osborne, RP (1999), 'Engine Breathing – Steady Speed Volumetric Efficiency and Its Validity Under Transient Engine Operation', *SAE Paper 1999-01-0212, International Congress & Exposition*, Detroit, MI, USA.

[8] *Variable Intake Manifold* (2002), Retrieved: February 19, 2002, from http://autozine.kyul.net/technical_school/engine/tech_engine_2.htm#Variable Intake Manifold

[9] Hatamura, K, Morishita, K, Asanomi, K & Shiraishi, H (1987), 'Mazda's New V-6 Gasoline Engine and its Innovative Induction System', *SAE Paper 871977*.

[10] Sakono, T, Takizawa, S, Harada, S, Ikeda, T & Abe, H (1992), 'Mazda's New Lightweight and Compact V-6 Engine', *SAE Paper 920677*.

[11] Winterbone, DE & Yoshitomi, M (1990), 'The Accuracy of Calculating Wave Action in Engine Intake Manifold', *SAE Paper 900677*.

[12] Winterbone, DE & Pearson, RJ (2000), *Theory of Engine Manifold Design – Wave action methods for IC engines,* Professional Engineering Publishing Limited, UK.

[13] Engström, J, Kaminski, CF, Aldén, M, Josefsson, G & Magnusson, I (1998), 'Experimental Investigations of Flow and Temperature Fields in an SI Engine and Comparison with Numerical Analysis', *SAE Paper 1999-01-3541*, *Proceedings of International Fuels & Lubricants Meeting & Exposition*, Toronto, Canada.

[14] Anderson, MK, Assanis, ND & Filipi, SZ (1998), 'First and Second Law Analyses of Naturally Aspirated, Miller Cycle, SI Engine with Late Intake Valve Closure', *SAE Paper 980889, Proceedings of the International Congress & Exposition,* Detroit, MI, USA.

[15] Jovanovic, Z & Petrovic, S (2000), 'The Effect of Intake Flow Modelling on Flame Front Shape and its Displacement in Cylindrical Combustion Chamber', *Proceedings of the Eleventh International Multidimensional Engine Modeling User's Group Meeting,* Detroit, MI, USA.

[16] Van Niekerk, CGJ (2002), *EngMod4T – A four-stroke engine simulation package.*

[17] Polášek, M & Vitek, O (2001), 'Combination of 0-D Simulation of an ICE with Advanced CFD Methods', *pp. 33 – 42, Proceedings of the 12th MotorSympo, International Symposium,* Brno, Czech Republic.

[18] Exa Corporation, PowerFLOW 3.0 (2001), Retrieved: January 25, 2001, http://www.exa.com/newsite/frames/powerflowmaster.html.

[19] Wirtz, R & Mazzoni, D (1998), 'Application of WAVE in Motorcycle Prototyping', *Proceedings of the Ricardo Software International User Conference*, Detroit, USA.

[20] Papaconstantis, C (2001) *Improvement of a V6 2.5l SI Engine's Performance through the use of an Inlet Manifold that utilises Air Resonance Charging,* BEng Undergraduate thesis, Department of Mechanical Engineering, University of Pretoria. South Africa.

[21] White, FM (1991), *Viscous Fluid Flow,* Second Edition, McGraw-Hill International, New York.

[22] White, FM (1994), *Fluid Mechanics,* Third Edition, McGraw-Hill International, New York.

[23] Tennekes, H & Lumley JL (1994), *A First Course in Turbulence,* The MIT Press. Massachusetts.

[24] Ferziger, JH (2002), *Computational Methods for Fluid Dynamics,* 3rd Edition, Springer, Berlin.

[25] Fluent Inc (2002), *Fluent version. 6.0 Manuals*, Lebanon, NH.

[26] Fluent Inc (2002), *Gambit version.2 Manual*, Lebanon, NH.

[27] Fletcher, CAJ (1991), *Computational Techniques for Fluid Dynamics: Volume II,* Second Edition, Spring-Verlag, New York, USA.

[28] Myers, RH & Montgomery, DC (2002), *Response Surface Methodology - Process and Product Optimization Using Designed Experiments,* 2nd Edition, Wiley, New York, USA.

[29] Stander, N & Craig, KJ, (2002) 'On the robustness of a simple domain reduction scheme for simulation-base optimisation', *Engineering Computations*, vol. 19, no. 4, pp. 431-450.

[30] Stander, N, Eggleston, TA, Craig, KJ & Roux, WJ (2003), *LS-OPT User's Manual Version 2,* Livermore Software Technology Corporation, Livermore, CA, USA.

[31] Snyman, JA (2001), 'The LFOPC leap-frog algorithm for constrained optimization', *Computers and Mathematics with Application,* vol. 40, pp. 1085-1096.

[32] Craig, KJ, de Kock, DJ & Snyman, JA (1999), 'Using CFD and mathematical optimisation to minimize stack pollution', *International Journal for Numerical Methods in Engineering*, vol. 44, pp. 551-566.

[33] Craig, KJ, Venter, P, de Kock, DJ & Snyman, JA (1999), 'Optimization of structured grid spacing parameters for separated flow simulation using mathematical optimization', *Journal of Wind Engineering and Industrial Aerodynamics*, vol. 80, pp. 221-231.

[34] De Kock, DJ, Craig, KJ & Snyman, JA (2000), 'Using mathematical optimization in the CFD analysis of a continuous quenching process', *International Journal for Numerical Methods in Engineering*, vol. 47, pp. 985-999.

[35] Craig, KJ, De Kock, DJ & Snyman, JA (2001), 'Minimizing the effect of automotive pollution in urban geometry using mathematical optimization', *Atmospheric Environment*, vol. 35, pp. 579-587.

[36] Craig, KJ, de Kock, DJ, Makgata, KW & de Wet, GJ (2001), 'Design Optimization of a Single-Strand Continuous Caster Tundish Using RTD Data', ISIJ International, vol. 41, no. 10, pp. 1194-1200.

[37] Kingsley, TC (2001), *Effectiveness of Computational Flow Optimisation in a Dynamic Flow Process,* BEng Undergraduate thesis. Department of Mechanical Engineering. University of Pretoria. South Africa.

[38] Craig, KJ & de Kock, D (1998), *Computational Investigation into Flow Phenomena in Touring Car Engine Trumpet and Intake: Modelling of Base Geometry,* Report prepared for Toyota SA Marketing, Laboratory for Advanced Engineering (Pty) Ltd, University of Pretoria, South Africa.

[39] Craig, KJ & de Kock, D (1998), *Computational Investigation into Flow Phenomena in Touring Car Engine Trumpet and Intake: Modifications-Phase 1,* Report prepared for Toyota SA Marketing. Laboratory for Advanced Engineering (Pty) Ltd, University of Pretoria, South Africa.

[40] Renishaw (2001), Retrieved: January 23 2001, from http://www.renishaw.com/client/product/UKEnglish/PRD-1229.shtml.

[41] Paraform Inc. (2002), *Paraform 2.1*.

[42] SuperFlow (2003), *SuperFlow SF-100 flowbench Manual*.

[43] Makgata, KW, Craig, KJ & De Kock, DJ, (2004), 'Computational analysis and parametric study of a high-performance rally engine', *SACAM Paper 42, 4th South African Conference on Applied Mechanics,* Johannesburg region, South Africa.

Appendix A: Intake system

The individual intake system components of the engine concerned are shown in Figure A-1 to Figure A-5.

Figure A-1: Side view of airbox (firewall side)

Figure A-2: Side view of airbox (engine side)

Figure A-3: Air-filter housing

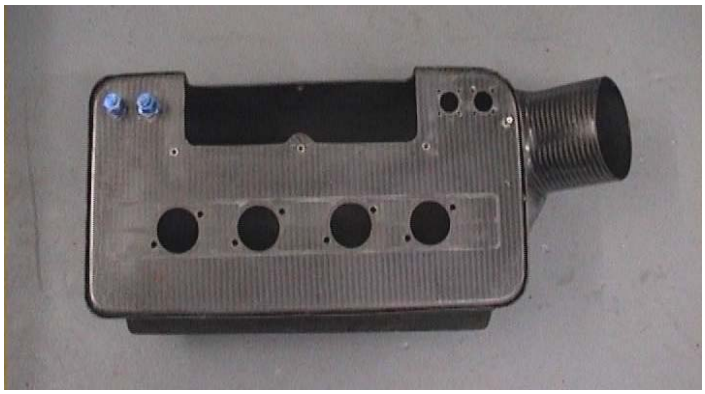

Figure A-4: Bottom view of airbox

Figure A-5: Complete intake system

Appendix B: Input for EngMod4T, Gambit and Fluent

Table B-1: Detail engine input data for EngMod4T

Crank shaft bearing type		Plain
Bore		86.00 mm
Stroke		86.00 mm
Conrod length		148.00 mm
Compression ratio		13.5:1
Exhaust temperature		800 °C
Firing order		1-3-4-2
Exhaust valve		
	Valve open BBDC	75°
	Valve close ATDC	45°
	Valve 1mm open BBDC	56°
	Valve 1mm before closed ATDC	26°
	Dwell angle	5.5°
	Seat outer diameter (dos)	29.45 mm
	Seat inner diameter (dis)	27.40 mm
	Port diameter at valve (dip)	25.70 mm
	Port diameter and manifold	36.80 mm
	Valve stem diameter (dst)	6.00 mm
	Valve seat angle (phi)	45°
	Length of exhaust in head	82.00 mm
	Valve tappet clearance	0.25 mm
Inlet valve		
	Valve open BTDC	53°
	Valve close ABDC	72°
	Valve 1mm open BTDC	31°
	Valve 1mm before closed ABDC	50°
	Dwell angle	4.5°
	Seat outer diameter (dos)	33.89 mm

	Seat inner diameter (dis)	31.62 mm
	Port diameter at valve (dip)	30.07 mm
	Port diameter and manifold	43.10 mm
	Valve stem diameter (dst)	6.00 mm
	Valve seat angle (phi)	45°
	Length of exhaust in head	100 mm
	Valve tappet clearance	0.23 mm
Exhaust system		4 into 2 into 1
Exhaust geometry		See
Air fuel ratio (A/F)		12.7
RPM for maximum power		8000
Type of fuel		Premium

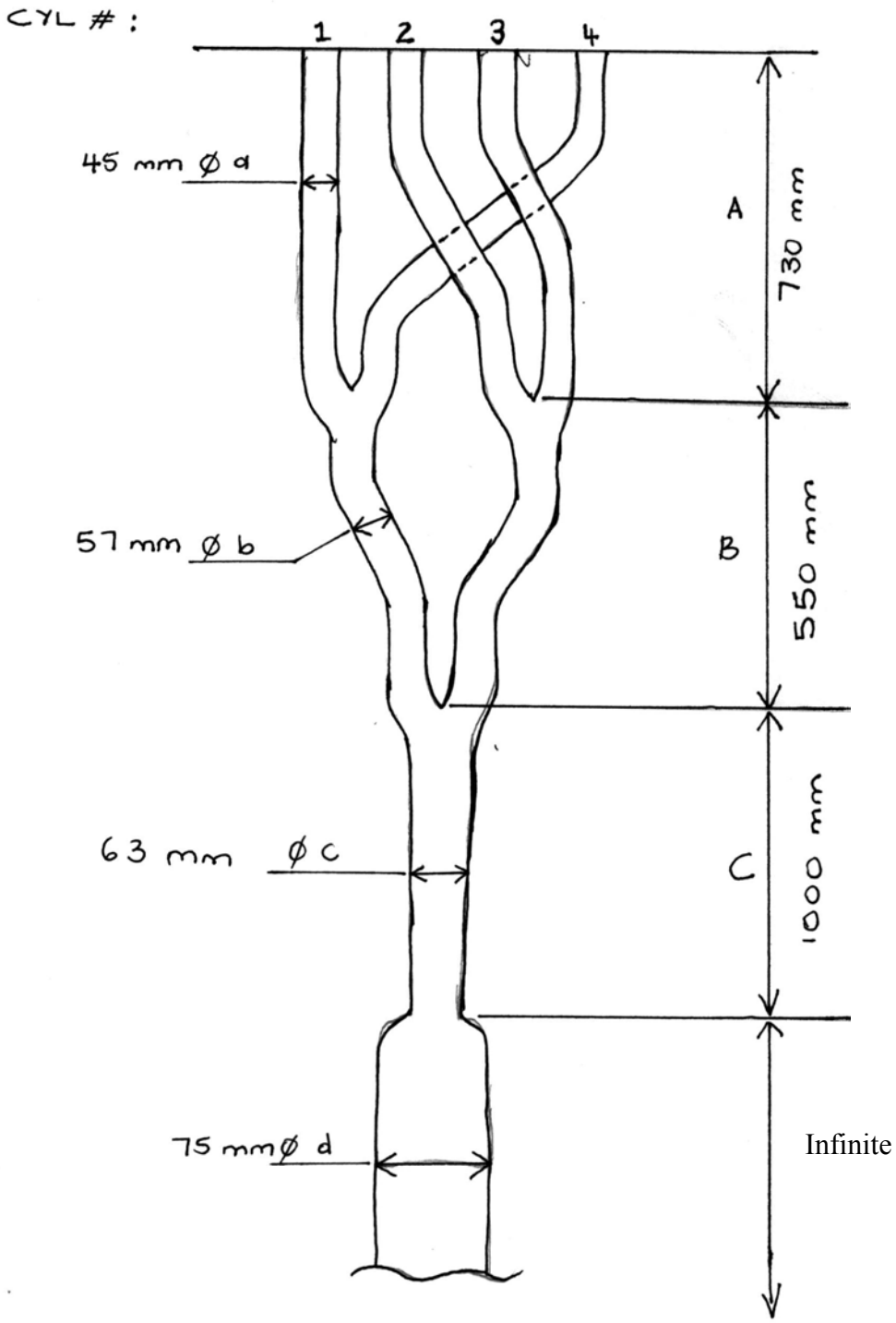

Figure B-1: Exhaust system configuration

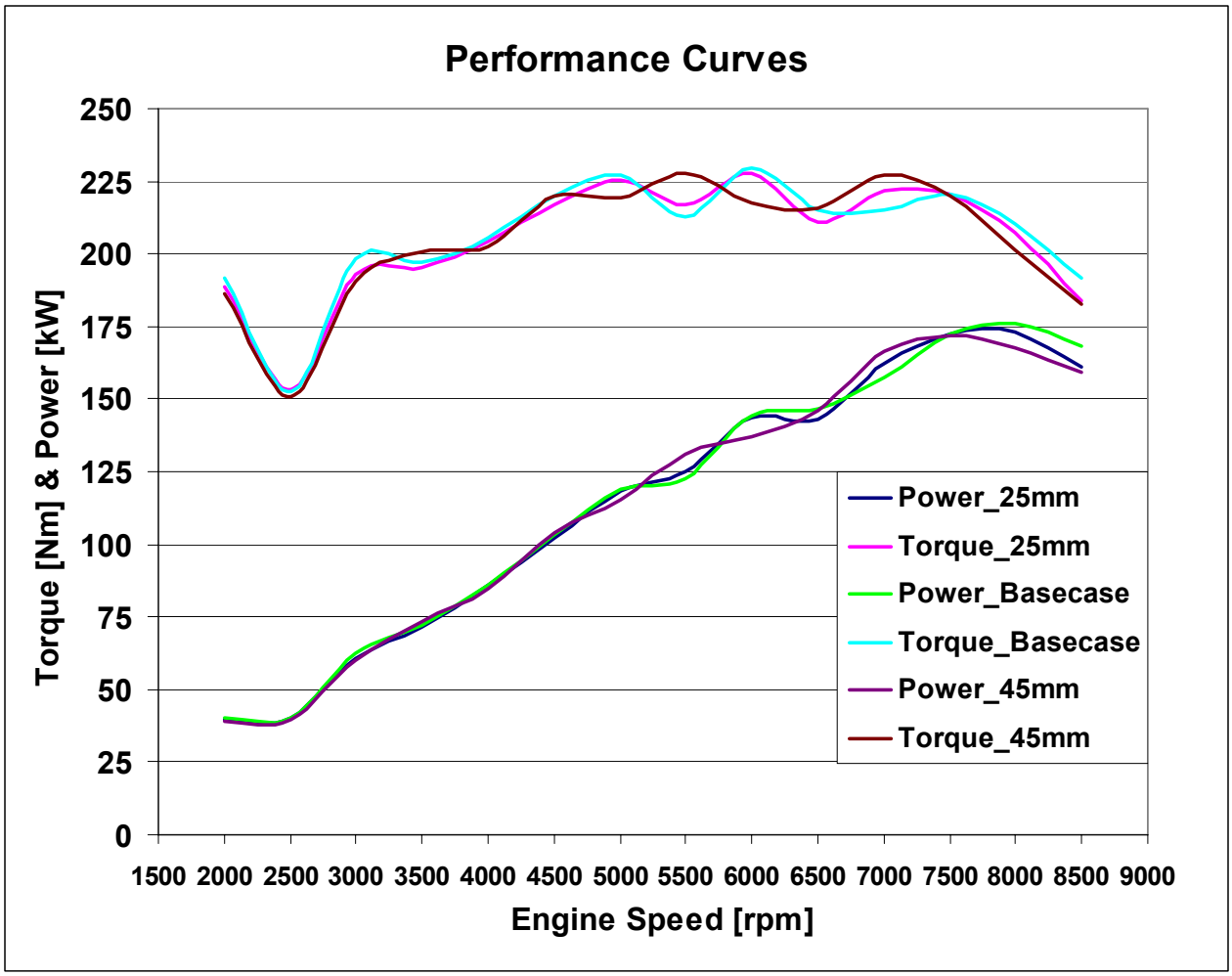

Figure B-2: EngMod4T Engine performance results for different trumpet heights

Appendix C: Experimental Setup

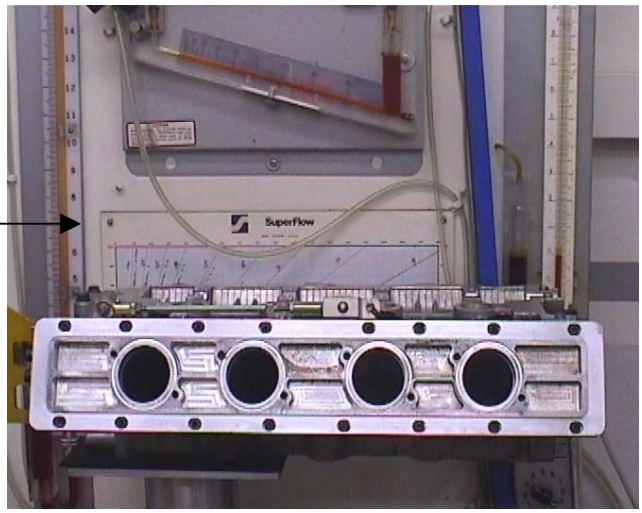

Figure C-1: Cylinder head on the flowbench

Figure C-2: Base of airbox with trumpets bolted on the cylinder head

Figure C-2 shows the trumpets before the top of the airbox is mounted. Note that all but one of the trumpets is blanked off to enable measurement of the flow through only one trumpet.

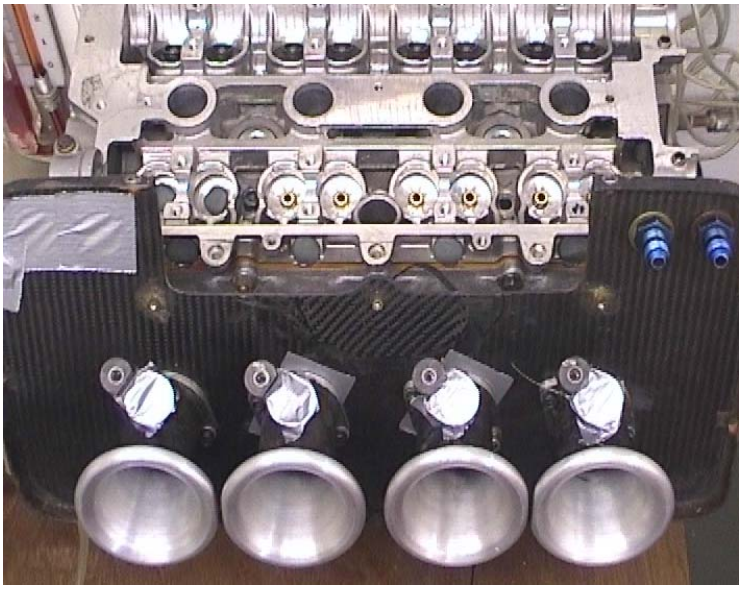

Figure C-3: Another view of trumpet and airbox base assembly

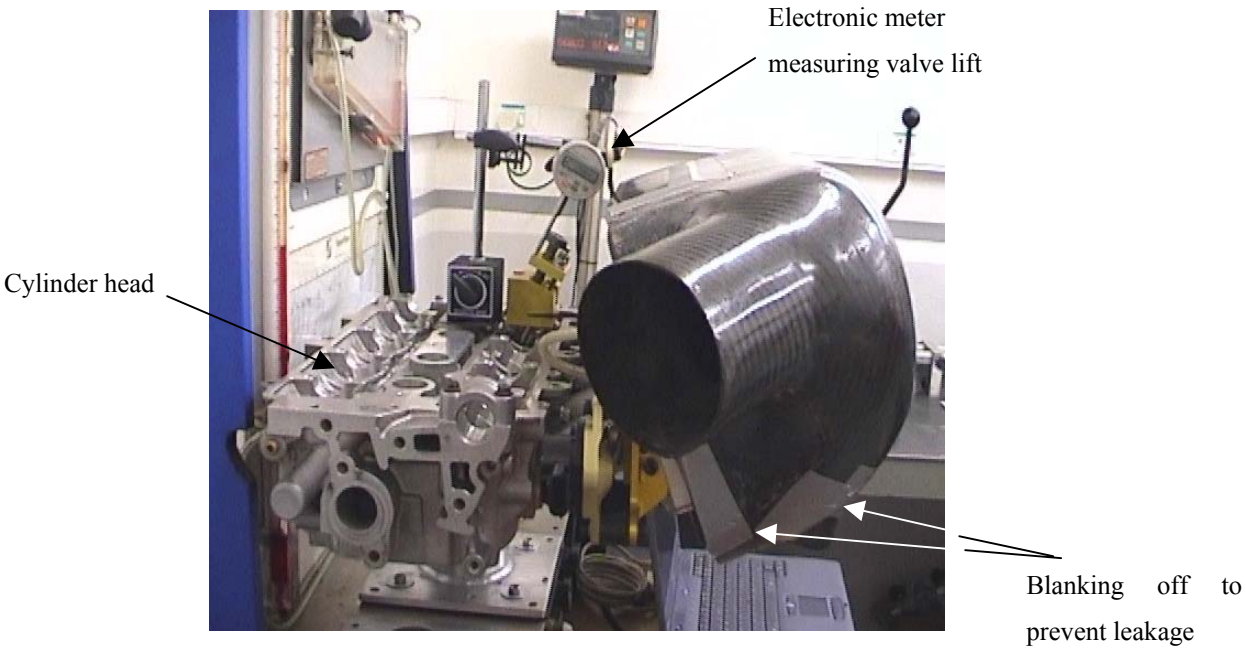

Figure C-4: Cylinder head and airbox test set-up

Note the asymmetrical arrangement of the trumpets and also tap points where airflow measurements are taken.

Appendix D: Journal Files

D-1. Journal file used in the GAMBIT for building models

```
identifier name "t" new nosaveprevious
identifier name "location\inlets_v.dbs" old nosaveprevious *import file with inlet port surfaces
window modify noshade
/max angle = 13 deg

/defining variables
$clear = 66.4
$tclear =(90-$clear)+1
$rad = 50
$offset = 0
$height = 155
$ang = atan((210-$height)/470)
$wid = 78.6

coordinate activate "c_sys.1"
volume create width 470 depth 210 height (240+$wid) offset 235 105 (120+($wid/2)) brick
face create width (240+$wid) height 300 offset 150 0 (120+($wid/2)) zxplane rectangle
face move "face.630" offset 0 40 0
face move "face.630" dangle 60 vector 0 0 260 origin 0 40 0
volume split "volume.96" faces "face.630" connected
volume delete "volume.97" lowertopology
face create width 480 height 210 offset 240 105 0 xyplane rectangle
face move "face.634" offset 0 40 0
face move "face.634" dangle 25 vector 480 0 0 origin 0 40 0
volume split "volume.96" faces "face.634" connected
volume delete "volume.96" lowertopology
vertex cmove "vertex.1414" multiple 1 offset 0 0 100
vertex cmove "vertex.1429" multiple 1 offset 0 0 -100
vertex cmove "vertex.1430" "vertex.1431" multiple 1 offset -500 0 0
edge create straight "vertex.1431" "vertex.1430" "vertex.1432" "vertex.1433"
edge create straight "vertex.1433" "vertex.1431"
face create wireframe "edge.2045" "edge.2046" "edge.2047" "edge.2044" real

/rotating face at angle corresponding to height ratio "$ang"
face move "face.640" dangle $ang vector 0 0 360.727698 origin 470 210 -20.727698
volume split "volume.97" faces "face.640" connected
volume delete "volume.97" lowertopology
edge round "edge.2029" "edge.2048" "edge.2038" "edge.2011" "edge.2049" "edge.2050" \
  "edge.2052" "edge.2032" "edge.2031" "edge.2017" "edge.2040" "edge.2037" "edge.2020" \
  radius1 25
volume blend "volume.98"

vertex cmove "vertex.1454" multiple 1 offset 0 0 100
vertex cmove "vertex.1444" multiple 1 offset 0 0 -100
vertex cmove "vertex.1466" "vertex.1467" multiple 1 offset -500 0 0
edge create straight "vertex.1467" "vertex.1466" "vertex.1468" "vertex.1469"
edge create straight "vertex.1469" "vertex.1467"

/creating face for trumpet clearance "$tclear"
face create wireframe "edge.2109" "edge.2110" "edge.2111" "edge.2112" real
face move "face.671" offset 0 $tclear 0
volume split "volume.98" faces "face.671" connected
volume delete "volume.99" lowertopology
```

```
/creating frustrum inlet "$rad"
volume create height 193 radius1 $rad radius3 55 offset 250 0 0 xaxis frustum
vertex create onedge "edge.2129" uparameter 0.75
vertex create onedge "edge.2129" uparameter 0.25
edge create straight "vertex.1480" "vertex.1481"
volume move "volume.99" offset 229.30706 27.63082 185
edge move "edge.2131" offset 229.30706 27.63802 185

/rotating the inlet "fixed angle"
volume move "volume.99" dangle -40 vector 0 0 100 origin 575.80706 27.63802 135

/offsetting the inlet from original "0" position "$offset"
volume move "volume.99" offset 0 0 -$offset connected

volume unite volumes "volume.99" "volume.98"
import acis "D:\Katlego\Master\CFD\Iter2\trump.sat" ascii
/volume delete "volume.105" "volume.102" "volume.101" "volume.106" \
/  "volume.110" "volume.109" "volume.113" "volume.114" lowertopology
volume unite volumes "volume.110" "volume.111"
volume unite volumes "volume.108" "volume.109"

/splitting the trumpets
volume split "volume.99" volumes "volume.108" connected bientity
volume split "volume.99" volumes "volume.110" connected bientity

/deleting the trumpets "solid"
volume delete "volume.108" "volume.117" lowertopology
volume delete "volume.110" "volume.121" "volume.118" "volume.120" \
  lowertopology

volume split "volume.99" volumes "volume.112" connected bientity
volume split "volume.99" volumes "volume.113" connected bientity
volume split "volume.99" volumes "volume.114" connected bientity
volume split "volume.99" volumes "volume.115" connected bientity

volume split "volume.112" volumes "volume.104" connected bientity
volume split "volume.113" volumes "volume.105" connected bientity
volume split "volume.114" volumes "volume.106" connected bientity
volume split "volume.115" volumes "volume.107" connected bientity

window modify noshade

volume delete "volume.100" "v_volume.94" lowertopology
volume delete "volume.101" "v_volume.92" "volume.102" "v_volume.90" \
  "volume.103" "v_volume.88" lowertopology

volume delete "volume.121" "volume.123" "volume.125" "volume.127" lowertopology


window modify face "face.137" "face.186" "face.232" "face.944" invisible
```

D–2. Journal file used in the FLUENT simulations

```
fi/r-bc/*
fi/rea-prof/*

so/init/init-flow
so/iter 1000
file/write-case-data/D:\Katlego\Master\CFD\last-pt\lp_ss_1st_order.gz

so/set/dis pr 12
so/set/dis mo 1
so/set/dis ep 1
so/set/dis k 1
so/set/dis te 1
so/set/dis temp 1
def/mate/ch-cr/air air y ideal-gas



{DEFAULT VALUES USED}



so/iter 1000
file/write-case-data/*

def/mo/uns-1-o y

so/set/dis fl 22
so/set/dis pr 10
so/set/dis de 0
so/set/dis mo 0
so/set/dis ep 0
so/set/dis k 0
so/set/dis te 0

so/set/und-rel pr 1
so/set/und-rel mo 1
so/set/und-rel ep 1
so/set/und-rel de 1
so/set/und-rel k 1
so/set/und-rel te 1

so/mon/sur/c-m
so/mon/sur/set/p-1 pr p-1 () y 1 n y m-1-exp1_iter_2.out y "Mass Flow Rate"
so/mon/sur/set/p-2 pr p-2 () y 2 n y m-2-exp1_iter_2.out y "Mass Flow Rate"
so/mon/sur/set/p-3 pr p-3 () y 3 n y m-3-exp1_iter_2.out y "Mass Flow Rate"
so/mon/sur/set/p-4 pr p-4 () y 4 n y m-4-exp1_iter_2.out y "Mass Flow Rate"

so/mon/sur/set/m-1 pr p-1 () y 5 n y pr-1-exp1_iter_2.out y "Area-Weighted Average"
so/mon/sur/set/m-2 pr p-2 () y 6 n y pr-2-exp1_iter_2.out y "Area-Weighted Average"
so/mon/sur/set/m-3 pr p-3 () y 7 n y pr-3-exp1_iter_2.out y "Area-Weighted Average"
so/mon/sur/set/m-4 pr p-4 () y 8 n y pr-4-exp1_iter_2.out y "Area-Weighted Average"

(cx-gui-do cx-activate-item "MenuBar*MonitorsSubMenu*Surface...")
(cx-gui-do cx-activate-item "Surface Monitors*Frame2*Table2*PushButton11(Define)")
```

```
(cx-gui-do cx-set-list-selections "Define Surface Monitor*Frame1*Frame1*DropDownList3(X Axis)"
'( 2))
(cx-gui-do cx-activate-item "Define Surface Monitor*Frame1*Frame1*DropDownList3(X Axis)")
(cx-gui-do cx-activate-item "Define Surface Monitor*PanelButtons*PushButton1(OK)")
(cx-gui-do cx-activate-item "Surface Monitors*Frame2*Table2*PushButton17(Define)")
(cx-gui-do cx-set-list-selections "Define Surface Monitor*Frame1*Frame1*DropDownList3(X Axis)"
'( 2))
(cx-gui-do cx-activate-item "Define Surface Monitor*Frame1*Frame1*DropDownList3(X Axis)")
(cx-gui-do cx-activate-item "Define Surface Monitor*PanelButtons*PushButton1(OK)")
(cx-gui-do cx-activate-item "Surface Monitors*Frame2*Table2*PushButton23(Define)")
(cx-gui-do cx-set-list-selections "Define Surface Monitor*Frame1*Frame1*DropDownList3(X Axis)"
'( 2))
(cx-gui-do cx-activate-item "Define Surface Monitor*Frame1*Frame1*DropDownList3(X Axis)")
(cx-gui-do cx-activate-item "Define Surface Monitor*PanelButtons*PushButton1(OK)")
(cx-gui-do cx-activate-item "Surface Monitors*Frame2*Table2*PushButton29(Define)")
(cx-gui-do cx-set-list-selections "Define Surface Monitor*Frame1*Frame1*DropDownList3(X Axis)"
'( 2))
(cx-gui-do cx-activate-item "Define Surface Monitor*Frame1*Frame1*DropDownList3(X Axis)")
(cx-gui-do cx-activate-item "Define Surface Monitor*PanelButtons*PushButton1(OK)")
(cx-gui-do cx-activate-item "Surface Monitors*Frame2*Table2*PushButton35(Define)")
(cx-gui-do cx-set-list-selections "Define Surface Monitor*Frame1*Frame1*DropDownList3(X Axis)"
'( 2))
(cx-gui-do cx-activate-item "Define Surface Monitor*Frame1*Frame1*DropDownList3(X Axis)")
(cx-gui-do cx-activate-item "Define Surface Monitor*PanelButtons*PushButton1(OK)")
(cx-gui-do cx-activate-item "Surface Monitors*Frame2*Table2*PushButton41(Define)")
(cx-gui-do cx-set-list-selections "Define Surface Monitor*Frame1*Frame1*DropDownList3(X Axis)"
'( 2))
(cx-gui-do cx-activate-item "Define Surface Monitor*Frame1*Frame1*DropDownList3(X Axis)")
(cx-gui-do cx-activate-item "Define Surface Monitor*PanelButtons*PushButton1(OK)")
(cx-gui-do cx-activate-item "Surface Monitors*Frame2*Table2*PushButton47(Define)")
(cx-gui-do cx-set-list-selections "Define Surface Monitor*Frame1*Frame1*DropDownList3(X Axis)"
'( 2))
(cx-gui-do cx-activate-item "Define Surface Monitor*Frame1*Frame1*DropDownList3(X Axis)")
(cx-gui-do cx-activate-item "Define Surface Monitor*PanelButtons*PushButton1(OK)")
(cx-gui-do cx-activate-item "Surface Monitors*Frame2*Table2*PushButton53(Define)")
(cx-gui-do cx-set-list-selections "Define Surface Monitor*Frame1*Frame1*DropDownList3(X Axis)"
'( 2))
(cx-gui-do cx-activate-item "Define Surface Monitor*Frame1*Frame1*DropDownList3(X Axis)")
(cx-gui-do cx-activate-item "Define Surface Monitor*PanelButtons*PushButton1(OK)")
(cx-gui-do cx-activate-item "Surface Monitors*PanelButtons*PushButton1(OK)")

(rpsetvar 'flow-time 0.000013293)
def/bc/zt p-1 po
def/bc/po p-1 y "cyl_prof_1" "p" n y "cyl_prof_1" "temp" n y n n n y 5 50
def/bc/zt p-3 wall
def/bc/zt p-4 wall
def/bc/zt p-2 po
def/bc/po p-2 y "cyl_prof_2" "p" n y "cyl_prof_2" "temp" n y n n n y 5 50
sol/set/ts 0.00004
sol/dti 64 20
def/bc/zt p-2 wall
sol/set/ts 0.00004
sol/dti 51 20
def/bc/zt p-3 po
def/bc/po p-3 y "cyl_prof_3" "p" n y "cyl_prof_3" "temp" n y n n n y 5 50
sol/set/ts 0.00004
sol/dti 64 20
def/bc/zt p-1 wall
sol/set/ts 0.00004
sol/dti 51 20
```

```
def/bc/zt p-4 po
def/bc/po p-4 y "cyl_prof_4" "p" n y "cyl_prof_4" "temp" n y n n n y 5 50
sol/set/ts 0.00004
sol/dti 64 20
def/bc/zt p-3 wall
sol/set/ts 0.00004
sol/dti 51 20
def/bc/zt p-2 po
def/bc/po p-2 y "cyl_prof_2" "p" n y "cyl_prof_2" "temp" n y n n n y 5 50
sol/set/ts 0.00004
sol/dti 64 20
def/bc/zt p-4 wall
sol/set/ts 0.00004
sol/dti 51 20
file/write-case-data/*
```

*file location

Appendix E: Summary of Results

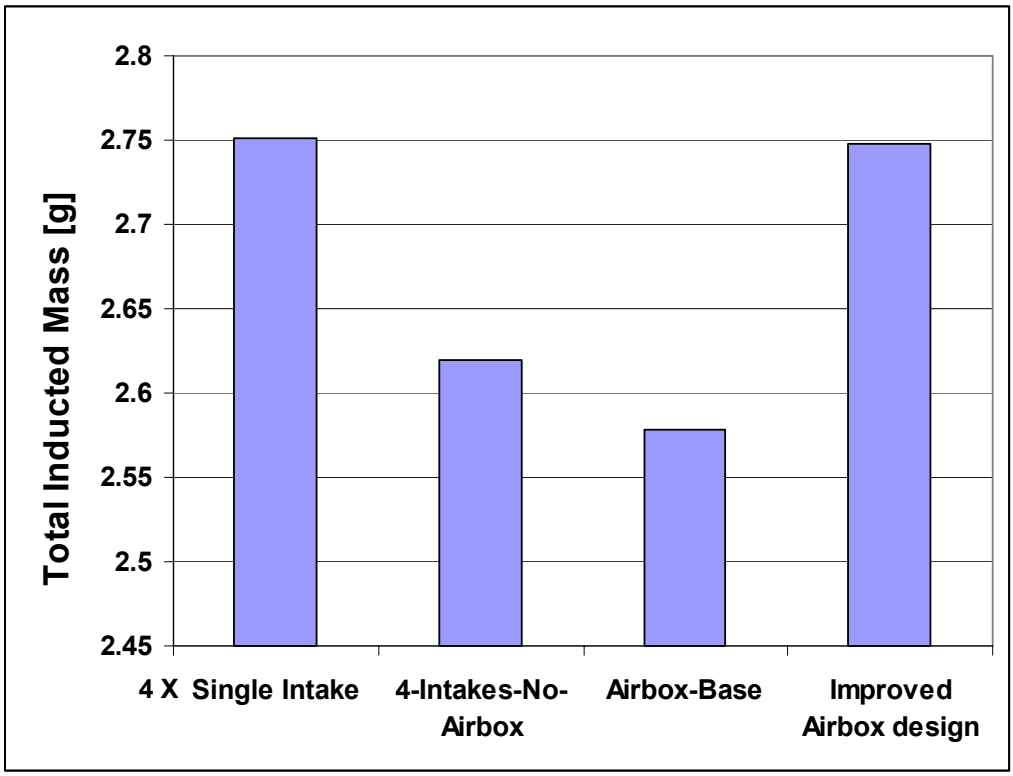

Figure E-1: Total mass inducted for considered cases over one engine cycle

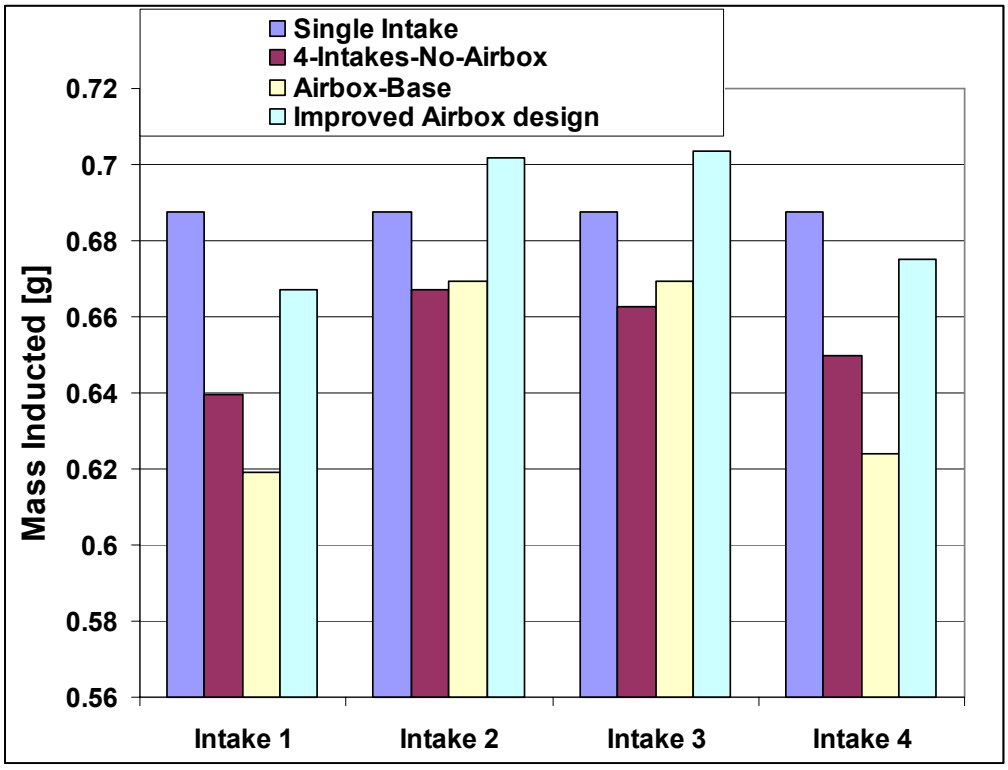

Figure E-2: Plot of individual intake flow induction for the four considered cases